Diploma Thesis:

Heat Conductivity Measurements in Artificial Lunar Soil Samples

Wärmeleitmessungen in künstlichen Mondbodenproben

Thomas Ballatré
Matriculation No. 2641917
15.10.2013

Supervisors:
Priv.-Doz. Dr.-Ing. Ralf Srama
University of Stuttgart
Faculty 6: Aerospace Engineering and Geodesy
Institute of Space Systems

Dipl.-Ing. Volker Maiwald
German Aerospace Center (DLR)
Institute of Space Systems
System Analysis Space Segment

UNIVERSITÄT STUTTGART
INSTITUT FÜR RAUMFAHRTSYSTEME
im Raumfahrtzentrum Baden-Württemberg (RZBW)

Pfaffenwaldring 29 · 70569 Stuttgart · Tel.: (0711) 685-62375 · Fax: (0711) 685-63596 · www.irs.uni-stuttgart.de

Aufgabenstellung Diplomarbeit für Herrn Thomas Ballatré

Thema englisch: Heat Conductivity Measurements in Artificial Lunar Soil Samples

Thema deutsch: Wärmeleitmessungen in künstlichen Mondbodenproben

Motivation:

Temperature measurements of Apollo 15 and Apollo 17 experiments revealed a significant heat reserve in subsurface regions of the Moon. Depths of 0.5 m show temperatures of about 250 K. In the frame of the project "Selenothermal Power Generation" it is investigated how this heat can be used to supply space systems (e.g. rovers, static experiments, infrastructure) with electrical power during the 14 days long lunar night.
The efficiency of any energy transformation process (heat to electrical energy) is strongly depending on the heat transfer to a given power generation system. It is influenced by the system itself, the fluid used for the power generation process and the lunar regolith.
The goal of the present thesis is to support the design of a power generation system with measurement data about the heat transfer from the lunar regolith to the power generation system itself.

Objectives:

- Review and selection of artificial lunar soil samples that thermally have the most similar behavior compared to actual lunar regolith
- Design of a testbed for heat transfer measurements from regolith to a pipe system containing flowing liquid nitrogen
- Construction of the testbed and measurement of the heat transfer.
- The testbed should be easily adaptable for usage of different materials, exchange of soil samples and adaption of the heat exchanger model.

Betreuer intern: PD Dr.-Ing. Ralf Srama

Bearbeitungsbeginn: 01.05.2013

Einzureichen spätestens: 01.11.2013

_____ PD Dr.-Ing. R. Srama
(Verantwortlicher Hochschullehrer)

_____ Unterschrift des/der Studierenden

Affirmation

Hereby I affirm that I wrote this thesis without any inadmissible help by a third party and without using any other means than indicated. Thoughts that were taken directly or indirectly from other sources are indicated as such. This thesis has not been presented to any other examination board in this or a similar form, neither in Germany nor in any other country.

Bremen, 15^{th} of October 2013

Acknowledgement

Foremost, I would like to express my deepest gratitude to my supervisor at the German Aerospace Center (DLR), Volker Maiwald, who has always been a great help during my thesis. Special thanks also go to Priv.-Doz. Dr.-Ing. Ralf Srama for supervising my thesis at the University of Stuttgart. I would like to show my greatest appreciation to Conrad Zeidler (DLR), Rob Mueller (NASA), Eugen Ksenik (DLR), Siebo Reershemius (DLR), Alexander Fischer (DLR), Patrick Winkler (DLR), and Nicolas Darkow (DLR) for providing me with support for the hardware. I am grateful for the assistance given by the SARA, SART, and TAS departments at DLR, especially by Mona Carlsen and Vincent Vrakking for help with CATIA and Vanessa Clark for proofreading this thesis.

Abstract

One of the key challenges presented by the establishment of a lunar surface base is the energy supply. The lunar night, lasting 14 Earth-days, makes purely solar-based energy generation unfeasible. Manned bases require continuous electricity supply as they cannot be simply shut-down like robots or rovers.

The unique problem of continuously powering the environmental control and life support system (ECLSS) is under investigation at the German Aerospace Center (DLR). One proposed solution is the Selenothermal Power Generation (SPG) concept. This solution is predicted to generate sufficient energy to supplement solar generators during the lunar nocturnal period.

This thesis investigates ground-based experimental validation of the SPG concept, including the design and construction of a test rig to perform heat conductivity measurements, as well as the execution of experiments to determine the heat transfer coefficient, which is needed to support the design of a power generation system.

Zusammenfassung

Eine der größten Herausforderungen bei der Errichtung einer Mondbasis stellt die benötigte Energieversorgung dar. Die lunare Nacht, welche 14 Erdtage andauert, macht es unmöglich, ausschließlich Solarenergie zu nutzen. Da bemannte Stationen nicht einfach wie Roboter oder Rover abgeschaltet werden können, benötigen sie eine dauerhafte Stromversorgung.

Eine Lösung des Problems der dauerhaften Energieversorgung für Lebenserhaltungssysteme wird am Deutschen Zentrum für Luft- und Raumfahrt (DLR) untersucht. Das Konzept "Selenothermal Power Generation" (SPG) ist eine mögliche Lösung dieses Problems. Dieses Konzept soll genügend Energie erzeugen, um die Solargeneratoren während der lunaren Nacht zu ersetzen.

Das Ziel dieser Diplomarbeit ist die experimentelle Validierung des SPG-Konzepts. Dazu zählt sowohl die Entwicklung und der Bau eines Teststandes zur Durchführung von Wärmeleitmessungen als auch die dadurch mögliche Bestimmung des Wärmedurchgangskoeffizienten. Dieser wird benötigt, um die Entwicklung des Energiegewinnungssystems zu unterstützen.

Contents

List of Abbreviations

BP-1	Black Point 1
DLR	German Aerospace Center (Deutsches Zentrum für Luft- und Raumfahrt)
ECLSS	Environmental Control and Life Support System
EVA	Extra-Vehicular Activities
FHT	Feldspathic Highlands Terrane
FJS-1	Fuji Japanese Simulant 1
FJS-2	Fuji Japanese Simulant 2
FJS-3	Fuji Japanese Simulant 3
FoM	Figures of Merit
ISRU	In-Situ Resource Utilisation
JAXA	Japan Aerospace Exploration Agency
JSC-1	Johnson Space Center Number One
KREEP	Chemical Component with Enrichment in Potassium (K), Rare-Earth Elements (REE), Phosphorous (P), Thorium (Th), and Uranium (U)
LOI	Loss On Ignition
LN	Liquid Nitrogen
MLS-1	Minnesota Lunar Simulant 1
Mt.	Mount
NASA	National Aeronautics and Space Administration
PKT	Procellarum KREEP Terrane
PTFE	Polytetrafluoroethylene
SPG	Selenothermal Power Generation
STP	Standard Temperature and Pressure
USA	United States of America
wt. %	Weight Per Cent

List of Chemical Symbols

Al_2O_3	Aluminium oxide
CaO	Calcium oxide
CO_2	Carbon dioxide
Cr_2O_3	Chromium(III) oxide
Fe_2O_3	Ferric oxide
FeO	Ferrous oxide
H_2O	Water
K_2O	Potassium oxide
MgO	Magnesium oxide
MnO	Manganese(II) oxide
N_2	Nitrogen
Na_2O	Sodium oxide
P_2O_5	Phosphorus pentoxide
SiO_2	Silicon dioxide
SO_2	Sulfur dioxide
TiO_2	Titanium dioxide

Nomenclature

Latin Alphabet

$\mathbf{A}$	m^2	Area
$\mathbf{A_{GLS}}$	m^2	Area of gas in a liquid slug
$\mathbf{A_{GTB}}$	m^2	Area of gas in a Taylor bubble
$\mathbf{A_{HE}}$	m^2	Inner area of the heat exchanger pipe
$\mathbf{a}$	-	Coefficient, defined in Chapter 2 on page 15
$\mathbf{b}$	-	Coefficient, defined in Chapter 2 on page 15
$\mathbf{b_i}$	-	Coefficients, defined in Chapters 2 and 4 on pages 19 and 34
$\mathbf{C}$	$\frac{J}{kg \cdot K}$	Heat capacity
$\mathbf{C_m}$	$\frac{J}{mol \cdot K}$	Molar heat capacity
$\mathbf{C_v}$	$\frac{J}{m^3 \cdot K}$	Volumetric heat capacity
$\mathbf{c}$	-	Coefficient, defined in Chapter 2 on page 15
$\mathbf{c_p}$	$\frac{J}{kg \cdot K}$	Isobaric heat capacity
$\mathbf{c_v}$	$\frac{J}{kg \cdot K}$	Isochoric heat capacity
$\mathbf{d}$	m	Diameter
$\mathbf{d_i}$	-	Coefficients, defined in Chapters 2 and 4 on pages 19 and 34
$\mathbf{e}$	$\frac{W}{m^2 \cdot K}$	Average deviation of k
$\mathbf{F}$	N	Force
$\mathbf{f}$	-	Pipe friction factor
$\mathbf{h_{tp}}$	-	Two-phase pipe friction factor
$\mathbf{g}$	$\frac{m}{s^2}$	Gravitational acceleration
$\mathbf{H}$	m	Height
$\mathbf{h}$	$\frac{J}{kg}$	Specific enthalpy

$\mathbf{h_v}$	$\frac{\mathrm{J}}{\mathrm{kg}}$	Enthalpy in vaporization
$\mathbf{I}$	A	Current
$\mathbf{k}$	$\frac{\mathrm{W}}{\mathrm{m^2 \cdot K}}$	Heat transfer coefficient
$\mathbf{k_B}$	$\frac{\mathrm{J}}{\mathrm{K}}$	Boltzmann's constant
$\mathbf{l}$	m	Specific length
$\mathbf{l_i}$	-	Coefficients, defined in Chapters 2 and 4 on pages 19 and 34
$\mathbf{l_{TB}}$	m	Length of a Taylor bubble
$\mathbf{M}$	$\frac{\mathrm{g}}{\mathrm{mol}}$	Molar mass
$\mathbf{m}$	kg	Mass
$\dot{\mathbf{m}}$	$\frac{\mathrm{kg}}{\mathrm{s}}$	Mass flow rate
$\mathbf{N_i}$	-	Coefficients, defined in Chapters 2 and 4 on pages 19 and 34
$\mathbf{P}$	W	Power
$\mathbf{p_c}$	Pa	Critical pressure
$\dot{\mathbf{Q}}$	W	Heat flow
$\mathbf{q_D}$	nm	Constant, defined in Chapter 2 on page 20
$\mathbf{R}$	Ω	Resistance
$\mathbf{R_0}$	-	Constant, defined in Chapter 2 on page 20
$\tilde{\mathbf{R}}_\mathbf{0}$	-	Constant, defined in Chapter 2 on page 15
$\mathbf{R_s}$	mm	Surface roughness coefficient
$\mathbf{Re}$	-	Reynolds number
$\mathbf{Re_c}$	-	Critical Reynolds number
$\mathbf{S}$	$\frac{\mathrm{W}}{\mathrm{m^2 \cdot K}}$	Standard deviation of k
$\mathbf{T}$	K	Temperature
$\mathbf{T_c}$	K	Critical temperature
$\mathbf{T_{ref}}$	K	Reference temperature
$\bar{\mathbf{T}}_\mathbf{regolith}$	K	Average regolith temperature
$\mathbf{t}$	s	Average time step between the phase change

$\mathbf{t_i}$	-	Coefficients, defined in Chapters 2 and 4 on pages 19 and 34
$\mathbf{U}$	V	Voltage
$\mathbf{u}$	$\frac{\mathrm{J}}{\mathrm{kg}}$	Specific internal energy
$\mathbf{V}$	m^3	Volume
$\dot{\mathbf{V}}$	$\frac{\mathrm{m}^3}{\mathrm{s}}$	Volume flow rate
$\mathbf{V_G}$	m^3	Total volume of gas in one slug unit
$\mathbf{V_{SU}}$	m^3	Total volume of a slug unit
$\mathbf{v}$	$\frac{\mathrm{m}}{\mathrm{s}}$	Velocity
$\mathbf{x}$	-	Vapour quality in the nitrogen flow
$\bar{\mathbf{x}}$	$\frac{\mathrm{W}}{\mathrm{m}^2 \cdot \mathrm{K}}$	Arithmetic average of k
$\mathbf{x_L}$	-	Ratio of the liquid phase in a slug unit
$\mathbf{x_{TB}}$	-	Ratio of the Taylor bubble in a slug unit
$\mathbf{y}$	-	Mass fraction
$\mathbf{z}$	cm	Depth

Greek Alphabet

$\boldsymbol{\alpha_{LS}}$	-	Coefficient, defined in Chapter 7 on page 69
$\boldsymbol{\alpha_s}$	$\frac{\mathrm{V}}{\mathrm{K}}$	Seebeck coefficient
$\boldsymbol{\alpha_{SU}}$	-	Volume average void fraction over one slug unit
$\boldsymbol{\alpha_{TB}}$	-	Coefficient, defined in Chapter 7 on page 69
$\boldsymbol{\beta}$	-	Coefficient, defined in Chapter 7 on page 69
$\boldsymbol{\Gamma}$	-	Constant, defined in Chapter 2 on page 20
$\boldsymbol{\gamma}$	-	Constant, defined in Chapter 2 on page 20
$\boldsymbol{\gamma_i}$	-	Coefficients, defined in Chapter 4 on page 34
$\boldsymbol{\Delta p}$	Pa	Pressure difference
$\boldsymbol{\Delta p_{frict}}$	Pa	Frictional pressure loss
$\boldsymbol{\Delta p_{mom}}$	Pa	Momentum pressure loss
$\boldsymbol{\Delta p_{static}}$	Pa	Static pressure loss

$\mathbf{\Delta p_V}$	Pa	Pressure loss
$\mathbf{\Delta T_b}$	K	Bigger temperature difference in the heat exchanger
$\mathbf{\Delta T_m}$	K	Mean logarithmic temperature difference
$\mathbf{\Delta T_s}$	K	Smaller temperature difference in the heat exchanger
$\boldsymbol{\delta}$	-	Coefficient, defined in Chapter 2 on page 19
$\frac{\boldsymbol{\epsilon}}{\mathbf{k}}$	K	Lennard-Jones energy parameter
$\boldsymbol{\zeta}$	-	Pressure loss coefficient
$\boldsymbol{\eta}$	$\frac{\mathrm{m}^2}{\mathrm{s}}$	Viscosity
$\boldsymbol{\eta^0}$	$\frac{\mathrm{m}^2}{\mathrm{s}}$	Dilute gas viscosity
$\boldsymbol{\eta^r}$	$\frac{\mathrm{m}^2}{\mathrm{s}}$	Residual fluid viscosity
$\boldsymbol{\kappa}$	$\frac{\mathrm{g}}{\mathrm{cm}^3}$	Constant, defined in Chapter 2 on page 7
$\boldsymbol{\lambda}$	$\frac{\mathrm{W}}{\mathrm{m \cdot K}}$	Thermal conductivity
$\boldsymbol{\lambda^0}$	$\frac{\mathrm{W}}{\mathrm{m \cdot K}}$	Dilute gas thermal conductivity
$\boldsymbol{\lambda^c}$	$\frac{\mathrm{W}}{\mathrm{m \cdot K}}$	Thermal conductivity critical enhancement
$\boldsymbol{\lambda^r}$	$\frac{\mathrm{W}}{\mathrm{m \cdot K}}$	Residual fluid thermal conductivity
$\boldsymbol{\nu}$	-	Constant, defined in Chapter 2 on page 20
$\boldsymbol{\xi}$	nm	Correlation length
$\boldsymbol{\xi_0}$	nm	Constant, defined in Chapter 2 on page 20
$\boldsymbol{\pi}$	-	Mathematical constant
$\boldsymbol{\rho}$	$\frac{\mathrm{kg}}{\mathrm{m}^3}$	Density
$\boldsymbol{\rho_0}$	$\frac{\mathrm{g}}{\mathrm{cm}^3}$	Constant, defined in Chapter 2 on page 7
$\boldsymbol{\rho_g}$	$\frac{\mathrm{g}}{\mathrm{cm}^3}$	Density of the gas phase
$\boldsymbol{\rho_c}$	$\frac{\mathrm{g}}{\mathrm{cm}^3}$	Critical density
$\boldsymbol{\rho_L}$	$\frac{\mathrm{g}}{\mathrm{cm}^3}$	Density of the liquid phase
$\boldsymbol{\rho_{SU}}$	$\frac{\mathrm{g}}{\mathrm{cm}^3}$	Average density of a slug unit
$\boldsymbol{\sigma}$	nm	Lennard-Jones size parameter
$\boldsymbol{\tau}$	-	Coefficient, defined in Chapter 2 on page 19

$\mathbf{\Omega}$	-	Collision integral
$\tilde{\mathbf{\Omega}}$	-	Coefficient, defined in Chapter 2 on page 19
$\tilde{\mathbf{\Omega}}_{\mathbf{0}}$	-	Coefficient, defined in Chapter 2 on page 20

1. Introduction

1.1. Motivation

For millennia, humans have been fascinated by the moon. It was a central part of many civilisations; for example, the ancient Egyptians used a lunar calendar to organise their communal lives, and the Moon is portrayed as a God in several ancient cultures. In the decades following the industrial revolution, humans realised they were able to achieve remarkable things through technology, and authors of the time created elaborate stories about incredible ships that allowed humans to fly to the moon. The science fiction became reality; first in 1959 when the Russian Lunik 2 spacecraft was guided to impact on the lunar surface. This was followed by the first humans in 1969. These missions proved that off-planet exploration was possible and greatly influenced a generation to continue space exploration. However, the advances in manned exploration are stagnating along with the spirit of adventure. If mankind is to continue its progress through the solar system, one possible next step is the establishment of a moon-base. This would enable extended lunar stays and provide an outpost from which further missions can be launched.

A permanent lunar outpost has many inherent technical challenges. Large amounts of energy are required to allow the survival of humans. The environmental control and life support system (ECLSS) already requires 3 kW per person per day for an open system, the food production requires 35 kW per person per lunar night (about 14 days on Earth) [3], and scientific or industrial tasks will require even more. A large infrastructure would be needed to obtain this energy from the Sun alone. Huge energy storage systems would be required to power the base through the lunar nights.

One solution to this problem, Selenothermal Power Generation (SPG), is under investigation by the German Aerospace Center (DLR). This generation method uses the inherent, elevated lunar soil (regolith) temperature to power a dynamic conversion cycle. Experiments conducted during the Apollo 15 and 17 missions measured a constant temperature of 250 K at a depth of 0.5 m on the Moon. The SPG concept uses geothermal power generation methods, taking advantage of the nearly-constant temperature of the lunar soil. Primarily, two processes are being investigated; the Rankine and Stirling processes, both using a nitrogen working fluid.

These conversion processes are already well-developed, however experimental data is needed to support the design of a SPG system. Amongst these, heat transfer from the lunar regolith to the power generating system needs to be experimentally investigated. The unique conditions on the Moon which are not comparable to those on Earth must be accounted for in the system design. Two important factors have to be taken into account; the prevailing vacuum on the Moon, as well as the special physical behaviour of the lunar regolith.

1.2. Objectives

The objectives of this thesis are to perform preliminary investigations into the ground-testing of the SPG technology in a simulated lunar environment, and to develop a test rig for such experiments. To achieve these objectives, the following tasks will be undertaken:

- Review and analysis of lunar soil simulants;
- Generation of recommendations for the best artificial lunar soil, based on investigations;
- Design and construction of a test rig for heat transfer measurements from the regolith to flowing nitrogen in a pipe system;
- Experimental measurements of the heat transfer.

1.3. Definitions

1.3.1. Thermal Conductivity

Thermal conductivity (also heat conductivity), λ, is defined as the physical property governing heat diffusion in the steady state. It is the quantity of heat that passes per second through a unit cross section of material with unit thickness, when its opposite faces differ in temperature by one Kelvin. Its dimensions are W/(m·K). [23]

1.3.2. Heat Transfer Coefficient

The heat transfer coefficient, k, is a coefficient describing the heat flow from one material through another, solid material to a fluid, due to a temperature difference between the materials (see also Equation 2). Its dimensions are W/(m^2·K). [5]

2. Fundamentals

The SPG concept has arisen from unique characteristics of the lunar regolith. This chapter will provide an overview of the Moon's characteristics and how they are utilised in this concept.

2.1. Lunar Characteristics

2.1.1. Formation

There are different theories concerning the formation of the Moon. In the mid 19^{th} century, some members of the scientific community still believed that the Moon was created at the same time as the Earth. The hills and valleys were seen as a proof for the former existence of water on the Moon, which later evaporated or left to other celestial bodies. [9] In the 1970s the Giant Impact Hypothesis was verbalised. Cameron and Ward proposed in 1976 that a Mars-sized body collided with the Earth and thereby formed the Moon. [10] Later, in 2000 Cameron revised this theory to an impact of a body twice the size of Mars during Earth's accretion [29]. A more exhaustive study in 2001 by Canup and Ashaug came to the conclusion that an impact of a Mars-sized body near the very end of Earth's accumulation is the most likely theory for the formation of the Moon. Their simulations indicate that most of the material yielding the Moon originates from the impacting object, rather than from Earth. [11]

2.1.2. Build-up

The outermost layer of the Moon is the crust. Beneath the crust is the mantle which surrounds the core of the Moon. Impacts have shattered and fragmented the lunar crust down to a depth of several kilometres, producing a global layer of chaotically mixed impact debris, termed "megaregolith" (Figure 2.1). Early seismic studies predicted crustal thicknesses of about 60 km beneath the Apollo network. More recent studies, however, propose thinner crusts of only 45 km, 38 km or 30 km. On the basis of Lunar Prospector gamma-ray data, the lunar crust and the mantle were divided into distinct terranes that possess unique geophysical and geological characteristics. The biggest terranes are the Procellarum KREEP (Potassium, K; Rare-Earth Elements, REE; Phosphorous, P) Terrane (PKT); and the Feldspathic Highlands Terrane (FHT). The latter covers about 60% of the Moon's surface area. At a depth of about 560 km below the surface there is a seismic discontinuity in the mantle, indicating a possible compositional change. The low mean lunar density of 3344 kg/m^3 indicates that the Moon has only a small iron core compared to that of Earth or any other terrestrial planet. [30] The interior structure of the Moon can be seen in Figure 2.2.

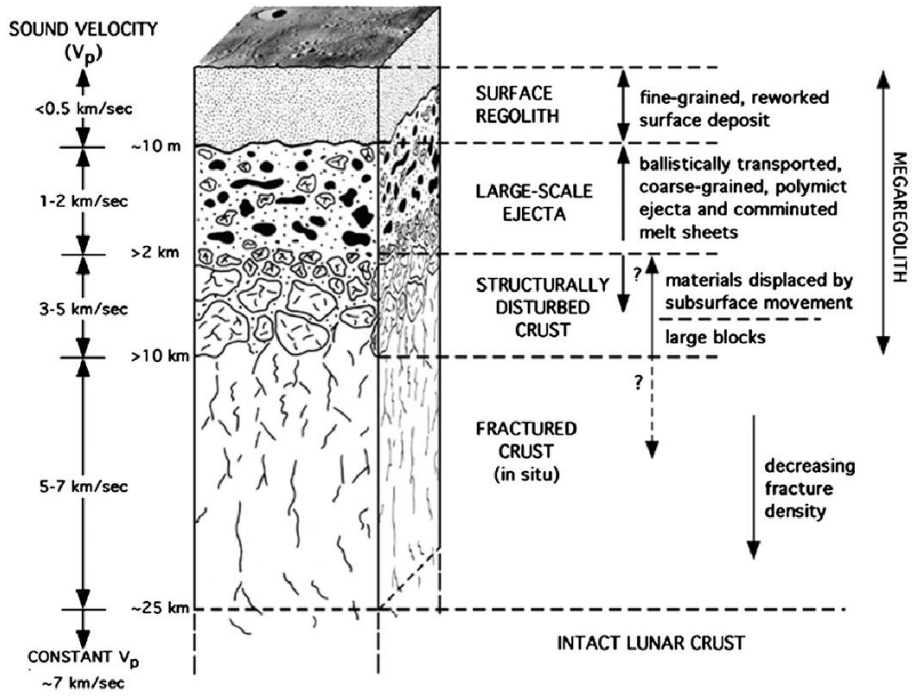

Figure 2.1.: Highly Idealised Cross-Section through the Internal Structure of the Megaregolith [30].

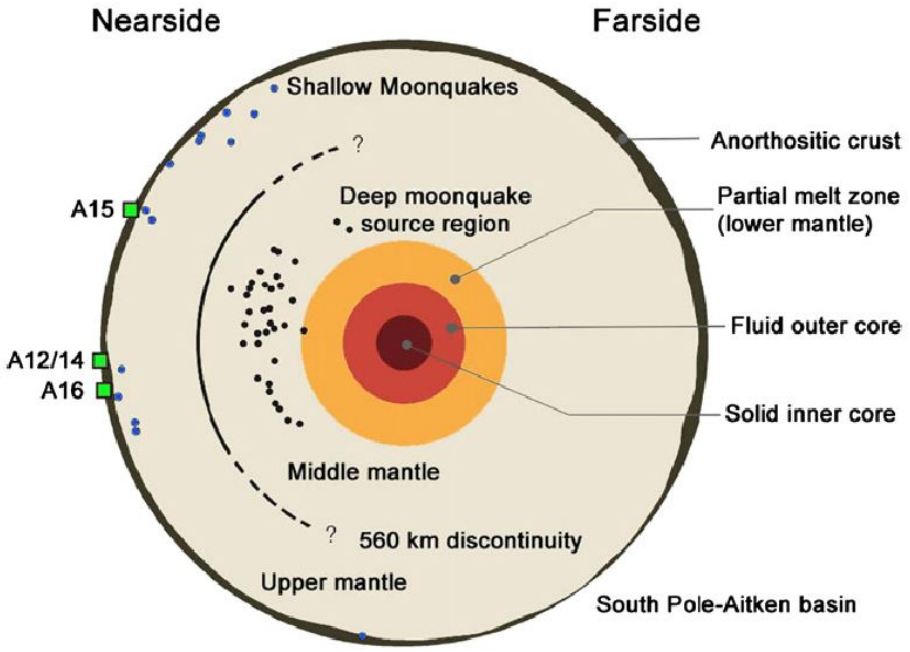

Figure 2.2.: Pole-to-Pole Cross Section of the Interior Structure of the Moon [30].

The conditions on the Moon are vastly different to those on Earth. A comparison of the physical properties of the Moon and Earth is provided in Table 2.1.

2.1.3. Lunar Regolith

2.1.3.1. Overview

Our knowledge of the diversity of lunar rock types is based on the Apollo and Luna mission samples, as well as on remote sensing data. Lunar rocks are discussed in terms of their primary mode of origin and geological setting; such as by eruption from a volcanic vent and extrusion as a lava flow to form a mare, and by their composition in terms of both bulk chemistry and specific mineral composition; such as basaltic composition and containing the minerals olivine, pyroxene, and plagioclase. Examples include a "pristine crystalline highland rock", "highly modified polymict breccia" or an "impact melt glass". [53] Karl von Terzaghi put it aptly in 1936 [53]:

> "Unfortunately, soils are made by nature and not by man, and the products of nature are always complex." (*Karl von Terzaghi*)

2.1.3.2. Chemical Composition

14 reference soils from Apollo 11, 12, 14, 15, 16, 17 and Luna 16, 20, 24 have provided information on the regolith's chemical composition. As a first approximation, the Al_2O_3 content of a soil shows its highland affinity and the K_2O content is a measure of its

Table 2.1.: Physical Comparison of the Moon and Earth [26]

Property	Moon	Earth
Mass	7.353×10^{22} kg	5.976×10^{24} kg
Radius (spherical)	1738 km	6371 km
Surface area	37.9×10^{6} km^2	510.1×10^{6} km^2 (land = 149.8×10^{6} km^2)
Flattening*	0.0005	0.0034
Mean density	3.34 g/cm^3	5.517 g/cm^3
Gravity at equator	1.62 m/s^2	9.81 m/s^2
Escape velocity at equator	2.38 km/s	11.2 km/s
Sidereal rotation time	27.322 d	23.9345 h
Inclination of equator/orbit	6°41'	23°28'
Mean surface temperature	380.15 K day; 120.15 K night	295.15 K
Temperature extremes	40.15 K (?) to 396.15 K	148.15 K to 331.15 K
Atmosphere	~10^4 molecules/cm^3 day 2×10^5 molecules/cm^3 night	2.5×10^{19} molecules/cm^3 (STP)
Moment of Inertia ($1/MR^2$)	0.395	0.3315
Heat flow (average)	~29 mW/m^2	63 mW/m^2
Seismic energy	2×10^{10} (or 10^{14} ?) J/yr†	10^{17}-10^{18} J/yr
Magnetic field	0 (small paleofield)	24-56 A/m

* (Equatorial - ideal)/ideal radii.

† These estimates account for moonquakes only and do not account for seismicity from meteoroid impacts.

KREEP content. Several soils that lie in the intermediate range of Al_2O_3 values (16-19 wt %) represent mare/highland mixtures. Highland soils have low TiO_2 and high Al_2O_3 values. Mare soils reflect the TiO_2 contents of the local basalts, therefore high-Ti and low-Ti mare basalts are existing. The substances SiO_2, TiO_2, Al_2O_3, FeO, MgO, CaO, Na_2O, K_2O, MnO, and Cr_2O_3 (exclusive trace elements) are part of the reference soils in varying ratios. [47]

2.1.3.3. Density

Assuming that the density on the Moon increases logarithmically with depth, z, from a finite value, ρ_0, at the surface, the density is calculated by [13]:

$$\rho = \rho_0 + \kappa \cdot \ln(z + 1) \qquad (z \text{ in cm}). \tag{1}$$

ρ_0 and κ are constant multiplying factors and can be determined explicitly from data to be $\rho_0 = 1.38$ g/cm^3 and $\kappa = 0.121$ g/cm^3 , respectively [13]. The density increases rapidly with depth, accordingly to Equation 1, however, below depths of about 1 m the increase becomes unrealistic [45].

2.2. Lunar Exploration

The Moon has been one of the main drivers and goals throughout the history of spaceflight. Several programs, past and present, have been conducted to reach the Moon. The most popular and successful of these was the Apollo program from the National Aeronautics and Space Administration (NASA) of the United States of America (USA).

2.2.1. Apollo

After Gagarin's first human space flight President John Fitzgerald Kennedy announced in 1961:

> "[...] I believe that this nation should commit itself to achieving the goal, before this decade is out, of landing a man on the moon and returning him safely to the earth." (*John F. Kennedy*)

This was the starting point for the most successful Moon mission in history of mankind. [8] Manned crews flew nine times to the Moon during this programme. Several measurements and experiments were performed on the Moon's surface during the extra-vehicular activities (EVA), as well as the collection of lunar regolith. [66]

Heat flow measurements were successfully taken during the Apollo 15 and Apollo 17 missions. Apollo 15 launched on 26 July 1971 and landed on 30 July 1971, north of the equatorial band to which Apollo landing sites had previously been restricted. Unlike previous missions, the Apollo crew had a rover which enabled them to explore a larger part of the Moon's surface. Through its utilisation, the crew was able to collect samples from the mare and nearby mountains. The last flight of the Apollo program was Apollo 17, which launched on 7 December 1972 as the only night launch. For the first time a professional geologist was part of the crew and set foot on the Moon. [66, 33]

2.2.2. Others

Numerous missions to the Moon have been launched and brought to a successful end by the USA, the Soviet Union, Japan, Europe, China and India. The first man-made spacecraft to reach the Moon's surface was Luna 2, a Soviet-built craft launched in 1959 as part of the Luna programme. Later Luna missions included sample return to Earth. All of the lunar landings, impacts, fly-bys, orbiters and return missions have been unmanned, with the exception of the Apollo flights. [65]

2.3. Heat Transfer

From the first law of Thermodynamics, heat flows through a system from hot sections to cooler sections. There are three mechanisms of heat transfer:

1. **Conduction**: Heat passes through the substance of the body itself. Depending on the material, the energy is transported by atoms, molecules, electrons or phonons.
2. **Convection**: Heat is transferred by relative motion of portions of the heated body. This motion occurs either through an external pressure difference (forced convection) or through a temperature (and therefore density) difference within the fluid (natural convection).
3. **Radiation**: Heat is directly transferred via electromagnetic radiation.

Convection and radiation are of paramount importance in liquids and gases. In solids, convection is absent and radiation usually negligible. [14, 5]

2.3.1. Fundamental Equations

The heat flow transferred in a system, such as an heat exchanger, is given by the equation for heat conduction [5]:

$$\dot{Q}_{1,2} = k \cdot A \cdot \Delta T_m. \tag{2}$$

In Equation 2, A is the contact surface area of the heat exchanger with two working fluids. It is assumed that the heat exchanger has an average heat transfer coefficient k. This holds for most cases, however if the type of heat transfer changes within one apparatus, the calculation has to be performed in sections with local heat transfer coefficients. An example of this is gas condensation.

The average logarithmic temperature difference between the entrance and exit of the heat exchanger, where at least one fluid has a constant temperature, is [5]:

$$\Delta T_m = \frac{\Delta T_b - \Delta T_s}{\ln(\Delta T_b / \Delta T_s)} \qquad \text{for} \quad \Delta T_b - \Delta T_s \neq 0, \tag{3}$$

$$\Delta T_m = \frac{\Delta T_b + \Delta T_s}{2} \qquad \text{for} \quad \Delta T_b \approx \Delta T_s. \tag{4}$$

The temperature differences between the two fluids at the entrance and the exit of the heat exchanger are accordingly c and ΔT_s. ΔT_b is the larger difference and ΔT_s the smaller

difference. This is representative of the situation on the Moon, where 0.5 m beneath the surface the regolith has a nearly constant temperature.

In the energy balance equation the heat flow is calculated by the mass flow ($\dot{m}$) and the enthalpy change of the fluids [5]:

$$\dot{Q} = \dot{m}_1 \cdot (h_{11} - h_{12}), \tag{5a}$$

$$\dot{Q} = -\dot{m}_2 \cdot (h_{21} - h_{22}). \tag{5b}$$

The enthalpy h_{11} is the enthalpy of fluid 1 at the entrance, and h_{12} is the value at the exit. Correspondingly is h_{21} the enthalpy of fluid 2 at the entrance and h_{22} at the exit. Equation 5 can be applied generally, also to multi-phase systems. [5]

2.3.2. Cryogenic Heat Transfer

A common problem arising in cryogenic systems is the prediction of thermal contact resistance in vacuum. In heat transfer between two contacting solid surfaces, the temperature changes across the contact area. Consequently, there must be a thermal resistance at the interface. The existence of a contact resistance is primarily caused by the roughness and flatness deviation of the two surfaces in contact. The contact resistance is assumed to be made up of three components:

1. **The macroscopic constriction resistance**: caused by a reduced contact area due to deviation from perfect flatness of the surfaces,
2. **The microscopic constriction resistance**: arises because the actual contact area is less than the apparent area, due to microscopic protuberances (roughness) on the surface, and
3. **The film resistance**: arises due to oxide films or other films between the surfaces. [4]

2.3.3. Heat Conduction in Granulates

The mineralogical composition, texture, water content, particle shape, and space arrangements of a soil influence its thermal conductivity. The heat conduction in granulated materials on Earth differ from those in solids, because there is heat conduction in the solid phase (particles and aggregates) as well as in the voids, which may contain air, liquid water, or water vapour. Increasing aggregate size and porosity is expected to cause decreasing thermal conductivity, due to the decrease of the number of contact points and the contact area. The heat transfer at one contact point depends on the actual contact area and the thermal properties of the mating material in between the solid particles at the contact zone. The thermal conductance of an aggregated soil phase is severely reduced because of

1. macroscopic constriction of heat flow due to reduced contact area,
2. microscopic constriction at the contact points due to surface roughness, and
3. fluid resistance at the contact point. [25]

2.4. SPG Concept

To make use of the selenothermal energy, DLR is investigating the possibility to generate electrical power by using a dynamic conversion process such as a Rankine or Stirling cycle. The proposed thermodynamic cycle for SPG is shown in Figure 2.3. Liquid nitrogen (LN), provided in a tank insulated towards the lunar surface (1), is pumped into a heat exchanger on/below the lunar surface (2), where the heat within the lunar regolith is transferred to the nitrogen, triggering vaporisation. The expanding nitrogen enters and propels a turbine (3), generating mechanical work (3). The gaseous nitrogen is fed into a second, empty tank, where it can cool down by means of a radiator and become liquid once more (4) [39]. In the Figures 2.4 and 2.5 the T,s- and p,v-diagrams of the Rankine and Stirling processes are depicted, respectively.

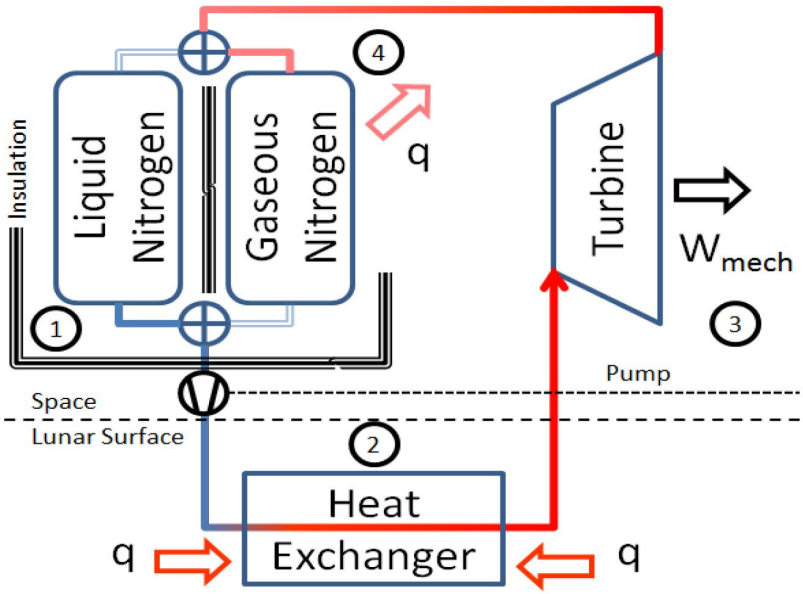

Figure 2.3.: The Proposed Thermodynamic Cycle for SPG [39].

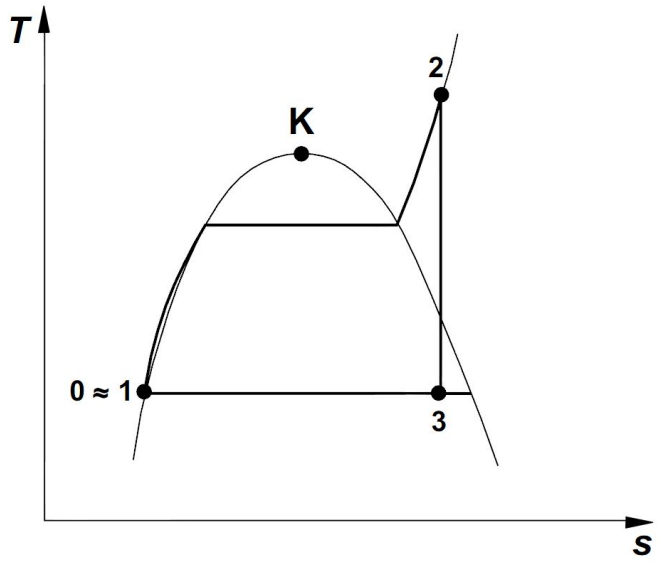

Figure 2.4.: T,s-Diagram of the Rankine cycle [38].

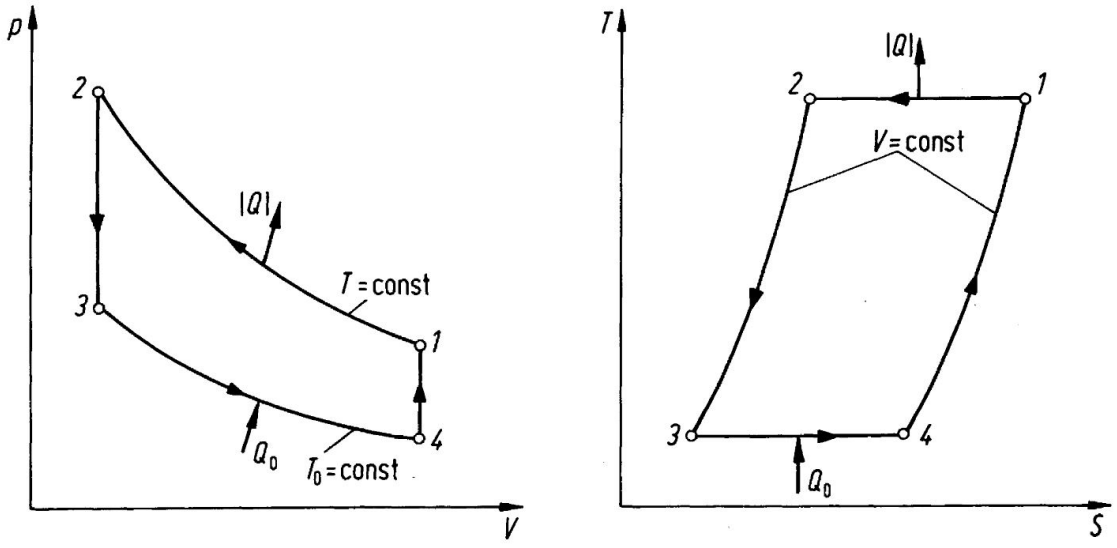

Figure 2.5.: p-V- (left) and T-S- (right) Diagram of the Stirling Cycle [55].

2.5. Heat Conductivity Measurements

In this thesis, the heat transfer coefficient, k, from lunar regolith to flowing LN in the heat exchanger shall be determined (see Section 1.3.2). In contrast to the thermal conductivity, λ, the heat transfer coefficient for regolith to a working fluid in a heat exchanger has not been previously investigated. Due to the high complexity and a large number of unknown variables, this value cannot be calculated or estimated, and must be determined experimentally. Thermal conductivity, flow properties, material constants, boundary layers, temperature and pressure all have an influence on the heat flow.

During the Apollo missions, the thermal conductivity, λ, of lunar regolith was measured, as will be shown in Section 2.5.1. An overview of further techniques for thermal conductivity measurement, commonly implemented on Earth, is provided in Section 2.5.2.

2.5.1. Apollo Experiments

The Apollo 15 and 17 heat-flow measurements have provided values for the thermal conductivity of the regolith. These results indicate that the heat conductivity of the regolith material exterior to the probe bore contact zone lies within the range $0.9 - 1.3 \cdot 10^{-4}$ W/(cm · K). This conductivity resulted in heat-flow values in the Apollo 15 and 17 measurements. At the Hadley Rille and Taurus-Littrow sites, the heat-flow values are 2.1 and 1.6 μW/cm^2, respectively. [34]

Figure 2.6 shows the temperature measurements of representative Apollo 15 and 17 heat-flow probes. Three distinct temporal components can be seen in Figure 2.6 [34]:

1. A diurnal component (Period = 29.53 days) at the sensors closest to the lunar surface.

2. Temperature-cycles with a 1-year period are detectable at all sensors within 120 cm of the surface.

3. At all sensors an aperiodic temperature rise can be seen, characterised by a decreasing magnitude and increasing time delay before onset at greater depths. This temperature rise is a result of the astronauts' activities which disrupted the thermal and radiative properties of the surface material.

2.5.2. Ground-based

On Earth, heat conductivity measurements have been performed extensively to determine the heat conductivity from different materials. Several different methods may be used, each with various advantages and disadvantages. In Table 2.2, some methods are listed with their respective properties.

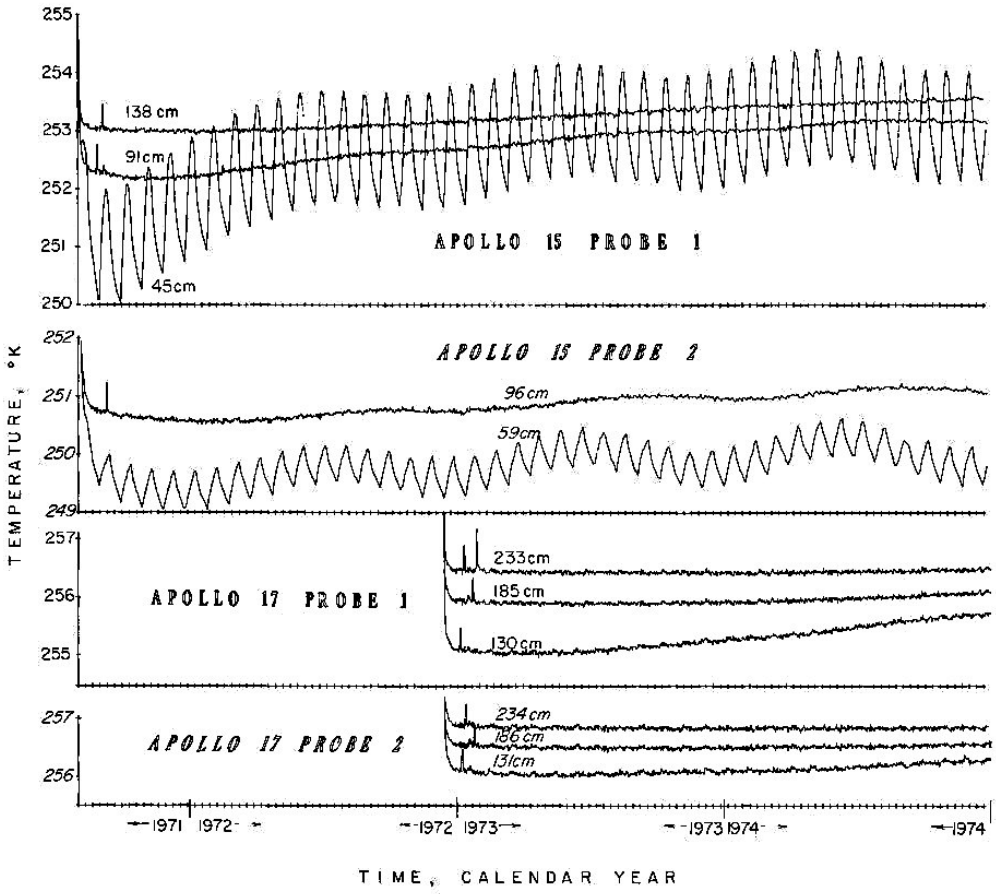

Figure 2.6.: Subsurface Temperature Histories of Representative Sensors on the Four Heat-Flow Probes, Covering 3.5 year period [34].

Table 2.2.: Comparison of Measurement Methods for the Determination of Thermal Conductivity and Thermal Diffusivity [18]

Method	Temperature range	Uncertainty	Materials	Merit	Demerit
Guarded hot plate	80 - 800 K	2 %	Insulation materials, plastics, glasses	High accuracy	Long measurement time, large specimen size, low conductivity materials
Cylinder	4 - 1000 K	2%	Metals	Temperature range, simultaneous determination of electrical conductivity and Seebeck-coefficient possible	Long measurement time
Heat flow meter	173.15 - 473.15 K	3 - 10 %	Insulation materials, plastics, glasses, ceramics	Simple construction and operation	Measurement uncertainty, relative measurement
Comparative	293.15 - 1573.15 K	10 - 20 %	Metals, ceramics, plastics, plastics [*sic*]	Simple construction and operation	Measurement uncertainty, relative measurement
Direct heating (Kohlrausch)	400 - 3000 K	2 - 10 %	Metals	Simple and fast measurements, simultaneous determination of electrical conductivity	only electrically conducting materials
Pipe method	293.15 - 2773.15 K	3 - 20 %	Solids	Temperature range	Specimen preparation, long measurement time
Hot wire, hot strip	293.15 - 2273.15 K	1 - 10 %	Liquids, gases, low conductivity solids	Temperature range, fast, accuracy	Limited to low conductivity materials
Laser flash	173.15 - 3273.15 K	3 - 5 %	Solids, liquids	Temperature range, most solids, liquids and powders, small specimen, fast, accuracy at high temperatures	Expensive, not for insulation materials
Photothermal, photoacoustic	30 - 1500 K	Insufficient knowledge	Solids, liquids, gases, thin films	Usable for thin films, liquids and gases	Nonstandard, knowledge about accuracy

2.6. Hardware

2.6.1. Sensors

Different sensors need to be applied to the test rig to determine the heat flow between the regolith simulant and the nitrogen in the heat exchanger. Temperature of the regolith and nitrogen flow must be measured, therefore several temperature sensors will be placed in the test rig. Two different kinds of temperature sensors are used; Pt100 sensors within the regolith simulant in the vacuum chamber, and thermocouples in the nitrogen flow. Pt100 sensors were chosen due to their relatively high accuracy, $(\pm(0.3°C + 0.005 \cdot |T|))$, and furthermore, are readily available and low-cost. The thermocouples for the nitrogen flow were favoured over Pt100 sensors due to their faster reaction to temperature changes. A variable area flowmeter will measure the nitrogen mass flow rate. The operating principles of these sensors shall now be discussed.

2.6.1.1. Pt100

In 1821 Sir Humphry Davy discovered that the resistivity of platinum increases with temperature. The resistance at a certain temperature, especially for temperatures below the freezing point of water, can be approximated by [40]:

$$R = \tilde{R}_0[1 + aT + bT^2 + c(T - 100)T^3]. \tag{6}$$

T is the temperature (in °C) and a, b, c are constant coefficients. This equation fits the resistivity temperature curve of platinum within ±0.02 K, from the freezing point of water down to the oxygen boiling point of 90.2 K. The coefficients for Johnson, Matthey and Company platinum are [40]:

$$a = 3.98 \cdot 10^{-3} \tfrac{1}{°C}$$

$$b = -5.85 \cdot 10^{-7} \tfrac{1}{°C}$$

$$c = -4.35 \cdot 10^{-5}$$

The temperature is determined by measuring the resistance of the sensor and an automatic conversion into Kelvin. A schematic of a Pt100 sensor is shown in Figure 2.7.

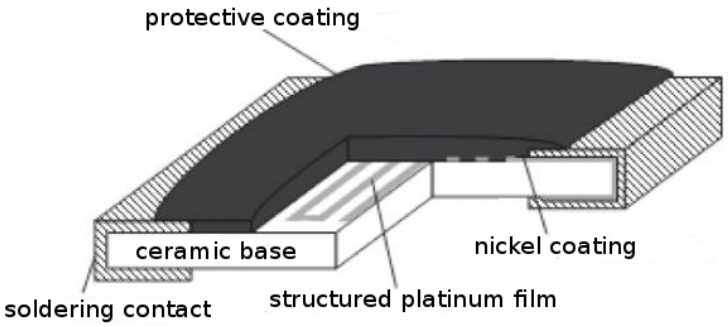

Figure 2.7.: Schematic Layout of a Metallic (Comparable to Platinum) Thin Film Resistor [27].

2.6.1.2. Thermocouples

Thermocouples convert a temperature difference into an electromotive force called the Seebeck voltage. Thermocouples are usually made from two dissimilar metal wires connected to form a complete loop, with one junction held at a reference temperature and the other junction serving as the temperature sensing device. [40] There are three laws concerning the use of thermocouples:

1. **The Law of the Homogeneous Circuit:** This is an empirical law which states that no temperature variation in a homogeneous circuit will produce a net voltage (Figure 2.8). Changes in cross-sectional area and temperature distribution have no effect. Any voltage that appears, as the result of a temperature variation in a wire, is evidence that the wire is inhomogeneous. If both legs are the same composition, no net Seebeck potential exists and no current will flow. [40]

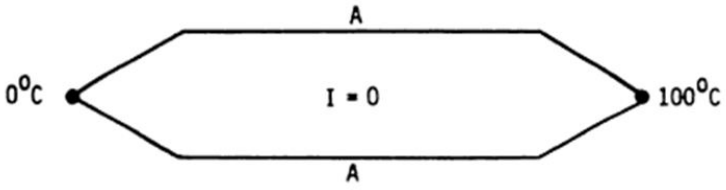

Figure 2.8.: Law of the Homogeneous Circuit [40].

2. **The Law of Intermediate Conductors at Constant Temperature:** This is a fundamental law that says no matter which dissimilar conductors are in contact, no net voltage will appear if the temperature of all the junctions is the same (Figure 2.9). This is a consequence of the second law of thermodynamics; if such a potential existed, work could be extracted without a temperature difference. In the case where both AB junctions at the same temperature, no Seebeck voltage is induced, and therefore there is no current. [40]

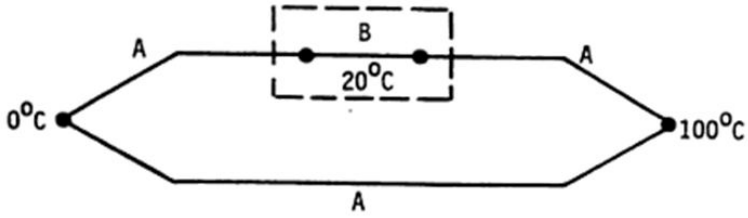

Figure 2.9.: Law of Intermediate Conductors at Constant Temperature [40].

3. **The Law of Successive Temperatures:** This is a fundamental law which states that the Seebeck voltage from a lower temperature to a higher temperature is equal to the sum of the Seebeck voltage from the lower temperature to any intermediate temperature and the Seebeck voltage from that intermediate temperature to the higher temperature (Figure 2.10). Mathematically, we have [40]

$$\int_{T_1}^{T_3} \alpha_s dT = \int_{T_1}^{T_2} \alpha_s dT + \int_{T_2}^{T_3} \alpha_s dT, \tag{7}$$

where T_2 is any intermediate temperature. As the Seebeck coefficient α_s is a function of T, the law of successive temperatures can be used to compensate for changes in reference junction potentials [40].

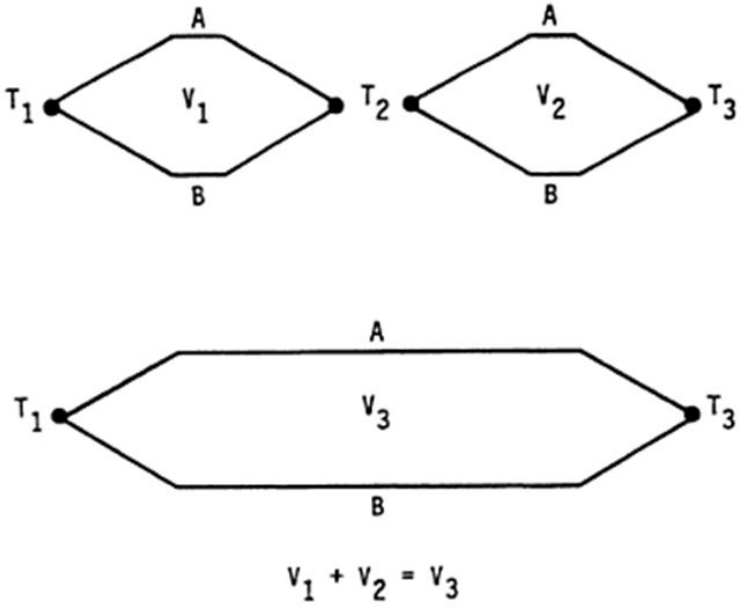

Figure 2.10.: Illustration of the Law of Successive Temperatures [40].

The calibrated thermocouples used in this test rig included a Swagelok® connection for attachment to the nitrogen pipes. It can be seen in Figure 2.11. The batch log can be found in Appendix A.3.

Figure 2.11.: Thermocouple.

2.6.1.3. Variable Area Flowmeter

The principle of the variable area flowmeter is based on a swimmer, which is immersed in the fluid. Either the swimmer or the measuring tube is conical, therefore generating a change in the swimmer drag coefficient as a function of its height. The height is also a function of the flow mass-rate. When the flow increases, the fluid imparts more force on the swimmer and moves it upwards [6], see also Figure 2.12 (right). In this test rig a Krohne H250 flowmeter, as seen in Figure 2.12 (left) is used, see reference [24].

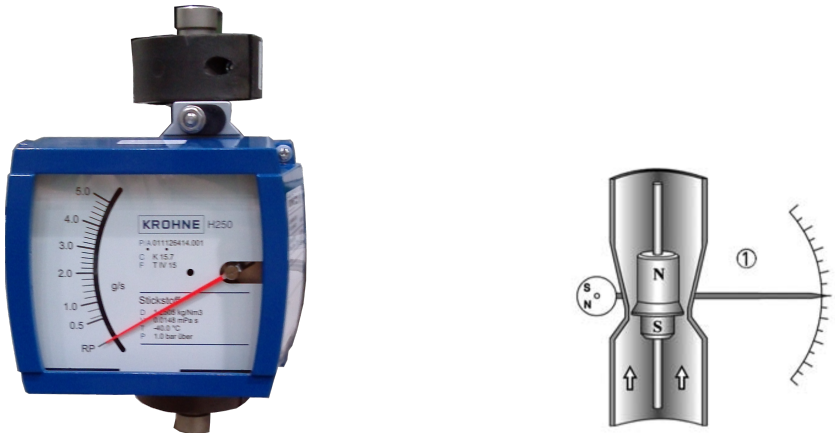

Figure 2.12.: Krohne H250 Variable Area Flowmeter (left) and its Operating Principle [24] (right).

2.6.2. Nitrogen

Nitrogen (N_2) is colourless, odourless, and extremely inert. At 273.15 K and 0.1013 MPa it is gaseous and has a density of 1.2505 kg/m^3. The triple point is at 63.15 K and 12.5 kPa. The boiling point is at 77.35 K and 0.1013 MPa. Its enthalpy of vaporisation (h_v) is 198.9 kJ/kg at 0.1013 MPa pressure [56].

2.6.2.1. Thermal Conductivity

According to Lemmon and Jacobsen [36], the thermal conductivity of nitrogen is a function of temperature and density:

$$\lambda = \lambda^0(T) + \lambda^r(\tau, \delta) + \lambda^c(\tau, \delta). \tag{8}$$

λ is the thermal conductivity in mW/(m·K), λ^0 is the dilute gas thermal conductivity, λ^r is the residual fluid thermal conductivity, λ^c is the thermal conductivity critical enhancement, $\tau = T_c/T$, and $\delta = \rho/\rho_c$. For nitrogen, $T_c = 126.192$ K and $\rho_c = 11.1839$ mol/dm^{-3}, as seen in Table 2.3. The dilute gas contribution is given by

Table 2.3.: Parameters of the Viscosity and Thermal Conductivity Equations for Nitrogen [36]

Parameter	Value	
$\mathbf{T_c}$	126.192	K
$\boldsymbol{\rho_c}$	11.1839	$\frac{\text{mol}}{\text{dm}^3}$
$\mathbf{p_c}$	3.3958	MPa
$\mathbf{M}$	28.01348	$\frac{\text{g}}{\text{mol}}$
$\frac{\boldsymbol{\epsilon}}{\mathbf{k}}$	98.94	K
$\boldsymbol{\sigma}$	0.3656	nm
$\boldsymbol{\zeta_0}$	0.17	nm
$\boldsymbol{\Gamma}$	0.055	
$\mathbf{q_d}$	0.4	nm
$\mathbf{T_{ref}}$	252.384	K

[36]:

$$\lambda^0 = N_1 \left[\frac{\eta^0(T)}{1\mu\text{Pa} \cdot \text{s}} \right] + N_2 \tau^{t_2} + N_3 \tau^{t_3}, \tag{9}$$

where η^0 is the dilute gas viscosity. The coefficients and exponents are given in Table 2.4. The residual contribution to the thermal conductivity is given in mW/(m·K) by [36]:

$$\lambda^r = \sum_{i=4}^{n} N_i \tau^{t_i} \delta^{d_i} \exp(-\gamma_i \delta^{l_i}), \tag{10}$$

where $\gamma_i = \begin{cases} 0, & \text{when } l_i = 0 \\ 1, & \text{when } l_i \neq 0 \end{cases}$. The coefficients and exponents are also given in Table 2.4. The thermal conductivity critical enhancement to calculate the fluid properties in the critical region is [36]:

$$\lambda^c = \rho c_p \frac{k_B R_0 T}{6\pi\xi\eta(T, \rho)} (\tilde{\Omega} - \tilde{\Omega}_0), \tag{11}$$

where [36]

$$\tilde{\Omega} = \frac{2}{\pi} \left[\left(\frac{c_p - c_v}{c_p} \right) \tan^{-1} \left(\frac{\xi}{q_D} \right) + \frac{c_v}{c_p} \left(\frac{\xi}{q_D} \right) \right], \tag{12}$$

Table 2.4.: Coefficients and Exponents of the Residual Fluid Thermal Conductivity Equation for Nitrogen [36]

i	N_i	t_i	d_i	l_i
1	1.511			
2	2.117	-1.0		
3	-3.332	-0.7		
4	8.862	0.0	1	0
5	31.11	0.03	2	0
6	-73.13	0.2	3	1
7	20.03	0.8	4	2
8	-0.7096	0.6	8	2
9	0.2672	1.9	10	2

and [36]

$$\tilde{\Omega}_0 = \frac{2}{\pi}\left[1 - \exp\left(\frac{-1}{(\xi/q_D)^{-1} + \frac{1}{3}(\xi/q_D)^2(\rho_c/\rho)^2}\right)\right]. \tag{13}$$

The correlation length ξ is given by [36]:

$$\xi = \xi_0\left[\frac{\tilde{\chi}(T,\rho) - \tilde{\chi}(T_{ref},\rho)\frac{T_{ref}}{T}}{\Gamma}\right]^{\nu/\gamma}, \tag{14}$$

where [36]

$$\tilde{\chi}(T,\rho) = \frac{p_c\rho}{\rho_c^2}\left(\frac{\partial\rho}{\partial p}\right). \tag{15}$$

In these equations, k_B is Boltzmann's constant ($1.380658 \cdot 10^{-23}$ J/K), and R_0, ν, and γ are theoretically based constants with values of $R_0 = 1.01$, $\nu = 0.63$, and $\gamma = 1.2415$. The terms q_D, ξ_0, and Γ are fluid-specific (fitted) terms, and T_{ref} is a reference temperature that is significantly above the critical temperature (Lemmon and Jacobsen [36] chose T_{ref} as twice the critical temperature). The values of these terms are given in Table 2.3. The value of λ_c should be set to zero when the bracketed term in equation 14 is negative (usually at high temperatures) or zero. The isochoric heat capacity (c_v), isobaric heat capacity (c_p), and the first derivative of density with respect to pressure are calculated from the equation of state at the specified temperature and density. [36]

2.6.2.2. Heat Capacity

The heat capacity of nitrogen is a function of temperature, density and pressure. Liquid nitrogen at atmospheric pressure (mean sea level pressure: p = 0.101325 MPa) at the boiling point (T = 77.35 K) has a density of 806.62 kg/m^3 and heat capacities of $c_v = 29.9$ J/(mol · K), and $c_p = 57.21$ J/(mol · K), respectively. In the gaseous phase at atmospheric pressure at the boiling point nitrogen has a density of 4.621 kg/m^3 and heat capacities of $c_v = 26.27$ J/(mol · K), and respectively $c_p = 37.56$ J/(mol · K). [28]

2.6.2.3. Leidenfrost Effect

The Leidenfrost effect results from the lower heat conduction of gases in comparison to solids. A liquid drop on a much hotter solid layer does not vaporise immediately but instead "floats" on the layer for a longer period of time. The arising vapour cloud protects the drop of encountering the hot layer beneath. [59] The Leidenfrost effect is shown in Figure 2.13. This effect could hamper the heat transfer to the nitrogen in the heat exchanger.

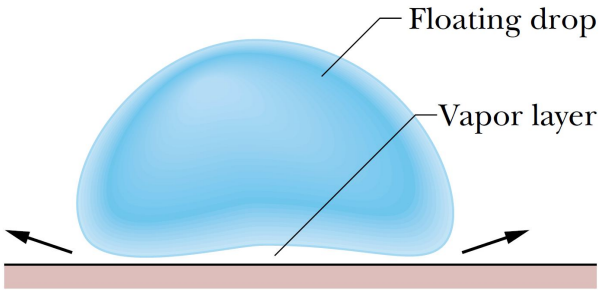

Figure 2.13.: A Leidenfrost Drop in Cross Section [64].

2.6.3. Sliding Vane Rotary Pump

The operating principle of a sliding vane rotary pump can be seen in Figure 2.14, and is defined in DIN 28400 [31]:

> "A sliding vane rotary vacuum pump is a rotary vacuum pump in which an eccentric rotor slides tangentially along the interior wall of the stator (housing). Two or more (usually radially) movable vanes arranged in rotor slots slide along the interior wall of the stator and divide the pump chamber into cavities with variable volumes."

In order to generate low ultimate pressures, an oil film is used to improve gap sealing. Boreholes and channels maintain an overall supply with oil between case lids and fore-parts of rotor and vanes, and help the vanes to push forward a small wave of oil continuously between the compression and suction volumes. Additional functions of the working fluid include corrosion protection and cleaning, particularly in contaminated applications. The operating fluid absorbs the fat and dust that enters the pump. [31]

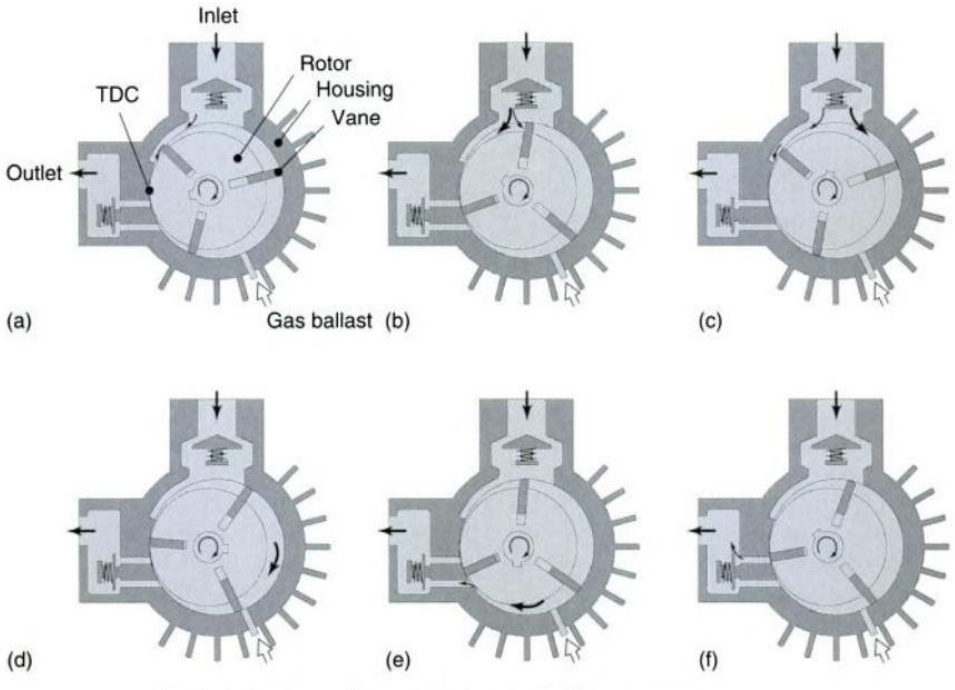

Figure 2.14.: Sliding Vane Rotary Pump [31].

3. Artificial lunar soils

Artificial lunar soil was defined by McKay and Blacic in [41] as

> "Any material manufactured from natural or synthetic terrestrial or meteoritic components for the purpose of simulating one or more physical and/or chemical properties of a lunar rock or soil." (*David S. McKay, James D. Blacic*)

In this thesis only one physical property of the regolith shall be simulated; the heat conductivity of lunar soil. With this focus, different simulants are presented and assessed in the following subsections.

3.1. Figures of Merit (FoM)

The FoM provides a means for formal, quantitative comparison of two particulate materials composed of geologic components. A reference material serves as the benchmark against which a second material is compared. The FoM addresses four material attributes. These are:

- Particle Type/Composition,
- Particle Size Distribution,
- Particle Shape Distribution, and
- Density. [51]

3.2. FJS

FJS-1, FJS-2 and FJS-3 (Fuji Japanese Simulant 1-3) are three simulants produced in Japan by JAXA and Shimizu Corporation. They consist of basalt from Mt. Fuji, ilmenite from Florida, and olivine from the Horoman and Hokkaido islands. These contents were crushed and physically mixed. FJS-1 was produced to simulate Apollo 16 highland regolith, FJS-2 for Apollo 14 KREEP regolith and FJS-3 for Apollo 11 high-Ti regolith. The exact ratios can be seen in Table 3.1. [12]

Table 3.1.: Comparison of FJS-1, FJS-2 and FJS-3 [12]

Oxide	FJS-1	FJS-2	FJS-3
SiO_2	49.1	49.7	46.0
TiO_2	1.9	1.7	6.7
Al_2O_3	16.2	14.8	13.7
Cr_2O_3	-	-	-
Fe_2O_3	4.8	4.7	5.9
FeO	8.3	8.2	7.9
MnO	0.19	0.19	0.28
MgO	3.8	8.1	7.3
CaO	9.1	8.4	7.8
Na_2O	2.8	2.6	2.6
K_2O	1.0	0.92	0.87
P_2O_5	0.44	0.4	0.39
LOI	0.43	0.47	0.58
Total	**98.1**	**100.2**	**100**

3.3. BP-1

The BP-1 (Black Point 1) simulant is made from the Black Point basalt flow, San Francisco Volcanic field, in northern Arizona [57]. An analysis of the major components of BP-1 is listed in Table 3.2.

Table 3.2.: XRF Analyses of BP-1 Splits [57]

Oxide	Bag 1	Bag 2	Bag 3	Bag 4	Bag 5	Bag All
SiO_2	45	44	44	43	45	44
Al_2O_3	16	18	18	16	17	17
Fe_2O_3	11	11	11	13	9	11
MgO	10	7	7	9	9	8
CaO	13	13	13	12	14	14
Na_2O	3	4	4	4	2	3
K_2O	0	0	0	0	0	0
CO_2	1	2	2	1	2	3
SO_2	0	0	0	2	1	0
Total	**99**	**99**	**99**	**100**	**99**	**100**

3.4. MLS-1 & JSC-1

MLS-1 (Minnesota Lunar Simulant) was produced in the 1970s and JSC-1 (Johnson Space Center Number 1) in the 1990s. These materials target lunar mare basalts of differing composition. MLS-1 matches the composition of a high-Ti Apollo 11 basalt and JSC-1 matches an average Apollo 14 mare basalt (see Table 3.3). [53]

Table 3.3.: Comparison of JSC-1 and MLS-1 with Targeted Apollo Composition (Values in Oxide wt. %) [53]

Oxide	JSC-1	Apollo 14 Average Soil	MLS-1	Apollo 11 Soil 10002
SiO_2	47.71	48.1	43.9	42.2
TiO_2	1.59	1.7	6.3	7.8
Al_2O_3	15.02	17.4	13.7	13.6
Cr_2O_3	0.04	0.23	-	0.3
Fe_2O_3	3.44	-	2.6	-
FeO	7.35	10.4	13.4	15.3
MnO	0.18	0.14	0.2	0.2
MgO	9.01	9.4	6.7	7.8
CaO	10.42	10.7	10.1	11.9
Na_2O	2.7	0.7	2.1	0.47
K_2O	0.82	0.55	0.2	0.16
P_2O_5	0.66	0.51	-	0.05
LOI	0.71	-	-	-
Total	**99.65**	**99.8**	**99.20**	**99.9**

Simulant JSC-1A was created to match as closely as possible the composition and grain size distribution of the original JSC-1 lunar regolith simulant. Simulant JSC-1AF ("fine fraction") has been processed by additional milling and sieving to possess a significantly smaller grain size in order to approximate the finer component of the lunar regolith where more than 50% of the grain sizes are below 20 microns. [49]

The particle density of JSC-1A is 2928 kg/m^3 [32]. However, the density of the sand is not equal to the particle density, as the particles are not tightly packed and there is still empty space between each particle. According to [68], the maximum density of JSC-1A is 2036 kg/m^3.

The thermal conductivity of JSC-1A under vacuum conditions (10^{-5} mbar) was determined for high temperatures by TU München (see Table 3.4).

Table 3.4.: Measured Thermal Conductivity of JSC-1A [48]

T [K]	λ [W/(m·K)]
523.15	8.9 $\times 10^{-3}$
773.15	15.3 $\times 10^{-3}$
1023.15	25.3 $\times 10^{-3}$
1173.15	33.3 $\times 10^{-3}$

3.5. Selection of Regolith Simulant

JSC-1A was chosen as a simulant, mainly because of its availability. Most of the simulants are not produced anymore and just a few are commercially sold. JSC-1A has some definite advantages, e. g. its good chemical conformity with actual lunar regolith. Most geotechnical properties of JSC-1A are similar to that of lunar soils, except the cohesion [68]. But it also has some disadvantages. One disadvantage is the lack of some data for JSC-1A, like the heat capacity. Another disadvantage is that JSC-1A evolves both H_2O and CO_2 at multiple temperatures which could lead to unpredictable effects occurring during tests [58].

3.6. Heat Capacity of JSC-1A

Unfortunately, there currently exists no experimental data concerning the heat capacity of JSC-1A. This value can be estimated with the constituent's mass fraction and heat capacity with the following equations. The specific heat capacity is defined as [16]:

$$\begin{aligned} c_p &= \left(\frac{\partial h}{\partial T}\right)_{p=const} \\ &= \left(\frac{\partial u + p\partial v}{\partial T}\right)_{p=const}. \end{aligned} \tag{16}$$

The volume change with temperature can be neglected for solids, $\partial V = 0$. For a mixture of solids the specific internal energy (u) can be added up from its constituents:

$$\begin{aligned} c_p &= \left(\frac{\partial u}{\partial T}\right)_{p=const} \\ &= \frac{\sum_{i=1}^{n} y_i \cdot \partial u_i}{\partial T} \\ &= \sum_{i=1}^{n} y_i \cdot c_{p_i}. \end{aligned} \tag{17}$$

The constituents' specific heat capacities can be determined from their molar masses (see Table 3.5) and heat capacities (see Table 3.6) by:

$$c_p = \frac{C}{M}. \tag{18}$$

Table 3.5.: Molar Mass and Density of Solid Binary Oxides at 293.15 K [1, 19, 63]

Oxide	M [g/mol]	ρ [g/cm³]
SiO_2	60.09 [1]	2.648 [63]
TiO_2	79.9 [63]	4.23 [63]
Al_2O_3	101.96 [1]	4.05 [63]
Fe_2O_3	159.69 [1]	5.25 [63]
FeO	71.846 [63]	5.745 [63]
MnO	70.94 [19]	5.45 [19]
MgO	40.31 [1]	3.576 [63]
CaO	56.08 [1]	3.4 [63]
Na_2O	61.98 [63]	2.27 [63]
K_2O	94.203 [63]	2.32 [63]
P_2O_5	141.96 [63]	2.114 [63]

Table 3.6.: Heat Capacity of Solid Binary Oxides at 298.15 K [35]

Oxide	Phase	C_m [J/(mol · K)]
SiO_2	Quartz(L)	44.42
TiO_2	Rutile	55.10
Al_2O_3	Sol	79.01
Fe_2O_3	Sol-A	104.77
FeO	Sol	48.04
MnO	Sol	44.76
MgO	Sol	37.26
CaO	Sol	42.42
Na_2O	Sol-A	68.56
K_2O	Sol	84.53
P_2O_5	Sol	100.769 [22]

The mass fraction of JSC-1A's constituents as well as their calculated specific heat capacities (c_p) are given in Table 3.7.

After substituting in all these values into Equation 17, a total specific heat capacity of 753.32 J/(kg·K) can be estimated as the heat capacity of JSC-1A. It has to be taken into account that this rough estimation has a few inaccuracies. The mass fractions are just average values for JSC-1A and are not explicitly measured for the sample used, and that it is not one solid material but a mixture with voids in between.

Table 3.7.: Mass Fractions and Specific Heat Capacities of JSC-1A's Constituents [49]

Oxide	JSC-1A average [wt%]	c_p at 298.15 K [J/(kg·K)]
SiO_2	46.67	739.22
TiO_2	1.71	689.61
Al_2O_3	15.79	774.91
Fe_2O_3	3.41 (JSC-1AF [46])*	656.08
FeO	7.57 (JSC-1AF [46])*	668.65
MnO	0.19	630.96
MgO	9.39	924.34
CaO	9.9	756.42
Na_2O	2.83	1106.16
K_2O	0.78	897.32
P_2O_5	0.71	709.84

* Note: JSC-1AF characterisation values are used here due to a discrepancy in the JSC-1A iron oxide data.

4. Test Rig Design

4.1. Requirements and Boundary Conditions

Heat Conduction is influenced by many environmental factors. For a valid investigation into the heat conduction process on the Moon, the conditions of the test rig need to be close to those on the Moon. To achieve this goal, critical requirements, with descriptions, are provided in Table 4.1.

Table 4.1.: Test Rig Requirements

	Requirement	Description	Value	Chapter
R1	Regolith	The simulant shall provide the same heat conductivity as real regolith.	-	3.4
R2	Vacuum	The Moon has no atmosphere which is an essential contributor to heat conductivity on Earth. The test rig environment shall be vacuum condition.	0 Pa	2.6.3
R3	Test Setup	The setup shall reflect the relevant parts of the SPG setup.	-	4.3.2

Additionally to the requirements, some boundary conditions are defined for the test rig. The temperature at a depth of 0.5 m underneath the lunar surface has a near constant value of 250 K. The lower gravity on the Moon which is just 1.622 m/s^2, about 17% of that on Earth [30] causes a smaller compression of the regolith than on Earth. The bulk density of the regolith can be calculated by:

$$\begin{aligned} \rho &= \frac{m}{V} \\ &= \frac{m}{z \cdot A}, \end{aligned} \tag{19}$$

with the Volume V defined by depth z and area A. According to Newton's second law the mass m can be calculated by:

$$m = \frac{F}{g}, \tag{20}$$

and is directly proportional to the weight force F and inversely proportional to the gravitational acceleration g. This implies that a lower pile of regolith simulant on Earth achieves

the same compression as a greater depth on the Moon.

$$\begin{aligned} \rho_E &= \rho_M \\ \frac{m_E}{z_E \cdot A} &= \frac{m_M}{z_M \cdot A} \\ \frac{F}{g_E \cdot z_E \cdot A} &= \frac{F}{g_M \cdot z_M \cdot A} \\ \Leftrightarrow g_e \cdot z_E &= g_M \cdot z_M \end{aligned} \tag{21}$$

By rearranging this formula the needed depth of regolith on Earth can be calculated from a given depth on the Moon:

$$\begin{aligned} z_E &= \frac{g_M}{g_E} \cdot z_M \\ z_E &= 0.17 \cdot 0.5 \text{ m} \\ &= 8.5 \text{ cm}. \end{aligned} \tag{22}$$

For example, to achieve the same compression of 0.5 m depth on the Moon, just 8.5 cm of regolith is needed on Earth.

4.2. Design

The design of the test rig can be seen in Figure 4.1 and the Catia model in Figure 4.2. The liquid nitrogen is stored in a pressurised tank. A valve controls the flow of the liquid nitrogen out of the reservoir. The temperature of the nitrogen is measured with thermocouples at the inlet and outlet of the vacuum chamber, and before the flow-rate sensor. The latter is used to verify that the temperature of the nitrogen is not below 233.15 K in order to ensure the correct functionality of the flow-rate sensor. The temperature distribution is determined with several Pt100 sensors inside the regolith simulant. During the experiment, the simulant can be heated by a heating wire, integrated in a spiral-shape on the base of the inner container. A pneumatic-flow diagram of the system is provided in Figure 4.3.

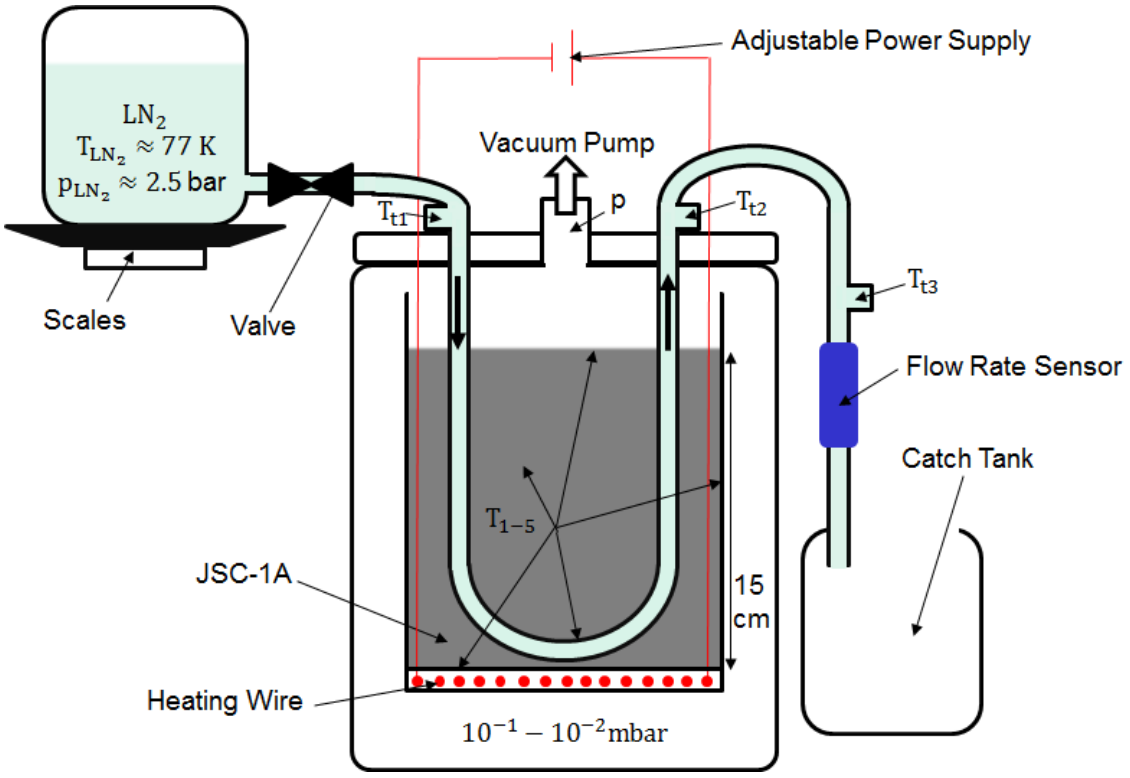

Figure 4.1.: Test Rig Schematic.

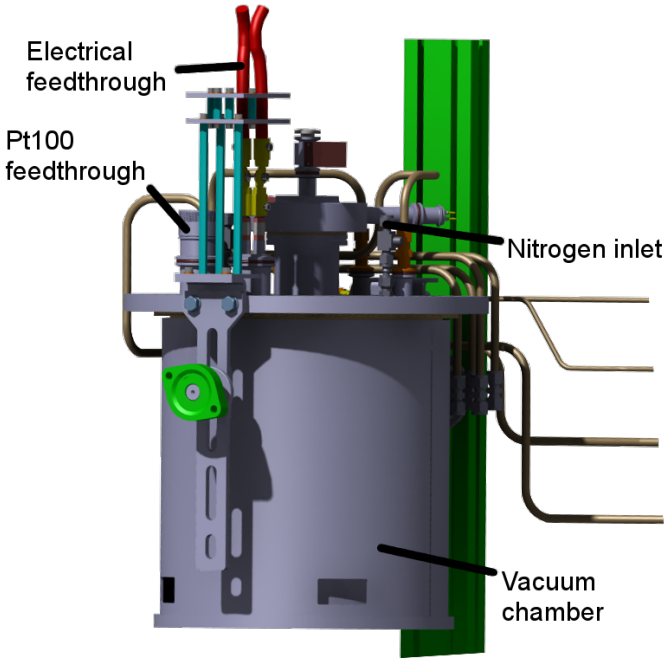

Figure 4.2.: Catia Test Rig Model.

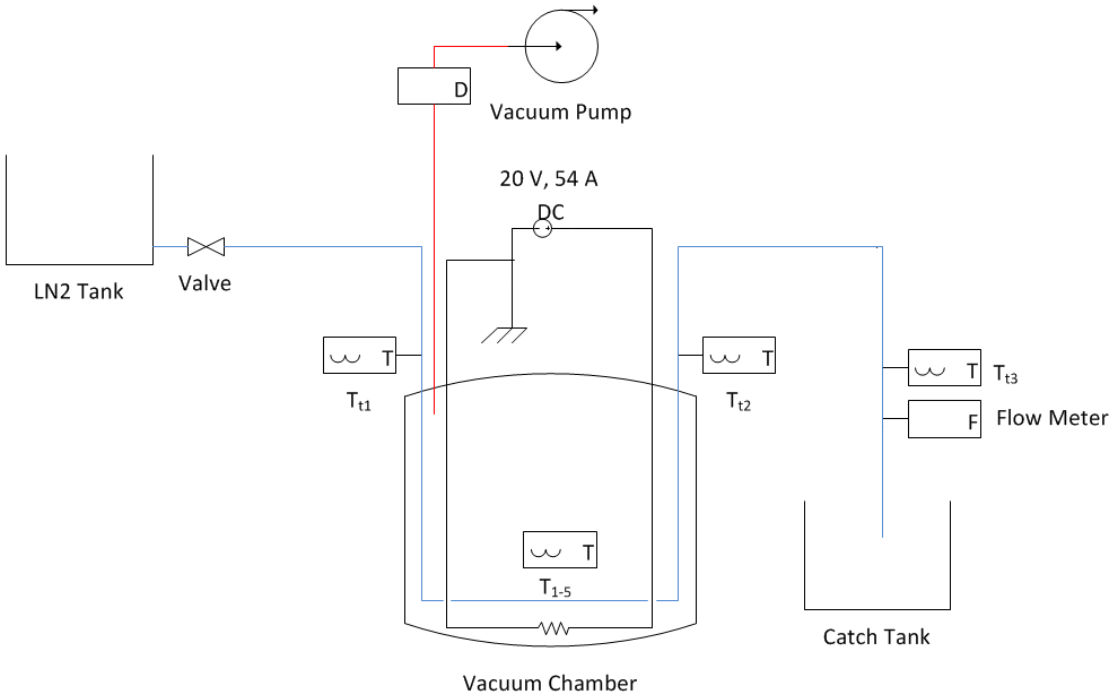

Figure 4.3.: Piping Plan.

4.3. Components

4.3.1. Overview

To model the SPG setup and to determine the heat transfer, different components are needed for the test rig:

- For the SPG setup:
  - Artificial lunar soil (see Chapter 3),
  - Heat exchanger;
- For the heat transfer measurements:
  - Temperature sensors:
    - Pt100 (see Chapter 2.6.1.1),
    - Thermocouples (see Chapter 2.6.1.2),
  - Flowmeter (see Chapter 2.6.1.3);
- For the lunar environment:
  - Vacuum chamber,
  - Vacuum pump (see Chapter 2.6.3).

4.3.2. Heat Exchanger

To fulfil the objectives from the task description, a heat exchanger containing the liquid nitrogen (LN) needs to be embedded within the regolith. The selection of the heat exchanger was based on the objective to reduce complexity in construction and calculation. A simple U-shaped tube was selected. The heat flow can be calculated using Equation 5 by measuring the temperature of the fluid before entering and after leaving the heat exchanger.
The maximum heat flow in the heat exchanger can be calculated with a modified version of Equation 5:

$$\dot{Q} = \dot{m} \cdot \Delta h. \tag{23}$$

Due to the phase change in the heat exchanger, the difference in enthalpy can be calculated as:

$$\begin{aligned} \Delta h &= (h_b - h_a) \\ &= c_p \cdot \Delta T + h_v \\ &= c_p \cdot (T_b - T_a) + h_v, \end{aligned} \tag{24}$$

where Δh is the difference in enthalpy and c_p is the isobaric heat capacity. The indices a and b are an alphabetical numbering and indicating the entrance (a) and the exit (b) of the heat exchanger. According to Chapter 2.6.2, the enthalpy of vaporisation (h_v) has a value of 198.9 kJ/kg. The temperature at the entrance (T_a) has a minimum of 77.36 K (boiling point) and at the exit (T_b) has a maximum of 250 K (temperature of the regolith).

Due to the Leidenfrost effect outlined in Chapter 2.6.2.3, a non-laminar flow in the heat exchanger is required for a more complete mixing of the vapour and fluid phase, and therefore a more effective heat exchange. Pipe flow is laminar when the Reynolds number, $\mathbf{Re}$, is smaller than the critical Reynolds number, $\mathbf{Re_c}$ [44]:

$$\mathbf{Re} = \frac{\rho v d}{\eta} < \mathbf{Re_c} = 2300, \tag{25}$$

where ρ is the density, v is the velocity, η is the dynamic viscosity of the nitrogen and d is the diameter of the pipe. For higher Reynolds numbers the flow turns turbulent. The pipe flow is turbulent for Reynolds numbers greater than 4000 [52]:

$$\mathbf{Re} = \frac{\rho v d}{\eta} \overset{!}{>} 4000. \tag{26}$$

The minimum velocity for non-laminar flow can be calculated with Equation 25. The dynamic viscosity is a function of temperature and density, and can therefore be determined by [36]:

$$\eta = \eta^0(T) + \eta^r(\tau, \delta), \tag{27}$$

where η is the viscosity in $\mu Pa \cdot s$, η^0 is the dilute gas viscosity, η^r is the residual fluid viscosity, $\tau = T_c/T$, and $\delta = \rho/\rho_c$. The critical parameters T_c and ρ_c are given in Table 2.3. The dilute gas contribution is given by [36]:

$$\eta^0(T) = \frac{0.0266958\sqrt{MT}}{\sigma^2 \Omega(T^*)}, \tag{28}$$

where σ is the Lennard-Jones size parameter and Ω is the collision integral given by [36]:

$$\Omega(T^*) = \exp\left(\sum_{i=0}^{4} b_i [\ln(T^*)]^i\right), \tag{29}$$

where $T^* = \frac{T}{(\epsilon/k)}$ and ϵ/k is the Lennard-Jones energy parameter. The Lennard-Jones parameters are given in Table 2.3, and the coefficients b_i are given in Table 4.2. The residual fluid contribution to the viscosity is given (in $\mu Pa \cdot s$) by [36]:

$$\eta^r(\tau, \delta) = \sum_{i=1}^{n} N_i \tau^{t_i} \delta^{d_i} \exp(-\gamma_i \delta^{l_i}), \tag{30}$$

where $\gamma_i = \begin{cases} 0, & \text{when } l_i = 0 \\ 1, & \text{when } l_i \neq 0 \end{cases}$ [36]. The coefficients and exponents of this equation are given in Table 4.3.

Table 4.2.: Coefficients of the Collision Integral Equation [36]

i	b_i
0	0.431
1	-0.4623
2	0.08406
3	0.005341
4	-0.00331

Table 4.3.: Coefficients and Exponents of the Residual Fluid Viscosity Equation for Nitrogen [36]

i	N_i	t_i	d_i	l_i
1	10.72	0.1	2	0
2	0.03989	0.25	10	1
3	0.001208	3.2	12	1
4	-7.402	0.9	2	2
5	4.620	0.3	1	3

The liquid nitrogen will will be at the boiling point when entering the heat exchanger, with the properties $T_{LN} = 77.35$ K, $\rho_{LN} = 808$ g/l $= 808$ kg/m^3 [56]. From Equation 27, the dynamic viscosity is $\eta = 162.645$ $\mu Pa \cdot s$ at the boiling point. By transposing Equation 25 and using a pipe of 6 mm diameter, the minimum velocity for non-laminar flow is:

$$v = \frac{\mathbf{Re} \cdot \eta}{\rho d} \overset{!}{>} 0.077 \ \frac{m}{s}. \tag{31}$$

From this, the mass flow can be calculated by

$$\dot{m} = \rho \cdot v \cdot A = 1.759 \ g \cdot s^{-1}. \tag{32}$$

The low temperature of LN is held constant for storage by very slow boiling of the liquid. Due to this reason, the liquid nitrogen used in this experiment is always at boiling temperature. The maximum possible difference in enthalpy occurs if the nitrogen is heated up from its boiling point ($T_{LN} =$ 77.35 K at ambient pressure) to the regolith temperature (T = 250 K). The heat capacity rises with decreasing temperature and reaches 1.102 kJ/(kg· K) at T = 83.15 K and p = 0.1 MPa [15]. Using these values in Equation 24:

$$\begin{aligned} \Delta h &= c_p \cdot (T_b - T_a) + h_v \\ &= 1.102 \ \frac{kJ}{kgK} \cdot (250 \text{ K} - 77.35 \text{ K}) + 198.9 \ \frac{kJ}{kg} \\ &= 389.16 \ \frac{kJ}{kg}. \end{aligned} \tag{33}$$

Substituting into Equation 23 gives the maximal possible heat flow from the regolith to the nitrogen in the heat exchanger:

$$\begin{aligned} \dot{Q} &= \dot{m} \cdot \Delta h \\ &= 3.066 \ \frac{g}{s} \cdot 389.16 \ \frac{kJ}{kg} \\ &= 1139.16 \ \frac{J}{s} \\ &= 1139.16 \text{ W}. \end{aligned} \tag{34}$$

Originally, it was planned to use a non-pressurised tank for the nitrogen and to use the height difference between the nitrogen reservoir and the catch tank to create a nitrogen flow. This solution was discarded in favour of a pressurised tank, which has the distinct advantage in its ability to provide a constant fluid velocity. A non-pressurised tank provides non-uniform velocity due to decreasing potential as the fluid level drops. For the sake of comparison, calculations performed to determine the required height difference for the non-pressurised tank will be provided. The Bernoulli equation (Equation 35) is used to determine the nitrogen reservoir height required to achieve non-laminar flow in the heat exchanger:

$$p_1 + \rho_1 g H_1 + \frac{\rho_1}{2} v_1^2 = p_2 + \rho_2 g H_2 + \frac{\rho_2}{2} v_2^2 + \zeta \frac{\rho_2}{2} v_2^2. \tag{35}$$

With $p_1 = p_2 = p_a$, and the velocity in the reservoir, $v_1 = 0$. ζ is the pressure loss coefficient expressed as a function of the length l, the diameter d and the pipe friction factor f of the pipe

$$\zeta = f \frac{l}{d}. \tag{36}$$

Therefore, Equation 35 can be simplified to

$$\rho_1 g H_1 = \rho_2 g H_2 + \frac{\rho_2}{2} v_2^2 + f \frac{l}{d} \frac{\rho_2}{2} v_2^2. \tag{37}$$

By transposing Equation 37 and neglecting the density variations, the height difference can be calculated:

$$\Delta H = (H_1 - H_2) = \frac{v_2^2}{2g} \left(1 + f \frac{l}{d} \right). \tag{38}$$

With the equation of Prandtl-Kármán-Nikuradse for hydraulic rough pipes, f can be calculated [50]:

$$f = \left[-2 \cdot \log_{10}\left(\frac{R_s}{3.71 \cdot d}\right)\right]^{-2}. \tag{39}$$

Substituting Equation 39 into Equation 38:

$$\Delta H = (H_1 - H_2) = \frac{v_2^2}{2g} \cdot \left[1 + \frac{l}{d}\left[-2 \cdot \log_{10}\left(\frac{R_s}{3.71 \cdot d}\right)\right]^{-2}\right]. \tag{40}$$

v_2, the velocity at the heat exchanger outlet, can be determined as the minimum velocity for non-laminar flow from Equation 31. Using this value for v_2, a surface roughness coefficient of $R_s = 0.05$ mm and a pipe length of 5 m, the needed height difference is approximately 9.28 mm. Therefore, there will always be a non-laminar flow for height differences exceeding 9.28 mm.

The exterior surface of the heat exchanger immersed in the regolith is 12,328.61 mm^2. This value will be utilised following the experiment, for the heat transfer evaluation.

4.3.3. Heating System

A heating device is needed to maintain the regolith simulant at a constant 250 K, due to cooling by the LN. The energy to be produced by the heater is equivalent to the energy that is transferred to the nitrogen in the heat exchanger. This value was calculated in Equation 34 to be at maximum 1139.16 W. The electronic components in this heating system will now be outlined briefly.

4.3.3.1. Power Supply

Electrical power is given by:

$$P = U \cdot I. \tag{41}$$

Power (P) is therefore proportional to both the voltage (U) and current (I). A low voltage is desirable to limit arcing, therefore a power supply with high current is needed to transfer high power to the regolith simulant. For the experiment, a 3.3 kW power supply (Gen 20-165) with an maximum output voltage of 20 V and maximum output current of 165 A is used.

4.3.3.2. Heating Wire

The heating wire to maintain the regolith simulant at a constant temperature of 250 K, countering cooling by the liquid nitrogen, is made of constantan and has a diameter of 4 mm. The resistance of the wire is 0.039 Ω/m. The melting point of constantan is 1493.15 K - 1543.15 K. At an operating point of 54 A, the wire has a temperature of 573.15 K. To insulate the wire electrically, heat shrink tubing made out of Polytetrafluoroethylene (PTFE) is fitted to it (see Figure 4.4). The current through the heating

wire was determined from Ohm's law:

$$\begin{aligned} \mathrm{I} &= \frac{\mathrm{U}}{\mathrm{R}} \\ &= \frac{20\ \mathrm{V}}{0.039\ \frac{\Omega}{\mathrm{m}} \cdot 9.5\ \mathrm{m}} \\ &= 54\ \mathrm{A}. \end{aligned} \tag{42}$$

According to Equation 42, a current of 54 A will be reached with a length of 9.5 m and 20 V voltage.

Figure 4.4.: Insulated Heating Wire.

5. Test Rig Construction

The test rig is constructed and utilised in the cryo-lab of the DLR in Bremen. This is obligatory due to safety procedures. LN handling during the experiment and the use of high-current electrical power necessitate stringent safety requirements. The hardware and assembly procedure shall now be outlined.

5.1. Pt100

The Pt100 sensors are integrated in the regolith, to provide data to construct a complete temperature distribution. The Pt100 temperature sensors in Figure 5.1 are each soldered to four cables and insulated to prevent direct contact between the two ends in the regolith. The result can be seen in Figure 5.2. The other end of the sensor cables are connected by a crimp contact (Figure 5.3) to the temperature feedthrough. The sensors are connected with the computer with the plug connector in Figure 5.4.

Figure 5.1.: Pt100.

Figure 5.2.: Pt100 Connected.

Figure 5.3.: Crimp Contact.

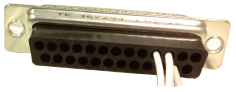

Figure 5.4.: Plug Connector.

The distribution of the Pt100 sensors can be seen in Figure 5.5. Sensor 1 is placed directly on the hot plate and sensor 3 is placed directly on the heat exchanger pipe while the other 3 sensors are placed within the regolith as shown in the figure.

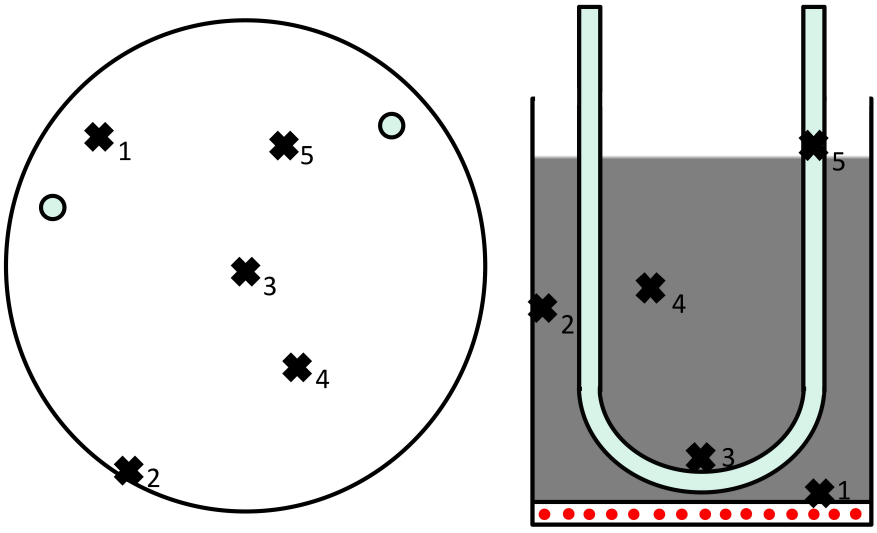

Figure 5.5.: Pt100 Horizontal (left) and Vertical (right) Distribution.

5.2. Heat Exchanger

The pipe heat exchanger is adapted to fit the confined space inside the vacuum chamber. A long, straight section for heat exchange is incorporated into the deep, "U"-shaped pipe with the inlet and outlet feeding through the vacuum chamber orifices. Before the outlet of the heat exchanger, there is a dogleg, necessitated by the restricted space in the vacuum chamber's cap which does not allow another position for the outlet. The heat exchanger pipe (before and after modification) can be seen in the Figures 5.6 and 5.7.

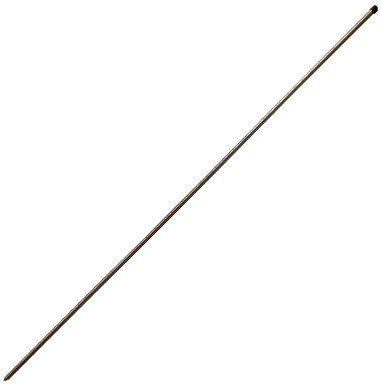

Figure 5.6.: Original Heat Exchanger.

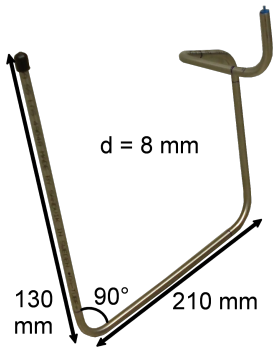

Figure 5.7.: Adapted Heat Exchanger.

The material is 316L stainless steel from Swagelok. Its thermal conductivity at 293.15 K is 15 W/(m · K) and its heat capacity at 293.15 K is 200 J/(kg · K) [43].

5.3. Nitrogen Tank

In Section 4.3.2 the height of a non-pressurised tank was calculated to achieve a certain flow velocity of the nitrogen. However a pressurised tank from the inventory of the cryo-lab of the DLR is used instead (see Figure 5.8).

Figure 5.8.: Nitrogen Pressure Tank.

The nitrogen tank is attached with a 18 mm diameter pipe. Because of the necessary reduction of the pipe diameter to connect the tank's 18 mm-pipe to the 8 mm diameter of the heat exchanger (HE) there is a loss in pressure. With the following assumptions and equations, this loss is estimated.

Assumptions:

$p_{\text{LN tank}}$	= const.	= 250 kPa	
T_{LN}	= const.	= 85.9 K	
ρ_{LN}	= const.	= 764.01 $\frac{\text{kg}}{\text{m}^3}$	
$\dot{m}$	= const.	= 2.2 $\frac{\text{g}}{\text{s}}$	
$d_{\text{LN tank}}$	= const.	= 16 mm	$\Rightarrow A_{\text{LN tank}} = 2.01 \times 10^{-4}\text{m}^2$
d_{HE}	= const.	= 6 mm	$\Rightarrow A_{\text{HE}} = 2.83 \times 10^{-5}\text{m}^2$.

The tank pressure is assumed to remain constant, with fluctuations having negligible effects on the flow. The temperature of the nitrogen, T_{LN}, is assumed to be constant at the nitrogen boiling point (as described in Section 4.3.2). The constant density and mass flow are derived from the assumption of a constant ullage pressure in the nitrogen tank:

$$\dot{m} = \rho_{\text{LN tank}} \cdot v_{\text{LN tank}} \cdot A_{\text{LN tank}}, \tag{43}$$

$$\begin{aligned} \Leftrightarrow v_{\text{LN tank}} &= \frac{\dot{m}}{\rho_{\text{LN tank}} \cdot A_{\text{LN tank}}} \\ &= 0.014\text{m} \cdot \text{s}^{-1}, \end{aligned} \tag{44}$$

$$\begin{aligned} \Delta p &= p_{\text{HE}} - p_{\text{LN tank}} \\ &= \frac{\rho_{\text{LN}}}{2} \cdot v_1^2 \cdot \left[1 - \left(\frac{A_{\text{LN tank}}}{A_{\text{HE}}}\right)^2\right] \\ &= -3.7 \text{ Pa}. \end{aligned} \tag{45}$$

The pressure loss is seen to be quite small compared to a tank ullage pressure of 250 kPa, and is therefore neglected.

5.4. Vacuum Chamber

5.4.1. Interior

An independent vessel is used to contain the regolith, which can be seen fully integrated in Figure 5.9. After filling it with the heat exchanger, the coiled heating wire and the regolith, the heat exchanger's depth is measured and adjusted (see Figure 5.10). Pt100 sensors are then integrated into the regolith. The complete vessel with regolith and heat exchanger is then inserted into the vacuum chamber. The heat exchanger is then connected to the nitrogen inlet and outlet.

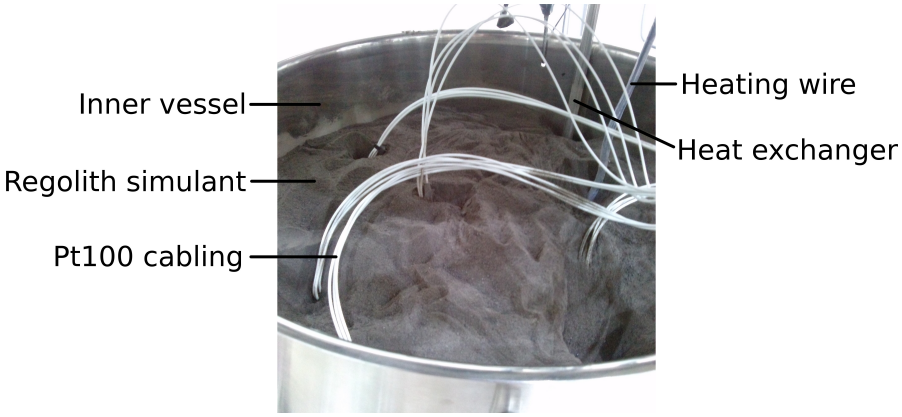

Figure 5.9.: Interior of the Vacuum Chamber, with Integrated Regolith, Heat Exchanger, Heater and Sensors.

Figure 5.10.: Prepared Regolith Container.

5.4.2. Exterior

The closed vacuum chamber with all connections is shown in Figure 5.11. The red sensor in Figure 5.11 is the pressure sensor and the thin white cables are the connections for the Pt100 sensors within the regolith simulant in the vacuum chamber.

Figure 5.11.: Vacuum Chamber.

5.5. Complete Test Rig

The complete experimental setup including vacuum chamber, nitrogen tank and all sensor components can be seen in Figure 5.12.

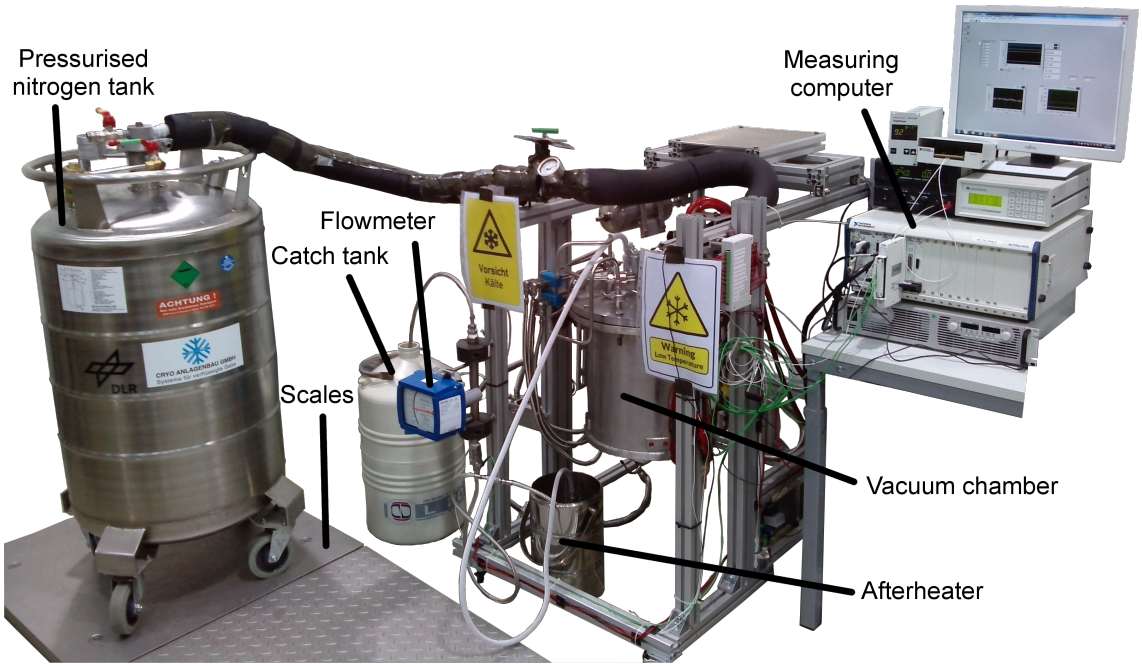

Figure 5.12.: Complete Test Rig in Use.

6. Heat Conductivity Measurements

In total, 22 experiments are executed, from basic testing of the test rig to the determination of the heat transfer (see Section A.2.15 to A.2.21). The test protocols and the measured sensor data can be found in Section A.2. An evaluation of the data and the determination of the heat transfer coefficient is performed in Chapter 7. In this chapter, the equipment testing and calibration, in addition to experimental observations, will be described.

6.1. Functionality Testing

6.1.1. Execution

Test 1 and 2 (see Section A.2.1 and A.2.2) are executed to confirm component functionality, in particular sensor operation and calibration. These tests are conducted at higher pressures (850 Pa and 1000 Pa for Test 1 and 2, respectively) and with the heating system non-operational. The required heat transfer test conditions are not achieved during these functionality tests.

The sensor behaviour after the initiation of the nitrogen flow is observed and monitored. The inflow valve setting is varied, which through changing pressure differential, influences the flow velocity, and the variable area flowmeter readout monitored.

6.1.2. Observations - Test 1

All temperature sensors are operational. The sensors within the nitrogen flow (T_{t1}, T_{t2}. T_{t3}) record the lowering of the pipe temperature with the initiation of the flow. Sensors in the regolith show a similar response. T_{t3}, the nitrogen flow temperature sensor directly proceeding the flowmeter, confirms that the nitrogen was heated in the heat exchanger, and, however, is not above the minimum temperature of 233.15 K (see Figure 6.1). Another observation made in Figure 6.1, sensor T_{t2} oscillates regularly from about 276 s until the nitrogen valve is closed. In Figure 6.2 it can be seen that the mass flow sensor begins oscillating after 250 s. T_3 is seen Figure 6.3 to drop the fastest in the regolith.

6.1.3. Justification and Conclusions - Test 1

When Figure 6.1 is compared with Figure 6.2, it can be seen that the values of the mass flowmeter start showing oscillating values at the point when T_{t3} shows a low nitrogen temperature. According to the manufacturer, the flowmeter is unable to function correctly in fluids below 233.15 K. To rectify this, an afterheater (see Figure 6.4) is installed to warm the nitrogen before entering the mass flowmeter. The afterheater consists of a vessel of water, in which a segment of the pipe is submerged.

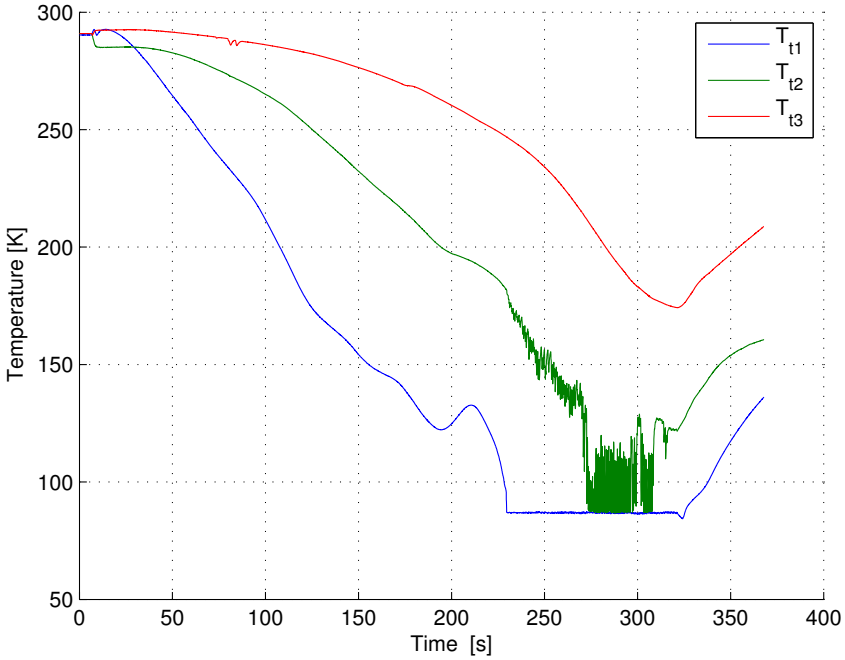

Figure 6.1.: Thermocouple Temperatures, Test 1.

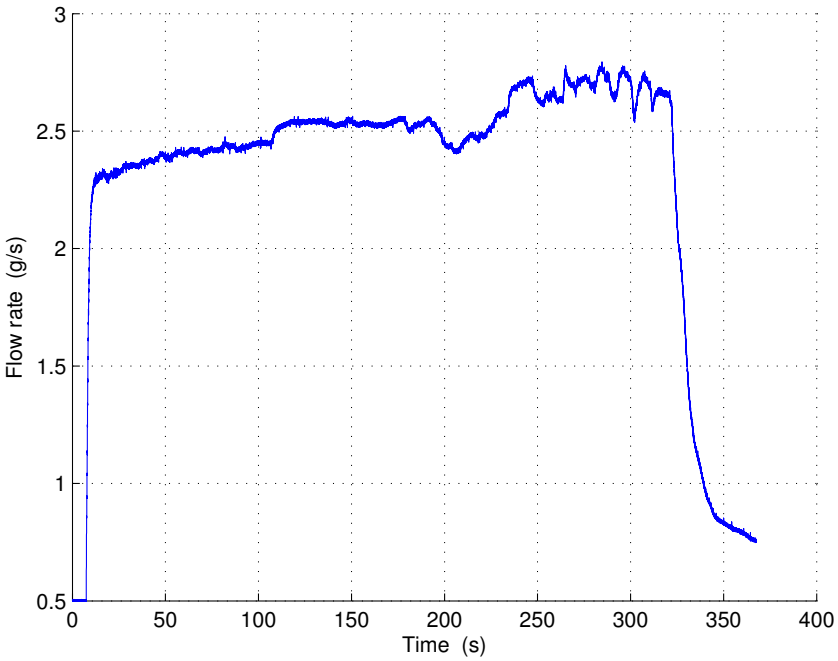

Figure 6.2.: Mass Flow Rate, Test 1.

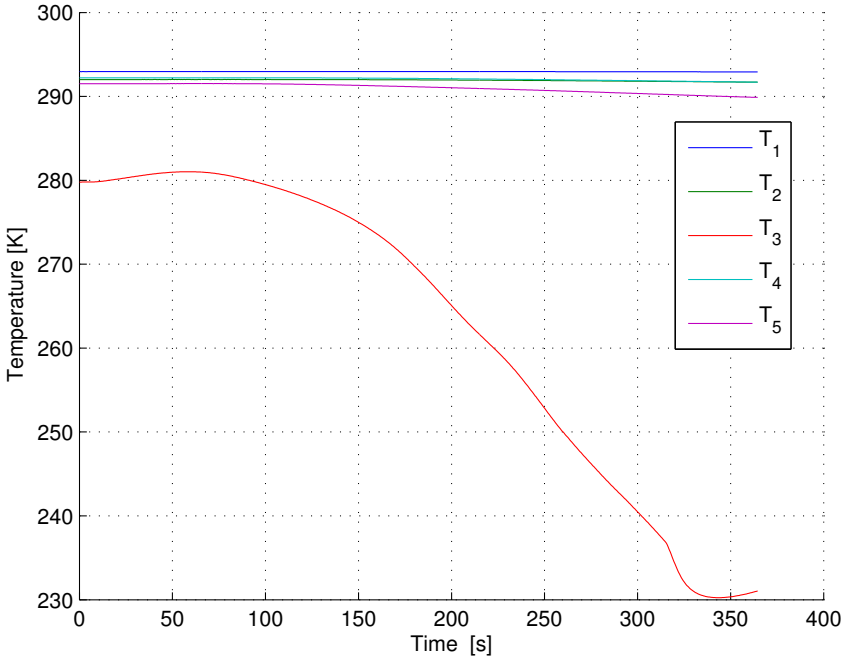

Figure 6.3.: Pt100 Temperatures, Test 1.

Figure 6.4.: Afterheater.

6.1.4. Observations - Test 2

Following the modification to include the afterheater (in Test 2, see Section A.2.2) the nitrogen entering the flowmeter stays on an almost-constant level above the allowed minimum (see Figure 6.5). The pressure in the vacuum chamber is observed to increase, unlike Test 1, where it continued to drop.

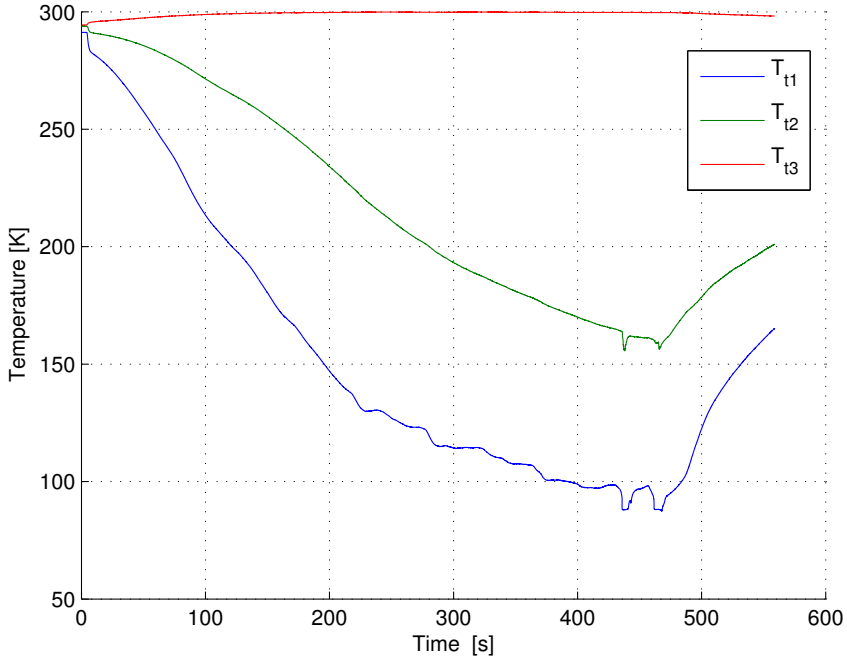

Figure 6.5.: Thermocouple Temperatures, Test 2.

6.1.5. Justification and Conclusions - Test 2

The mass flow values measured by the flowmeter have no discernable abnormalities anymore, due to a nitrogen temperature above the allowed minimum. Because of the higher pressure within the vacuum chamber compared to Test 1, it is assumed that this is due to a leakage in the chamber's setup and/or the degassing of the regolith simulant. Therefore a leakage test will be executed on the vacuum chamber.

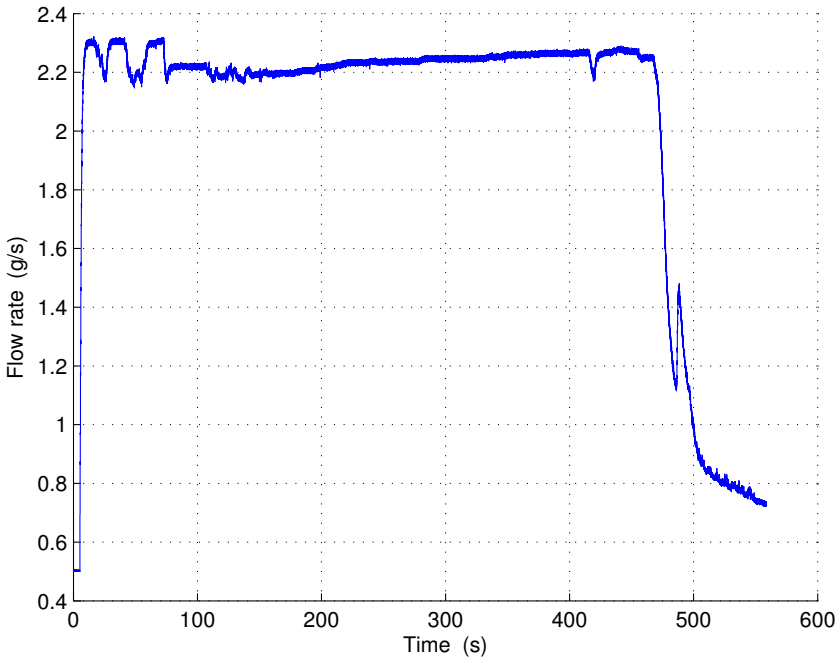

Figure 6.6.: Mass Flow Rate, Test 2.

6.2. Vacuum Leakage Tests

6.2.1. Execution

Contrary to the expected behaviour, the pressure within the vacuum chamber did not decrease below 1 kPa to the required value below 5 Pa. This indicates that a leak is present. Therefore, the empty vacuum chamber is examined with the leak detector seen in Figure 6.7. Because the leak detector uses a turbomolecular pump which is easily vulnerable to even the smallest hardware particles, the vacuum chamber needs to be cleaned and emptied out completely. To find leaks, the chamber is resealed, the leak detector is attached to the vacuum pump and creates a vacuum with its turbomolecular pump. After a certain vacuum quality is reached, all possible weak points on the chamber exterior are blown at with Helium from a pressurised gas cylinder. The pumped-out gas from the vacuum chamber is examined using a mass spectrometer which alerts as soon as the detected Helium exceeds a limit value. After closing all the leaks two leakage tests (see Section A.2.3 and A.2.4) are performed to proof the tightness of the vacuum chamber.

6.2.2. Observations - Test 3

During the evacuation process, the pressure decrease slows down with time and improving quality. After 2.5 hours, a pressure of 24 Pa is reached and the test is aborted.

Figure 6.7.: Leak Detector.

6.2.3. Justification and Conclusions - Test 3

The vacuum pump is attached to the vacuum chamber with a thin pipe which helps to control the air flow better, but hampers a fast evacuation of the chamber. For this reason the test is aborted after 2.5 hours and is repeated afterwards with a direct connection between vacuum pump and chamber.

6.2.4. Observations - Test 4

After 45 minutes a pressure of 9.5 Pa is reached and the test is aborted.

6.2.5. Justification and Conclusions - Test 4

Although the pressure was still decreasing, the test was aborted after a pressure of 9.5 Pa is reached. The achieved vacuum quality is sufficient for the planned experiments, therefore a further decrease in pressure for tightness testing is not necessary.

6.3. Heating Wire Functionality Tests

6.3.1. Execution

After the sensors were tested and the vacuum chamber was resealed, the heating system functionality is tested. In Test 5 and Test 6 (see Section A.2.5 and A.2.6) the heating wire is tested alone without any nitrogen flow. Different parameters are set up for the two tests. For safety reasons, the maximum allowed temperature of the heating wire is set to 473.15 K, which is reached at 40 A. Also for safety reasons, the first test of the heating wire is not performed with the maximum allowed current. In Test 5 a smaller value is chosen, 23.9 A. This value resulted in a voltage of 9.09 V. In Test 6, the maximum allowed

current of 40 A is set with a voltage of 14.99 V. In both cases the vacuum chamber has a pressure of 140 Pa at the beginning of the experiments.

6.3.2. Observations

In both tests, the temperature within the vacuum chamber rises (see Figures 6.8 and 6.9). At the beginning of the tests, T_4 has the steepest gradient because it is positioned the closest to the heating wires within the regolith. T_1 starts rising later but is hotter than every other sensor (with the exception of T_3) at the conclusion of the experiment. T_3 shows an irregular increase after 687 s, which needs to be examined.

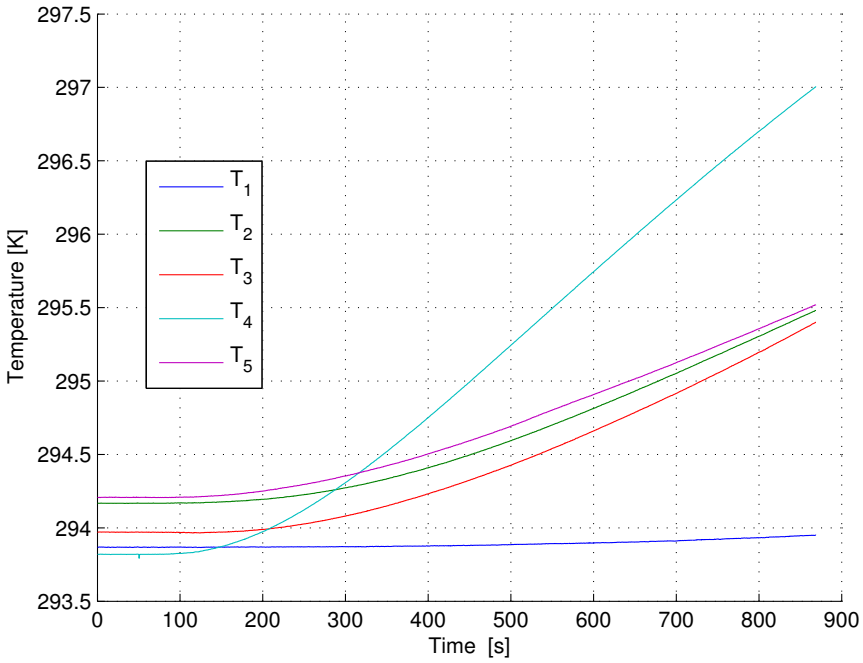

Figure 6.8.: Pt100 Temperatures, Test 5.

6.3.3. Justification and Conclusions

The slow increase of T_1 in Test 5 is accounted for by the position of the sensor. It is placed on the hot plate and not on the heating wire itself. In Figure A.7 this temperature sensor starts rising with an even greater gradient than the other sensors. An exception is the behaviour of T_3 in Test 6. Opening the vacuum chamber after Test 6 provides the explanation for this behaviour. An electrical short at the temperature feedthrough for this sensor is found and rectified.

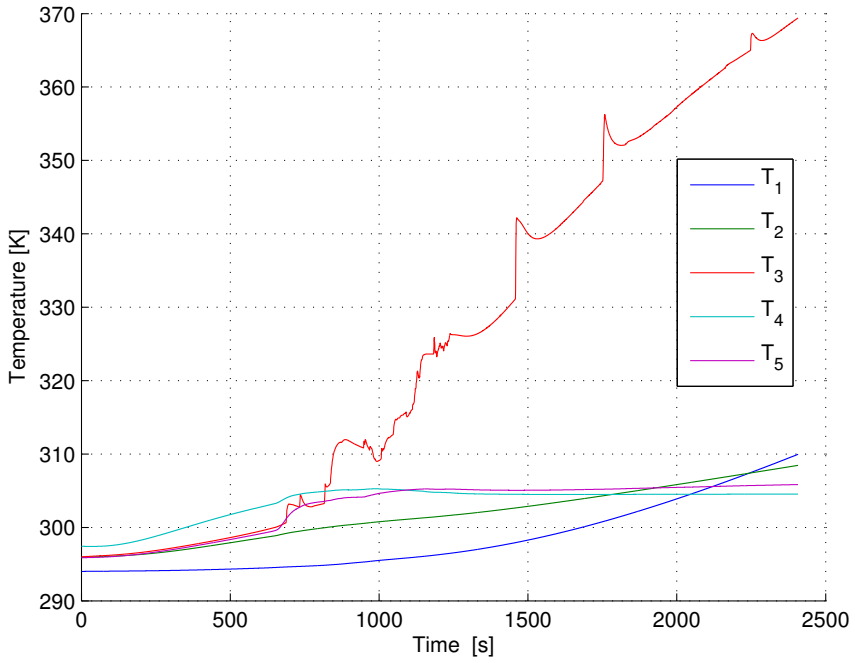

Figure 6.9.: Pt100 Temperatures, Test 6.

6.4. Calibration of Pt100 Sensors

6.4.1. Execution

In Test 7 and Test 8, the Pt100 sensors are calibrated to guarantee more precise results for the following heat conductivity measurements. Iced water is used to provide reference temperature of 273.15 K. The sensors are kept in the iced water for 30 s. Afterwards, an average value is determined from the measurements.

6.4.2. Justification and Conclusions

Due to some problems at Test 7, in keeping the reference fluid (water) at a constant temperature, the calibration had to be repeated in Test 8. The calibration of all sensors can be seen in Figures 6.10 to 6.14. The results are listed in Table 6.1.

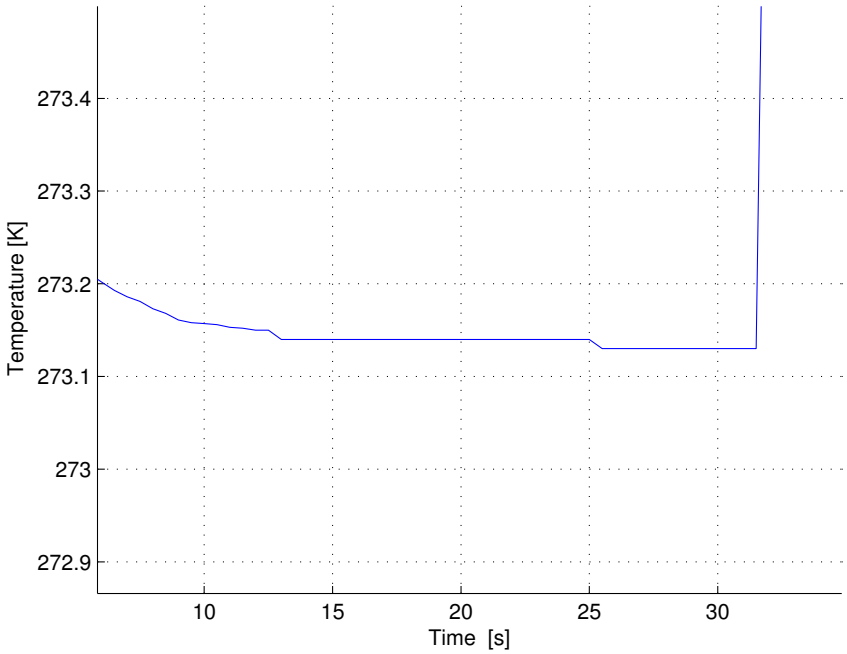

Figure 6.10.: T1 Calibration, Test 8.

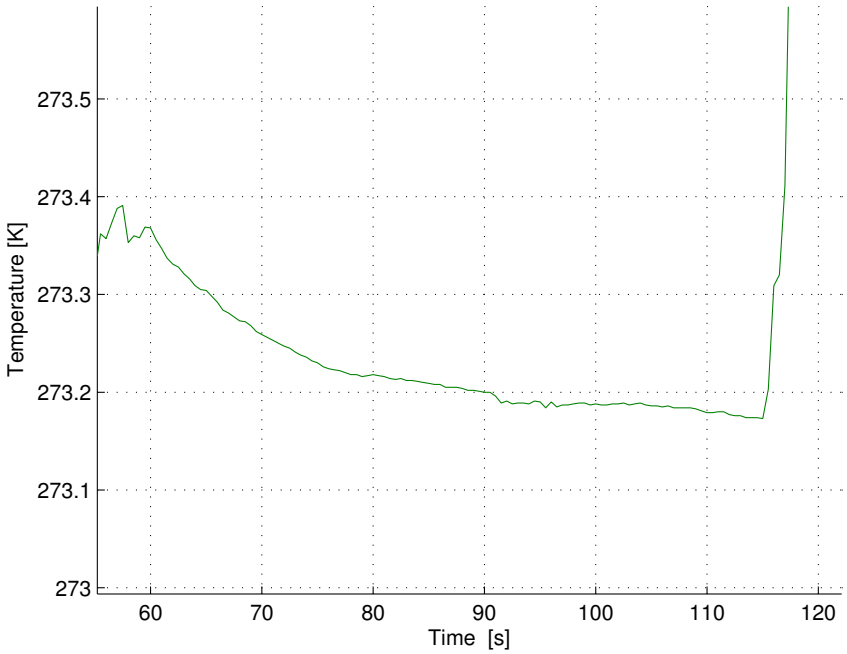

Figure 6.11.: T2 Calibration, Test 8.

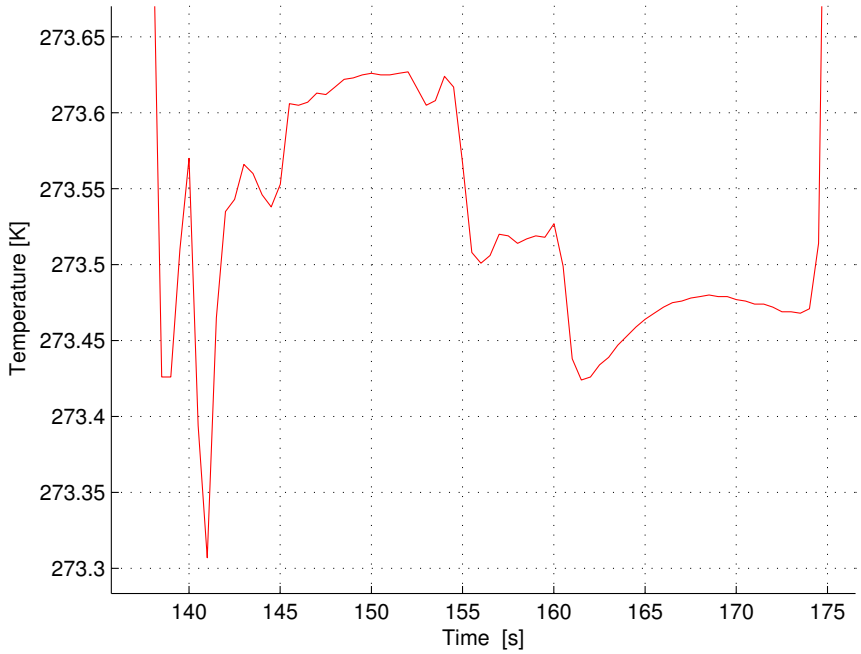

Figure 6.12.: T3 Calibration, Test 8.

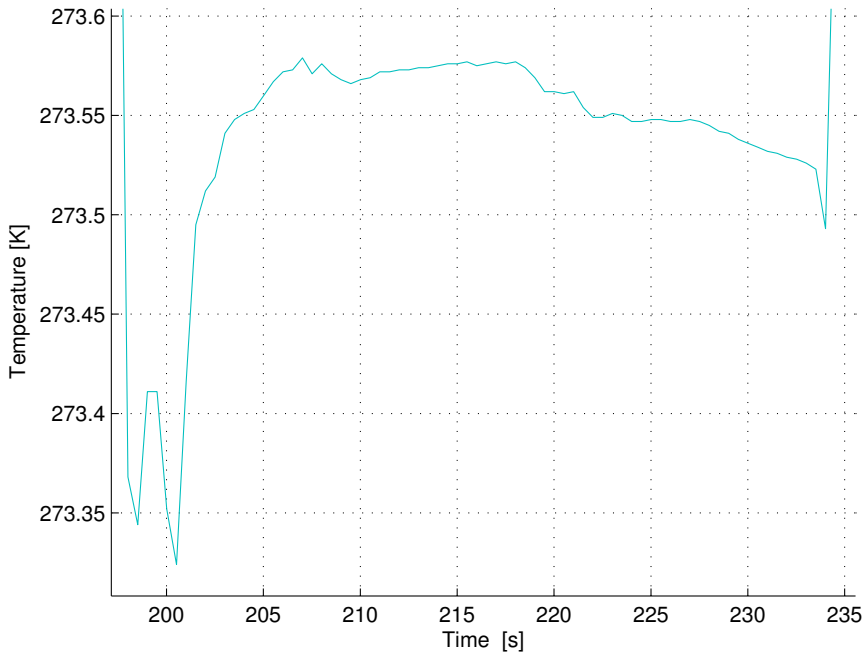

Figure 6.13.: T4 Calibration, Test 8.

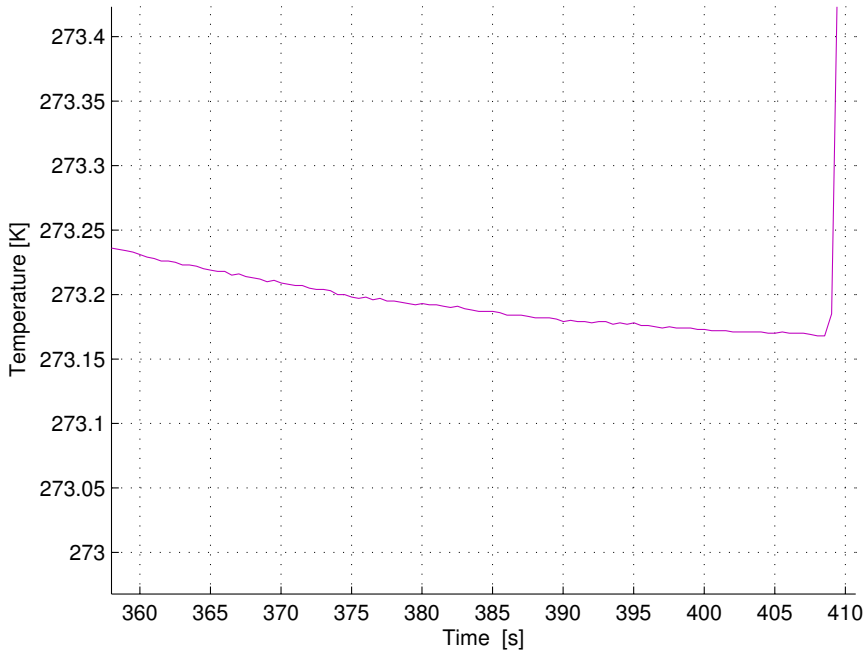

Figure 6.14.: T5 Calibration, Test 8.

Table 6.1.: Calibration of Pt100 sensors

Sensor	$T_{reference}$ [K]	$T_{recorded}$ [K]	Correction [K]
1	273.15	273.18	- 0.03
2	273.15	273.19	- 0.04
3	273.15	273.53	- 0.38
4	273.15	273.56	- 0.41
5	273.15	273.18	- 0.03

6.5. Preliminary Heat Conductivity Measurements

6.5.1. Execution - Test 9

Test 9 is the first heat conductivity measurement to test the functionality of the integrated test rig, including the heating wire. At the start the vacuum chamber has a pressure of 150 Pa and the heating wire is set to 3.68 V and 15 A. The nitrogen tank has a pressure of 250 kPa and its valve will be opened for 30 minutes.

6.5.2. Observations - Test 9

The heating wire is on from the beginning of the experiment and consequentially the regolith temperature is higher than room temperature. T_1 is observed to rise consistently during the experiment (see Figure 6.15). After a short start-up phase to cool all nitrogen pipes down, a constant temperature is reached at the heat exchanger entry (T_{t1}, see Figure 6.16). An unexpected behaviour can be seen at T_{t2}, the heat exchanger outlet. There are regular, oscillating step-changes in temperature of about 20 K. During the experiment, no mass flow rate is recorded. After trouble shooting, a loose contact is found to be the problem and solved during the experiment. For this reason, there are no values from the flowmeter at the beginning of the experiment (see Figure 6.17). Another abnormality is the behaviour of the pressure during the experiments, which shows fluctuations before reaching 250 Pa at the end of the experiment.

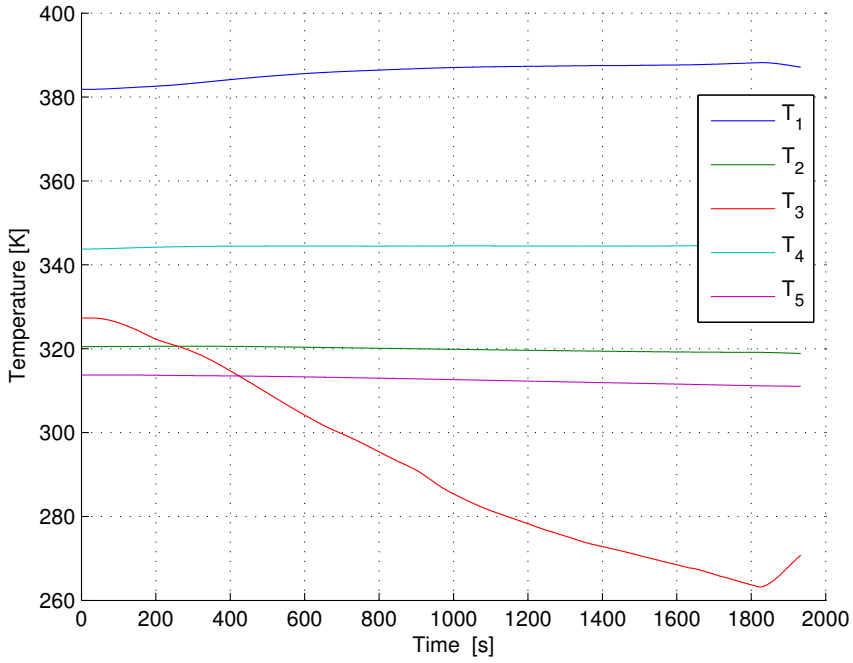

Figure 6.15.: Pt100 Temperatures, Test 9.

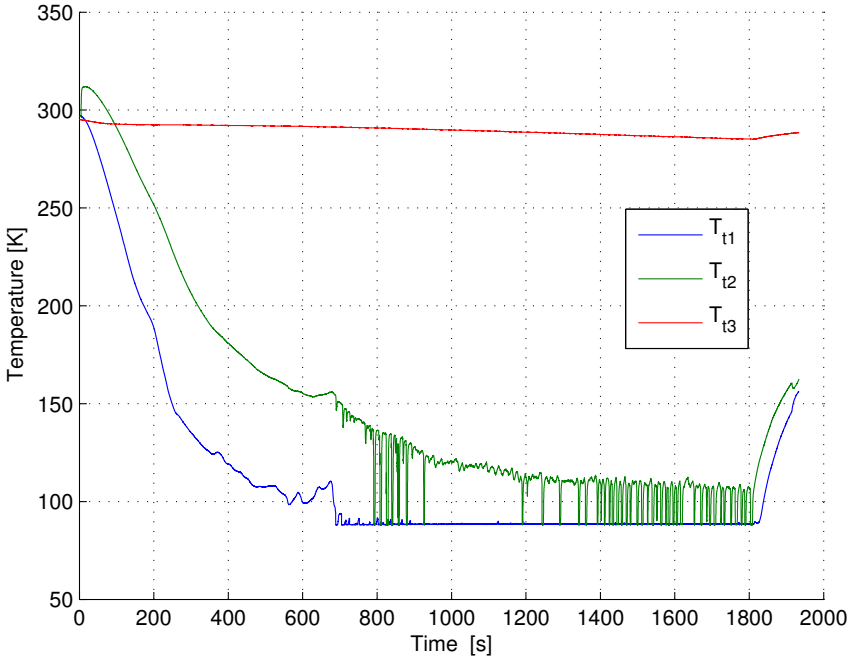

Figure 6.16.: Thermocouple Temperatures, Test 9.

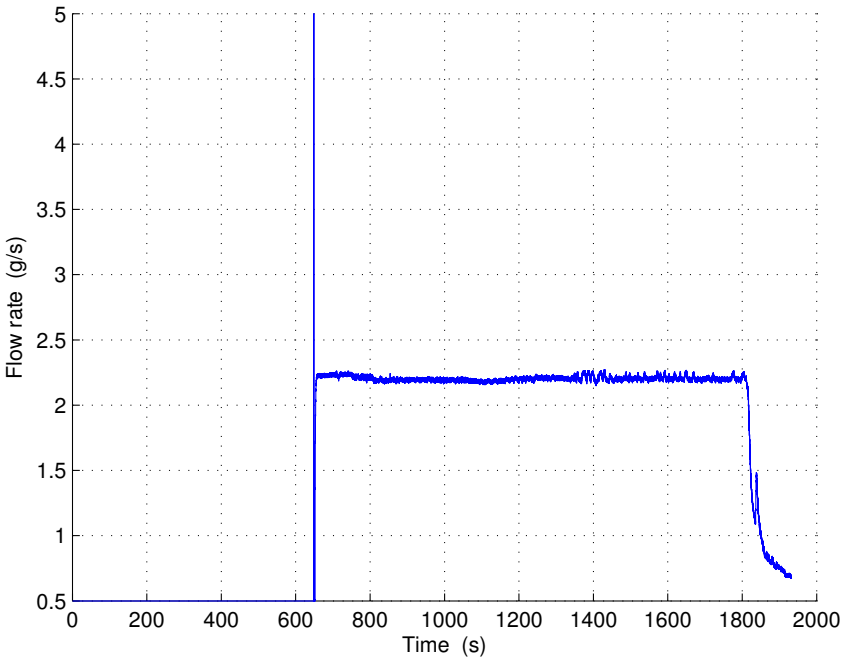

Figure 6.17.: Mass Flow Rate, Test 9.

6.5.3. Justification and Conclusions - Test 9

The regular step-changes in the nitrogen temperature at the heat exchanger outlet are due to an incomplete phase change. The nitrogen leaves the heat exchanger in two phases. This has significant implications to the evaluation of heat transfer. The two-phase flow instead of a complete phase change may occur due to poor heat transfer between the regolith and the heat exchanger. Insufficient heat is transferred to the nitrogen to the nitrogen to evaporate it completely. The poor heat transfer can be attributed to several things. Primarily, lunar regolith is a bad conductor of heat, exacerbated by the vacuum-filled voids [17]. This would imply that only very poor heat transfer is possible from the regolith to a heat exchanger. Secondly, it could be due to bad heat exchanger design; including the simple geometry and nitrogen mass flow rate. Both have a strong impact on the quality of heat exchange. Two-phase flow is addressed in detail, together with heat transfer coefficient evaluation, in Chapter 7.

6.5.4. Execution - Test 10

Test 10 is the second heat conductivity measurement with the goal to vary and control the mass flow rate. To achieve a control over the mass flow rate, the valve at the nitrogen tank is regulated manually. This experiment is executed without the heating wire and at a chamber pressure of 89 Pa.

6.5.5. Observations - Test 10

The temperature within the regolith drops at every sensor according to Figure 6.18. Within the nitrogen there are step changes in temperature (see Figure 6.19). The mass flow also exhibits strong fluctuations, with no continuous values (see Figure 6.20).

6.5.6. Justification and Conclusions - Test 10

The temperature in the regolith decreases because of the cooling effect of the nitrogen without the use of the heating wire. A constant mass flow rate can not be achieved through manual valve control. Consequentially, this test can not be used for the determination of the heat transfer coefficient. The outcome of this test was the assessment that better control over the mass flow rate should be possible. Therefore, the test rig should be modified for future experiments to include this feature.

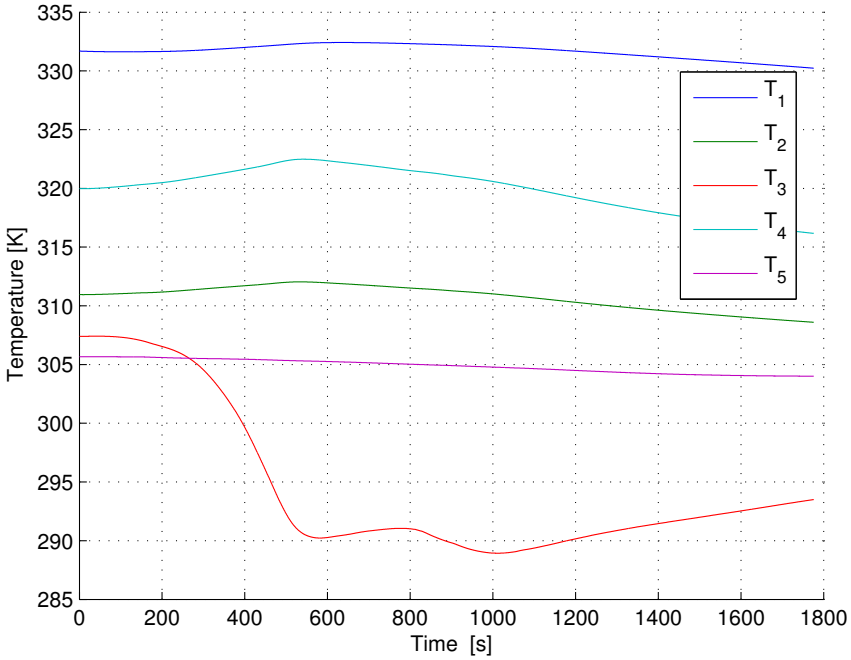

Figure 6.18.: Pt100 Temperatures, Test 10.

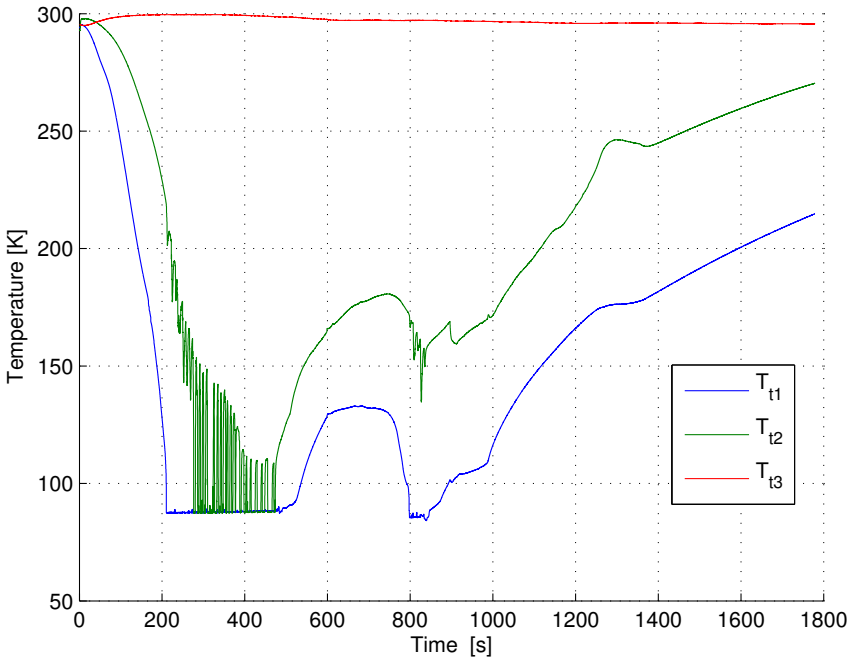

Figure 6.19.: Thermocouple Temperatures, Test 10.

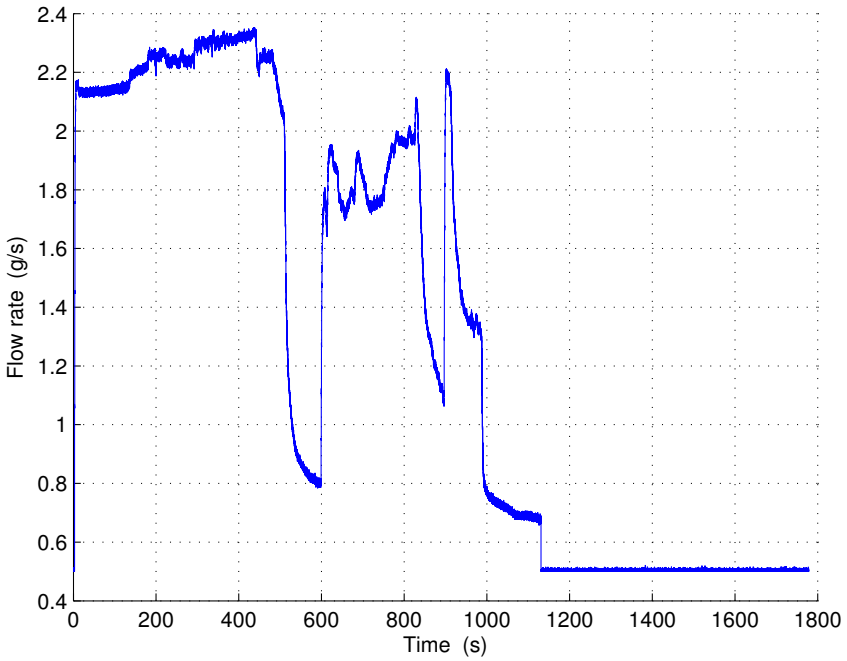

Figure 6.20.: Mass Flow Rate, Test 10.

6.6. Determination of the Resistance of the Electrical Connections

6.6.1. Execution

In Test 11 and Test 22 the resistance of the complete heating wire circuit, including the heating wire, current feedthrough and connection cables to the power supply, is determined. The resistance is determined at different temperatures of the heating wire using a multimeter probe. Test 11 is executed at a temperature of the hot panel of 365 K and Test 22 at ambient temperature of 294.25 K.

6.6.2. Results

The difference between both measurements amounts to just 0.02 Ω or 4.5 %, with 0.44 Ω in Test 11 and 0.42 Ω in Test 22.

6.7. Adaptations to the Test Rig

6.7.1. Execution - Test 12

As mentioned in Section 6.5, a few changes to the test rig setup are proposed in order to have a better control over the nitrogen mass flow rate. In Test 12, a new valve is installed

between the nitrogen tank and the heat exchanger inlet. The test is performed at 83 Pa chamber pressure and 250 kPa pressure in the nitrogen tank.

6.7.2. Observations - Test 12

In Figure 6.21 it can be seen that it is possible to set the mass flow rate to different values and keep them constant with the new valve. During the 40 minutes investigation to test the new valve operation, 2.64 kg of nitrogen is consumed.

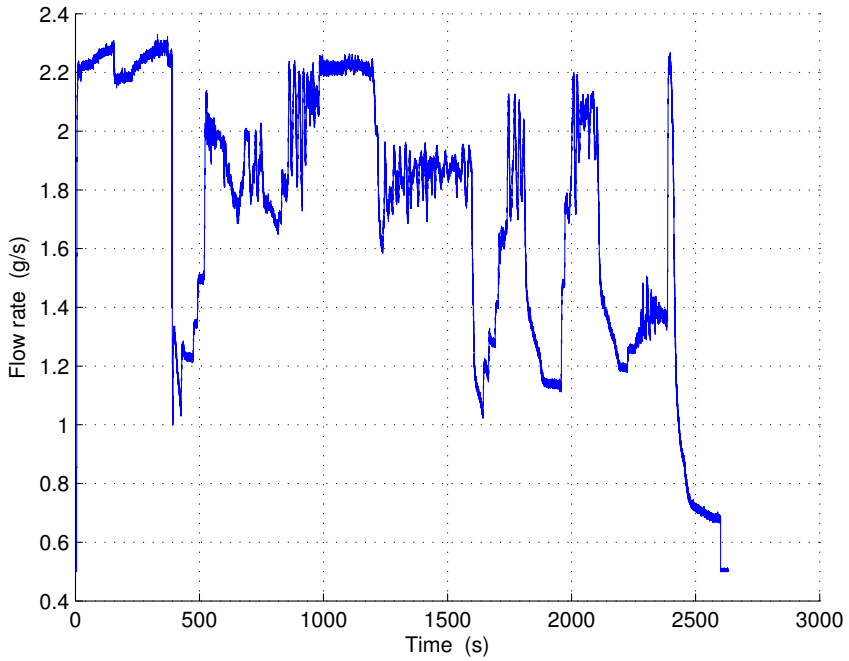

Figure 6.21.: Mass Flow Rate, Test 12.

6.7.3. Justification and Conclusions - Test 12

The valve enables good control over the mass flow rate. The only demerit is that it is not possible to reproduce the exact same mass flow rate again. Therefore, it is proposed to attach an angular reference scale to the valve-tap to be able to reproduce different mass flow rates, as shown in Figure 6.22.

6.7.4. Execution - Test 13

In Test 13 a scale is attached to the valve to be able to reproduce the same conditions in different experiments. The test is executed at 63 Pa chamber pressure and 250 kPa tank pressure.

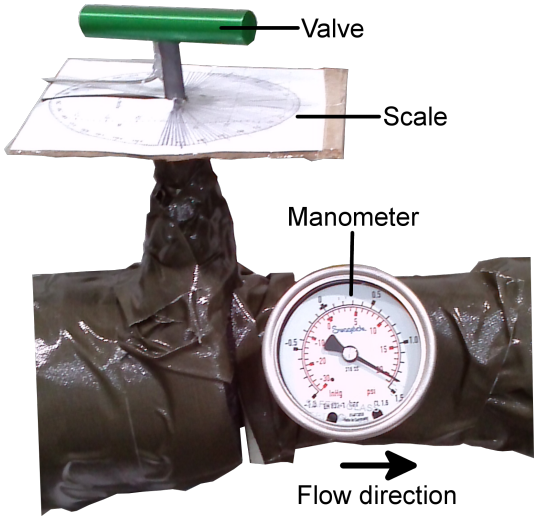

Figure 6.22.: Valve, Scale and Manometer.

6.7.5. Observations - Test 13

Abortion of the test.

6.7.6. Justification and Conclusions - Test 13

This test is aborted because the desired control of the mass flow rate is not possible. Another possibility to control the position of the valve shall be investigated. A manometer is installed to control the mass flow rate by measuring the pressure in the pipe.

6.7.7. Execution - Test 14

In Test 14 a manometer is attached directly following the valve. The valve can now be utilised to select a known pressure value, which can be read from the manometer (see Figure 6.22). In this manner, the mass flow rate can be controlled as it is a function of the pressure. In this experiment, a pressure of 0.2 MPa shall be produced and maintained after intentionally caused disturbances. The pressure in the chamber is 43 Pa and the pressure in the tank 250 kPa.

6.7.8. Observations - Test 14

It is possible to return to 0.2 MPa in the pipe several times after disturbances. This pressure resulted in a flow velocity of about 2.2 g/s as it can be seen Figure 6.23.

6.7.9. Justification and Conclusions - Test 14

After this successful testing, it is decided to do all following heat conductivity measurements with a pipe pressure of 0.2 MPa to ensure an equal mass flow rate of nitrogen.

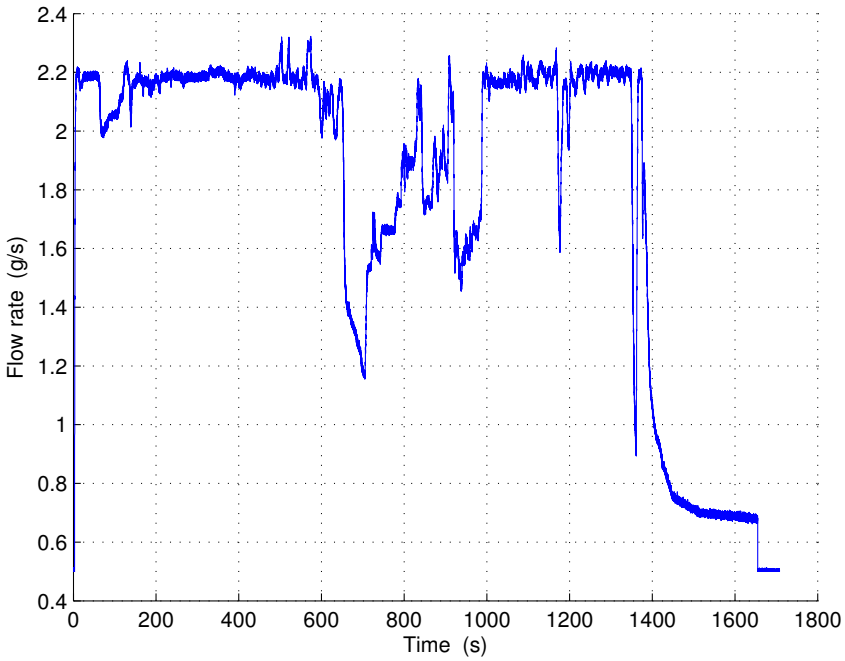

Figure 6.23.: Mass Flow Rate, Test 14.

6.8. Heat Conductivity Measurements

6.8.1. Execution

In all following heat conductivity measurements, the pressure in the pipe is set to 0.2 MPa. In Test 15 to Test 21, the heat conductivity measurements for which this test rig is constructed are executed. The regolith simulant is cooled by the nitrogen heat exchanger at a very slow rate. Therefore, the measurements are performed at the coolest achieved temperature; ambient temperature, which was significantly warmer than the required temperature of 250 K. The pressure in the chamber is not consistent for every experiment but varies between 36 Pa and 38 Pa, with the exception of Test 15 where the chamber pressure is at 42 Pa. The pressure in the nitrogen tank also varies, but the pressure in the pipe is kept constant at 0.2 MPa. After the start-up phase in which the nitrogen at the heat exchanger entry is not completely liquid, the measurement is performed for 5 minutes in Test 15 to Test 18 and for 10 minutes in Test 19 to Test 21.

6.8.2. Observations

During some of the measurements, a fluctuation in the chamber pressure is observed. The temperature in the regolith in Test 15 is higher than in all the other heat conductivity experiments. Due to the similarity of the experiments just one nominal test is graphically represented here (see Figures 6.24 to 6.26). All graphs (Pt100, thermocouple and flowmeter

measurements) for Test 15 to Test 21 can be seen in the Figures A.30 to A.50.

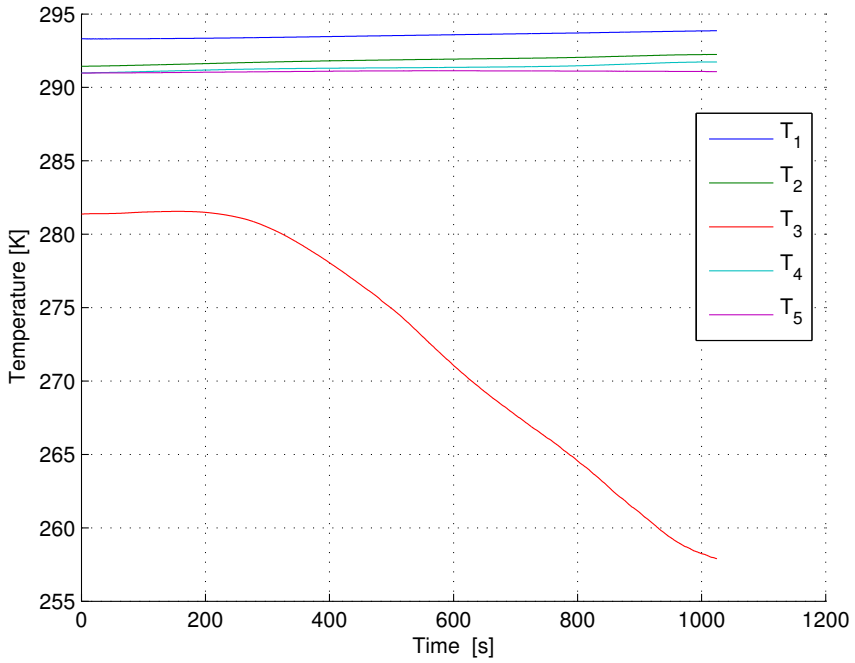

Figure 6.24.: Pt100 Temperatures, Test 21.

6.8.3. Justification and Conclusions

The pressure fluctuations in the vacuum can have different origins. One possibility is a leak within the heat exchanger which leads to nitrogen entering the vacuum chamber. An observation supporting this assumption is that the fluctuations just occur during the experiments while the nitrogen is flowing. However, a leak would be evident in a smaller measured mass flow rate in comparison to the experiments before the fluctuations occurred, which is not the case. The pressure fluctuations may also be attributed to the evolution of H_2O and CO_2 in the regolith simulant as described in Section 3.5. Given the vacuum conditions, the H_2O would become gaseous, and therefore increase the chamber pressure. This mechanism has a temperature dependency, and therefore may be aggravated by the operation of the heating-wire or the flow of the cold nitrogen.

Furthermore, due to start-up phenomena, only certain phases during each investigation contribute meaningful data for the heat transfer coefficient evaluation. Two-phase flow is observed in every case. This flow can have several regimes, as described in detail in Section 7.1.1.

The flow regime and liquid and gaseous fractions within the flow must be known for the heat transfer calculations. Each experiment demonstrates slug flow, evidenced by periodic oscillating temperatures between the liquid and gaseous temperatures. An example of

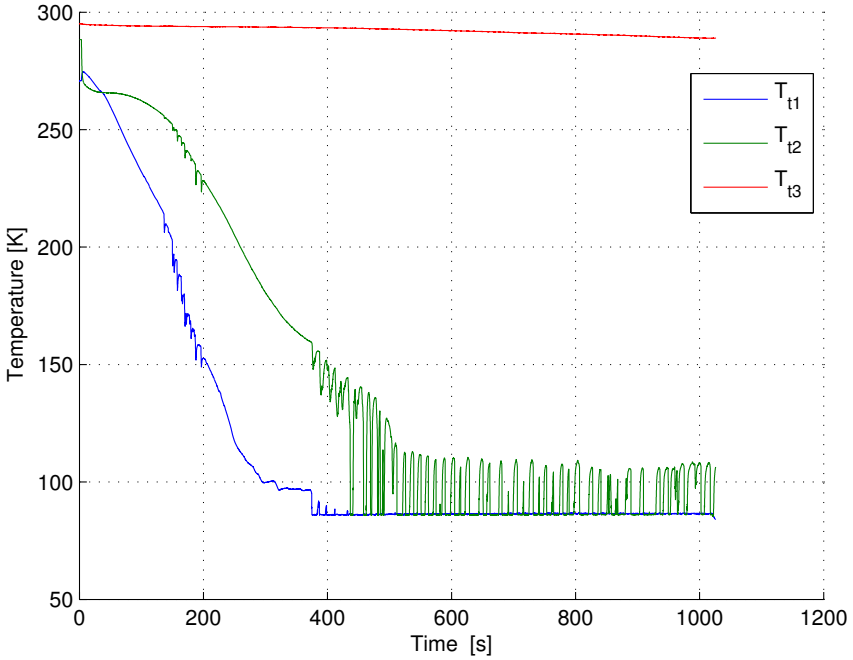

Figure 6.25.: Thermocouple Temperatures, Test 21.

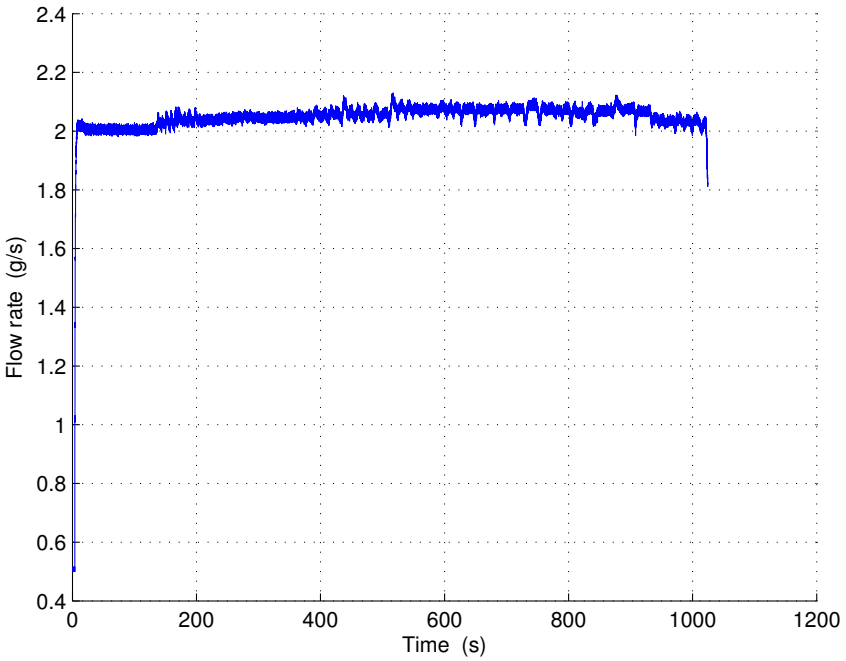

Figure 6.26.: Mass Flow Rate, Test 21.

this behaviour is exhibited in Figure 6.25, where the temperature sensor T_{t2} at the heat exchanger exit is seen to fluctuate in this manner from t = 500 s to t = 1020 s.

Slug flow can be readily analysed, therefore phases during the experiment exhibiting slug flow shall be used for the heat transfer coefficient evaluation.The evaluation of the experiments and the determination of the heat transfer coefficient is contained in Chapter 7.

7. Evaluation

7.1. Fundamentals

Due to the fact that the nitrogen does not change the phase completely, Equation 24 cannot be used in its current form. The partial phase change has to be taken into account:

$$\Delta h = c_{p,liquid} \cdot (T_{bI} - T_a) + x[h_v + c_{p,gaseous} \cdot (T_b - T_a)], \tag{46}$$

with x as the vapour quality at the heat exchanger outlet. This includes the gas in the Taylor bubble (see Section 7.1.2) as well as the gas within the liquid slug. Because the nitrogen enters the heat exchanger at boiling temperature, the liquid phase at the outlet of the heat exchanger has still the same temperature:

$$T_{bI} = T_a. \tag{47}$$

With this specification, Equation 46 can be abbreviated to:

$$\Delta h = x[h_v + c_{p,gaseous} \cdot (T_b - T_a)]. \tag{48}$$

To determine x a more detailed analysis of the nitrogen flow is needed.

7.1.1. Two-phase Flow Regimes

In two-phase flow, the phases may either be turbulent or laminar. The liquid and gas phases may have different states, therefore several combinations of two-phase flow regimes exist [4]. The various modes of two-phase flow in a horizontal pipe are illustrated in Figure 7.1 and in a vertical tube in Figure 7.2.

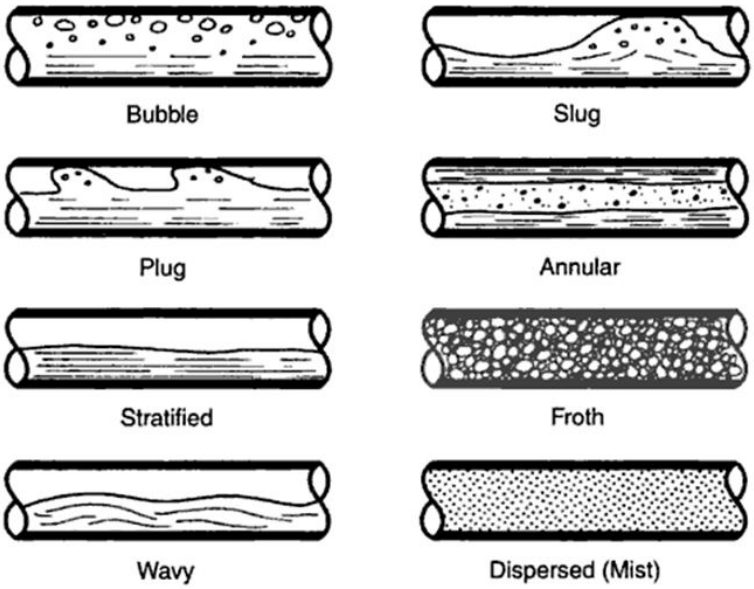

Figure 7.1.: Two-phase Flow Regimes in a Horizontal Pipe [21].

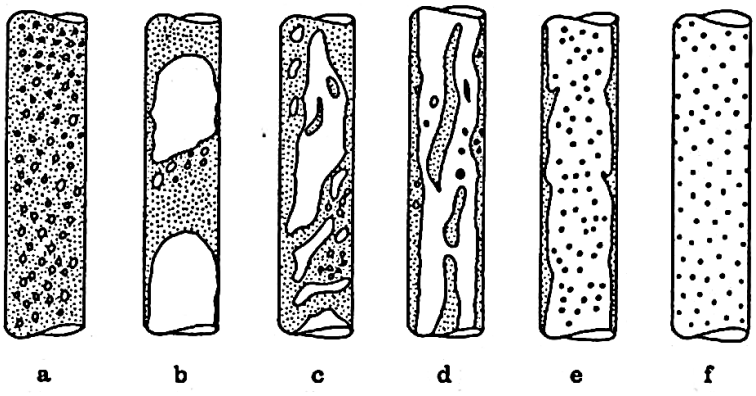

Figure 7.2.: Flow Types in a Vertical, Unheated Tube with Upward Flow. **a** Bubble Flow; **b** Plug/Slug Flow; **c** Churn Flow; **d** Wispy-Annular Flow; **e** Annular Flow; **f** Spray or Drop Flow [2].

All these flow patterns appear more or less distinctive in a series one after the other during the evaporation of a liquid in a vertical tube, as illustrated in Figure 7.3, with x as the vapour quality [2].

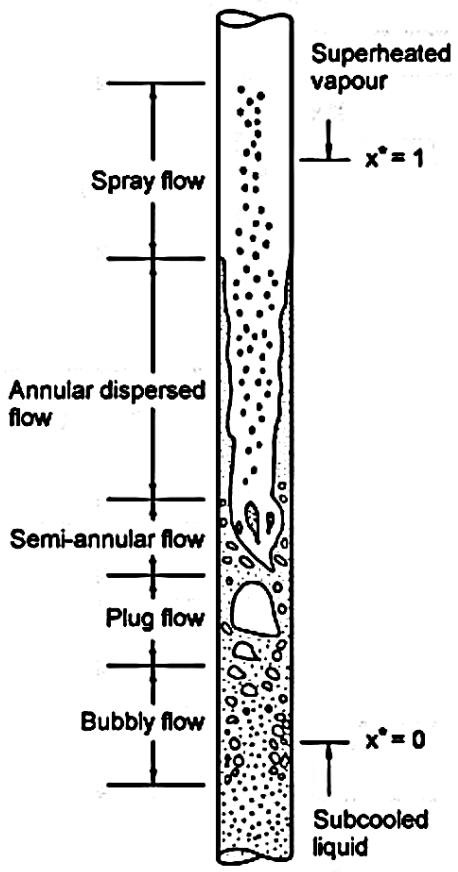

Figure 7.3.: Flow Patterns in a Vertical, Heated Tube (flow in upwards direction) [2].

7.1.2. Fundamental Equations

As seen in Section 7.1.1, there are six different flow patterns for vertical two-phase flow in tubes. These can all appear in series in heated tubes, like the one in the heat exchanger. As outlined in Chapter 6.8.3, because of the more-or-less regular phase change, it can be assumed that there is slug flow in the tube at the heat exchanger outlet. In vertical slug flow, the bubbles adopt a characteristic capsular shape with a rounded front and can either completely or nearly completely fill the channel cross-section, where, at most, a thin liquid film separates them from the channel wall. Such bubbles are called Taylor bubbles [37]. They move along separated by liquid slugs, within which may be a dispersion of smaller bubbles [62]. The slug unit in detail can be seen in Figure 7.4.

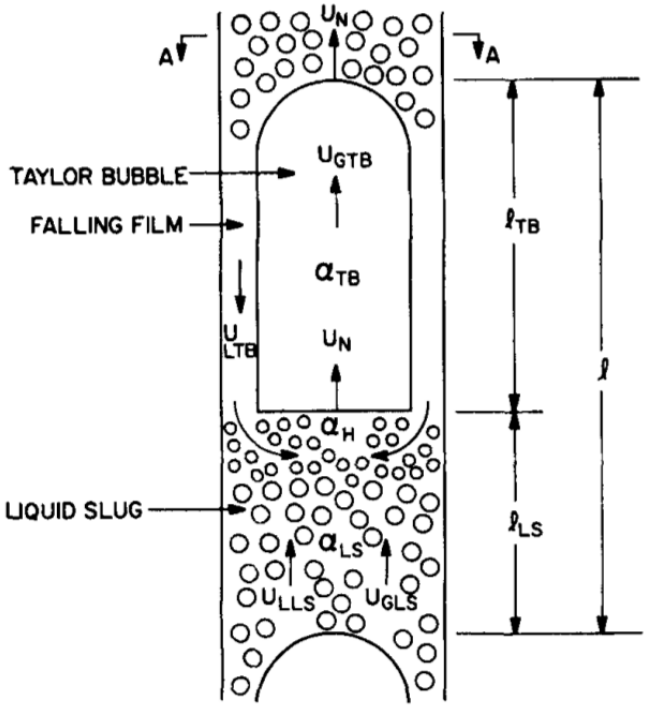

Figure 7.4.: Slug Unit [20].

To determine the average gas vapour quality, x, first the average volume void fraction over one slug unit, α_{SU}, is needed. It can be calculated by [20]:

$$\begin{aligned}\alpha_{SU} &= \frac{V_G}{V_{SU}} \\ &= \beta\alpha_{TB} + (1-\beta)\alpha_{LS},\end{aligned} \tag{49}$$

with V_G as the total volume of gas in the slug unit, V_{SU} as the volume of the slug unit itself and [20]:

$$\alpha_{TB} = \frac{A_{GTB}}{A}, \tag{50a}$$

$$\alpha_{LS} = \frac{A_{GLS}}{A}, \tag{50b}$$

$$\beta = \frac{l_{TB}}{l}, \tag{50c}$$

where A_{GTB} is the area of gas in the Taylor bubble, A the total cross-sectional area of the pipe, A_{GLS} the area of gas in the liquid slug, l_{TB} the length of the Taylor bubble and l the total length of the slug unit. To determine the average gas volume fraction of the slug unit, α_{SU}, α_{TB}, α_{LS} and β must be determined. [20]

According to [62] the Taylor bubbles have nearly the same diameter as the tube, so it is assumed that

$$A_{GTB} = A, \tag{51}$$

$$\begin{aligned} \Rightarrow \alpha_{TB} &= \frac{A_{GTB}}{A} \\ &= 1. \end{aligned} \tag{52}$$

The length of the Taylor bubble and of the whole slug unit can be determined as:

$$\begin{aligned} l_{TB} &= t \cdot x_{TB} \cdot v, \\ l &= t \cdot v, \end{aligned} \tag{53}$$

with t as the average time step between the phase change, x_{TB} the ratio of the Taylor bubble, and v as the flow velocity determined from the mass flow measurement:

$$\begin{aligned} v &= \frac{\dot{V}}{A_{HE}} \\ &= \frac{\dot{m}}{\rho_{SU} \cdot A_{HE}}, \end{aligned} \tag{54}$$

with ρ_{SU} as the average density of the whole slug unit:

$$\rho_{SU} = (x_{TB} + \alpha_{LS}) \cdot \rho_g + (x_L - \alpha_{LS}) \cdot \rho_L, \tag{55}$$

with

$$x_L = 1 - x_{TB}. \tag{56}$$

α_{LS} can be assumed to be 0.25, according to [60].

With all these values, the average vapour quality over one slug unit, x, can finally be determined:

$$x = \alpha_{SU} \frac{\rho_g}{\rho_{SU}}. \tag{57}$$

7.2. Determination of the Heat Transfer Coefficient

The properties of nitrogen at the heat exchanger outlet are first determined. Unfortunately, the nitrogen pressure at the heat exchanger outlet is unknown. The pressure loss, Δp_V, in the heat exchanger can be estimated with the following equation [61]:

$$\Delta p_V = \Delta p_{static} + \Delta p_{mom} + \Delta p_{frict}, \tag{58}$$

with Δp_{static} as the static pressure loss, Δp_{mom}, as the momentum pressure loss, and Δp_{frict} as the frictional pressure loss. The pressure loss calculation is demonstrated for a representative test (Test 21). The static pressure loss is 0 Pa because the inlet and outlet of the heat exchanger are at the same height level. The momentum pressure loss is [61]:

$$\begin{aligned} \Delta p_{mom} &= \dot{m}^2 \left\{ \left[\frac{(1-x)^2}{\rho_l (1-\alpha_{SU})} + \frac{x}{\rho_g \cdot \alpha_{SU}} \right]_{out} - \left[\frac{(1-x)^2}{\rho_l (1-\alpha_{SU})} + \frac{x}{\rho_g \cdot \alpha_{SU}} \right]_{in} \right\} \\ &= \left(0.0021 \ \frac{kg}{s} \right)^2 \left\{ \left[\frac{(1-0.46)^2}{6.17 \ \frac{kg}{m^3} (1-0.51)} + \frac{0.46}{4.8 \ \frac{kg}{m^3} \cdot 0.51} \right]_{out} - \left[\frac{(1-0)^2}{6.17 \ \frac{kg}{m^3} (1-0)} + 0 \right]_{in} \right\} \\ &= 0.54 \ \mu Pa. \end{aligned} \tag{59}$$

For the frictional pressure loss, the Reynolds-number and the two-phase pipe friction factor, f_{tp}, is needed [61]:

$$\begin{aligned}\mathbf{Re} &= \frac{v \cdot \rho_{SU} \cdot d}{\eta} \\ &= \frac{4 \cdot \dot{m}}{\pi \cdot d \cdot \eta} \\ &= \frac{4 \cdot 0.0021 \ \frac{kg}{s}}{3.14 \cdot 0.006 \ m \cdot 162.645 \times 10^{-6} \ Pa \cdot s} \\ &= 2741.31,\end{aligned} \tag{60}$$

and

$$\begin{aligned}f_{tp} &= 0.25\left[\log\left(\frac{150.39}{\mathbf{Re}^{0.98865}} - \frac{152.66}{\mathbf{Re}}\right)\right]^{-2} \\ &= 0.045.\end{aligned} \tag{61}$$

The frictional pressure loss is [67]:

$$\begin{aligned}\Delta p_{frict} &= \frac{\dot{m}^2 \cdot f_{tp} \cdot l}{A^2 \cdot 2 \cdot d \cdot \rho_{SU}} \\ &= \frac{(0.0021 \ \frac{kg}{s})^2 \cdot 0.045 \cdot 1 \ m}{(2.83 \times 10^{-5} \ m^2)^2 \cdot 2 \cdot 0,006 \ m \cdot 5.47 \ \frac{kg}{m^3}} \\ &= 3774.94 \ Pa.\end{aligned} \tag{62}$$

Substituting these values in Equation 58 gives a total pressure loss of 3774.94 Pa. Therefore, at the exit of the heat exchanger, a pressure of 0.196 MPa is obtained. The pressure at the outlet of the heat exchanger is therefore assumed to lie between 0.15 MPa and 0.2 MPa. The heat transfer coefficient will be determined for pressures 0.15 MPa and 0.2 MPa, to account for uncertainties in the pressure loss calculation. Using the equations presented in Section 7.1, the results in Table 7.1 are gained. The densities listed in Table 7.1 are taken from [28] at an assumed pressure of 0.2 MPa with linear interpolation:

$$\rho = \frac{\rho_2 - \rho_1}{T_2 - T_1} \cdot (T - T_1) + \rho_1, \tag{63}$$

where index 2 indicates the closest higher value and 1 the closest lower value given in reference [28]. One sample calculation to determine the density at 88.3 K for Test 9:

$$\begin{aligned}\rho_{T=88.3K} &= \frac{\rho_{T=90K} - \rho_{T=88K}}{90 \ K - 88 \ K} \cdot (88.3 \ K - 88 \ K) + \rho_{T=88K} \\ &= \frac{5.851 \ \frac{kg}{m^3} - 6.0 \ \frac{kg}{m^3}}{2 \ K} \cdot 0.3 \ K + 6.0 \ \frac{kg}{m^3} \\ &= 5.98 \ \frac{kg}{m^3}.\end{aligned} \tag{64}$$

The same calculation was also performed at 0.15 MPa and resulted in the same values, to three significant figures (see the final column in Table 7.1). The estimated value of 0.15 MPa is very conservative, assuming significant pressure loss, while the optimistic value of 0.2 MPa (the pressure at the manometer) assumes no losses.

The column "t" in Table 7.1 states the time period for the determination of x, where the flow regime was stable. Because of cool-down processes at the start of the experiment, not the whole record could be taken into account for the evaluation and determination of the average vapour quality.

Table 7.1.: Results

Test	t [s]	T_l [K]	$\rho_l \left[\frac{kg}{m^3}\right]$	T_g [K]	$\rho_g \left[\frac{kg}{m^3}\right]$	x_{TB}	$\dot{m} \left[\frac{g}{s}\right]$	α_{SU}	x
9	1344 - 1803	88.30	5.98	110.52	4.68	0.68	2.2	0.76	**0.74**
15	650 - 799	87.40	6.05	112.90	4.57	0.53	2.2	0.65	**0.61**
16	620 - 827	86.50	6.12	108.20	4.78	0.36	2.2	0.52	**0.47**
17	440 - 620	86.17	6.15	107.35	4.82	0.27	2.2	0.45	**0.40**
18	475 - 645	85.97	6.17	107.71	4.81	0.28	2.1	0.46	**0.40**
19	666 - 1006	86.35	6.13	108.51	4.77	0.38	2.1	0.54	**0.49**
20	503 - 971	86.14	6.15	107.74	4.81	0.30	2.1	0.47	**0.42**
21	523 - 1022	85.94	6.17	107.75	4.80	0.35	2.1	0.51	**0.46**

All the values for x in Table 7.1 are consistent, with the exception of Tests 9 and 15. Test 9 was conducted at a higher temperature, as the heating system was operative. All other tests were conducted without heating (see Table 7.3). Test 15 appears to be a singularity. The higher vapour quality in Test 15 (x = 0.61) is likely to be a result of the higher ambient temperature within the vacuum chamber, as described in 6.8.2.

Table 7.2.: Heat Capacity of Gaseous Nitrogen

Test	$c_{p0.15\ MPa} \left[\frac{J}{kg \cdot K}\right]$]	$c_{p0.2\ MPa} \left[\frac{J}{kg \cdot K}\right]$	$\Delta h_{0.15\ MPa} \left[\frac{kJ}{kg}\right]$	$\Delta h_{0.2\ MPa} \left[\frac{kJ}{kg}\right]$
9	1071.26	1083.11	164.8	165,00
15	1069.40	1080.46	137.96	138.14
16	1073.23	1086.01	104.43	104.56
17	1073.99	1087.19	88.66	88.77
18	1073.67	1086.68	88.90	89.0
19	1072.96	1085.63	109.11	109.25
20	1073.64	1086.63	93.28	93.40
21	1073.63	1086.62	102.27	102.40

In Table 7.2, the values for c_p are linear interpolated (see Equation 63) from [28] and substituted into Equation 48 to determine Δh.

Using Equation 2, adapted for a single fluid heat exchanger, and Equation 23, the heat

transfer coefficient can be determined:

$$k \cdot A \cdot \Delta T = \dot{m} \cdot \Delta h, \tag{65a}$$

$$\Leftrightarrow k = \frac{\dot{m} \cdot \Delta h}{A \cdot (\bar{T}_{regolith} - T_a)}, \tag{65b}$$

with $\bar{T}_{regolith}$, the average regolith temperature determined from T_2, T_4 and T_5. These temperatures are corrected with the calibration values from Section 6.4. T_1 and T_3 were not used, as these sensors were in direct contact to the heat exchanger pipe or the hot plate. A is the heat exchanger's exterior surface through which the heat is transferred. In the used geometry, this area is 12,328.61 mm^2.

The calculated heat transfer coefficients are presented in Table 7.3, for both assumed outlet pressures (0.15 MPa and 0.2 MPa). The effect of the assumed pressure loss on the final heat transfer coefficient is a difference of < 1 % for all cases. This is a relatively small difference, therefore the impact of assuming the heat exchanger outlet pressure, rather than obtaining the exact value through experimental measurement, is not significant. While not ideal, this assumption is not critical to the heat transfer coefficient evaluation.

Table 7.3.: Heat Transfer Coefficient

Test	$\bar{\mathbf{T}}_{\mathbf{regolith}}$ **[K]**	$\mathbf{k_{0.15\ MPa}}$ $\left[\frac{\mathbf{W}}{\mathbf{m^2 \cdot K}}\right]$	$\mathbf{k_{0.2\ MPa}}$ $\left[\frac{\mathbf{W}}{\mathbf{m^2 \cdot K}}\right]$
9	325.31	124.08	124.23
15	301.52	114.98	115.12
16	295.62	89.11	89.22
17	294.13	76.08	76.17
18	293.13	73.09	73.19
19	293.85	89.57	89.68
20	292.72	76.91	77.01
21	291.71	84.65	84.76

The differences in the values row-wise can be explained by the temperature-dependency of the heat transfer coefficient. The heat transfer coefficient is not directly dependent on the temperature, but it depends on the material's thermal conductivity which itself is temperature-dependent.

In Figure 7.5 the heat transfer coefficients are plotted against the regolith temperature. Errorbars in this plot represent the uncertainty in the heat exchanger outlet pressure (0.15 MPa and 0.2 MPa taken as the lower and upper values), and the assumed values for α_{LS} and A_{TB}.

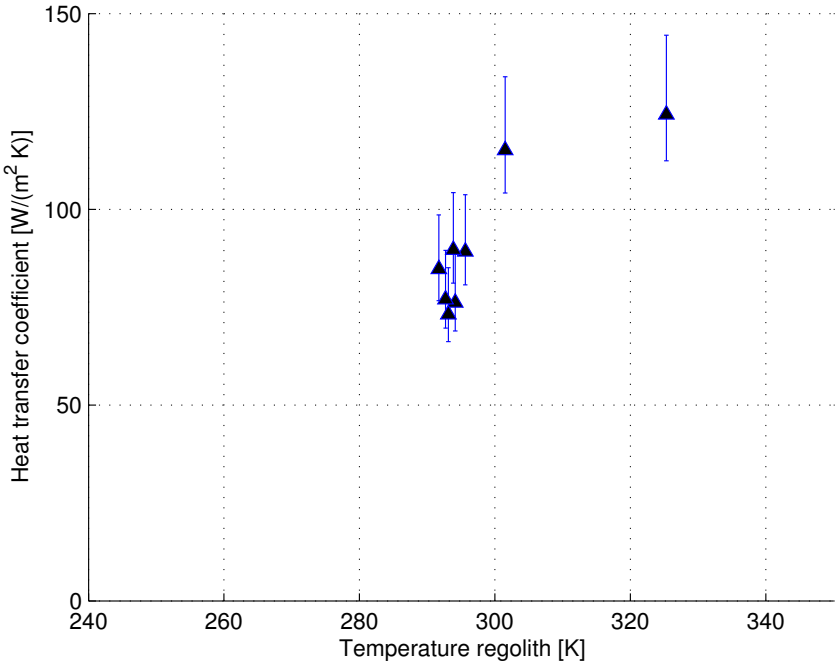

Figure 7.5.: k against $\bar{T}_{\text{regolith}}$, with errors.

7.3. Results Analysis

7.3.1. Experimental Consistency

The value obtained from Test 15 (at a temperature of 301 K and heat transfer coefficient of 115 W/(m^2·K) can be seen to be an outlier, and the value for the elevated temperature obtained in Test 9 is also observed to be significantly higher. Discarding the result from Test 15, the values for k show high consistency. In future investigations, the temperature dependency of k should be investigated. To prove the consistency of the results, the average and the standard deviation is determined. This is done for the tests 16 to 21.

To determine the standard deviation, S, and the average deviation, e, the arithmetic average, $\bar{x}$, is needed:

$$\begin{aligned}\bar{x} &= \sum_{i=16}^{21} \frac{k_i}{6} \\ &= \frac{(89.22 + 76.17 + 73.19 + 89.68 + 77.01 + 84.76)\frac{W}{m^2 \cdot K}}{6} \\ &= 81.67 \frac{W}{m^2 \cdot K}.\end{aligned} \tag{66}$$

The standard deviation is calculated by:

$$\begin{aligned} \mathrm{S} &= \sqrt{\sum_{\mathrm{i}=16}^{21} \frac{(\mathrm{k_i} - \bar{\mathrm{x}})^2}{6}} \\ &= 6.51 \frac{\mathrm{W}}{\mathrm{m}^2 \cdot \mathrm{K}}. \end{aligned} \tag{67}$$

The average deviation is calculated by:

$$\begin{aligned} \mathrm{e} &= \sum_{\mathrm{i}=16}^{21} \frac{|\mathrm{k_i} - \bar{\mathrm{x}}|}{6} \\ &= 6.22 \frac{\mathrm{W}}{\mathrm{m}^2 \cdot \mathrm{K}}. \end{aligned} \tag{68}$$

7.3.2. Heat Transfer Coefficient Temperature Dependency

To determine the heat transfer coefficient at 250 K, the results calculated in Chapter 7.2 are linearly extrapolated to 250 K. The singularity in Test 15 is neglected for this calculation, in order to not influence the final result. Values of 23.0965 and 23.1367 $\frac{\mathrm{W}}{\mathrm{m}^2 \cdot \mathrm{K}}$ for k are determined at 0.15 MPa and 0.2 MPa, respectively. The extrapolation can be seen in Figure 7.6 and 7.7, with the calculated standard deviations.

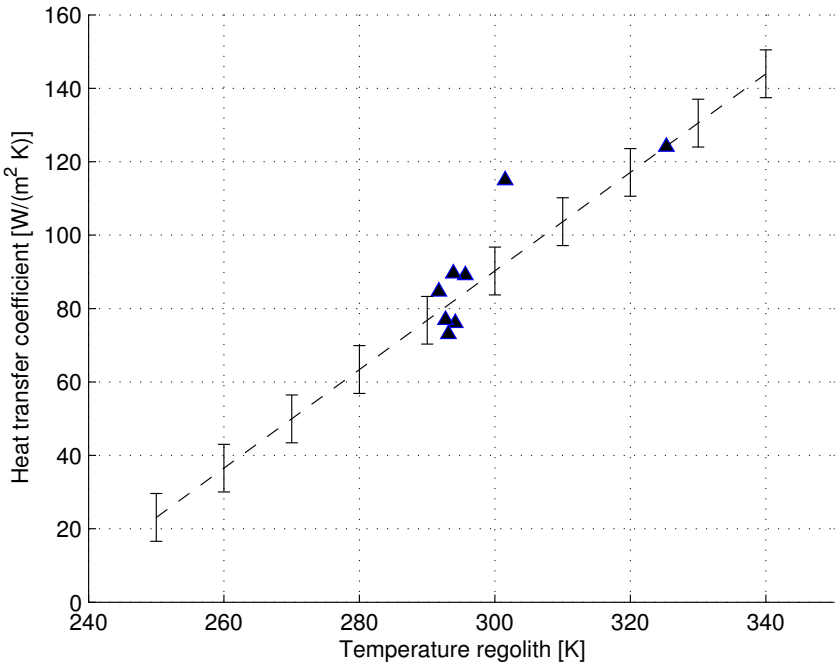

Figure 7.6.: Linear extrapolation of $\mathrm{k}_{0.15\ \mathrm{MPa}}$ against $\bar{\mathrm{T}}_{\mathrm{regolith}}$, including standard deviation.

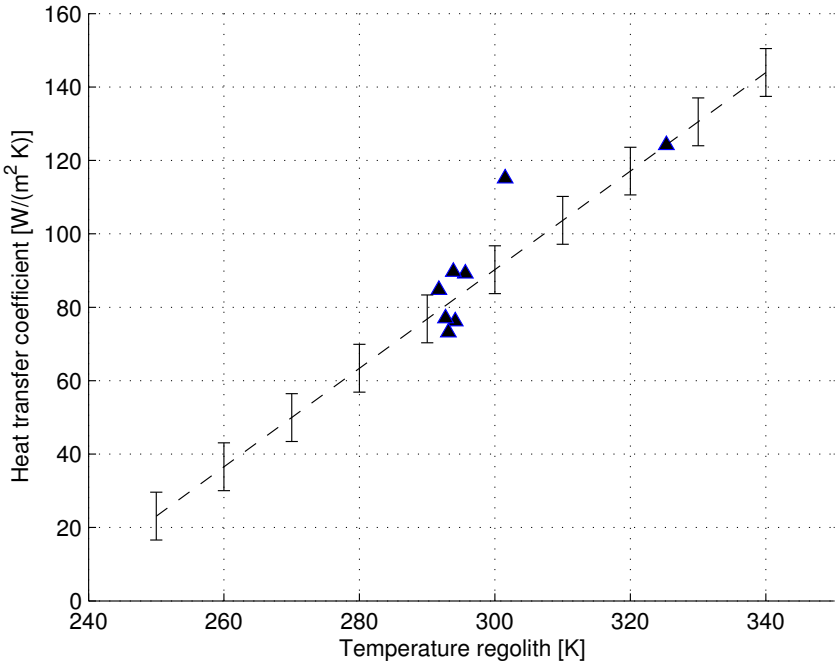

Figure 7.7.: Linear extrapolation of $k_{0.2\ \mathrm{MPa}}$ against $\bar{T}_{\mathrm{regolith}}$, with standard deviation.

Because the value for k at 250 K is extrapolated from just 6 other results it has to be treated with caution. Extrapolating outside of the measured range is not anticipated to provide an accurate result, particularly since the linear relationship to the regolith temperature cannot be confirmed with such little data. Literature was consulted to determine a function for the heat transfer coefficient of heat exchangers with temperature. k was found to be very sensitive with varying logarithmic mean temperature differences. An example of this relationship is shown in Figure 7.8 for coiled, evaporative nitrogen heat exchanger. In this figure k is denoted by α with the units kcal/(m^2·h·deg). k is seen to follow a Gauss curve-like function, with peaks between 10 to 25 K, depending on the heat exchanger used. The experimental data cannot be fitted to this function, due to complexity. Therefore, it is recommended for future investigations, that a wider regolith temperature range is investigated, encompassing the target value of 250 K. More data points should also be obtained.

7.3.3. Experimental Validity

Heat transfer coefficients from similar experiments are compared to the values found in this thesis for k. In Reference [42] a geothermal experiment in northern Tunisia, using water as heat exchanger fluid, delivered values for k of 29.1 - 58.9 W/(m^2·K). These values were mostly dependant on the varying mass flow. According to [54] water-to-water heat exchangers reach heat transfer coefficients from 850 - 1700 W/(m^2·K). The heat

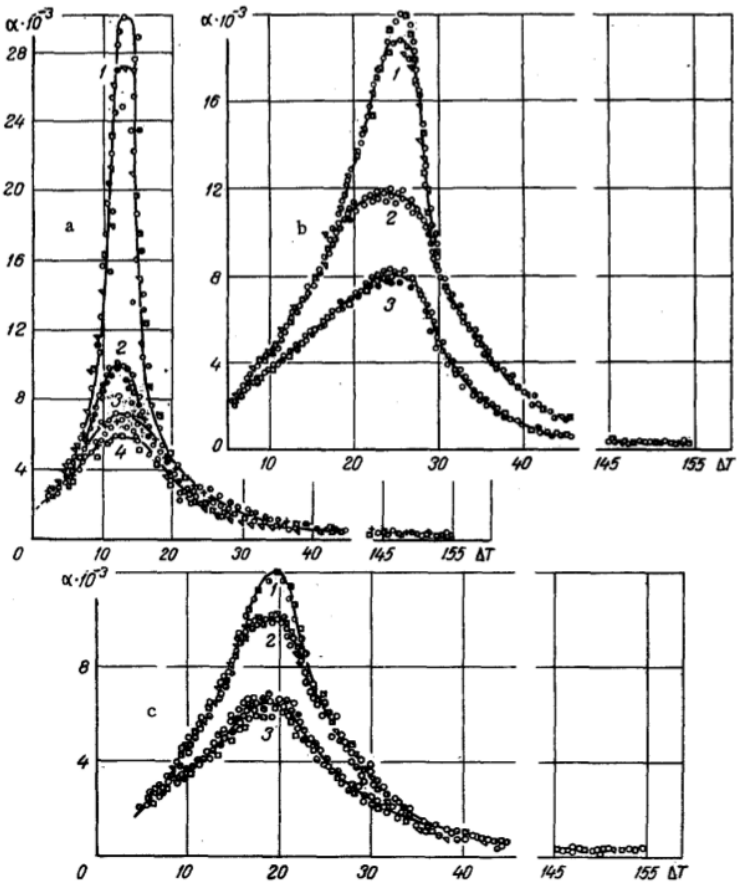

Figure 7.8.: Relation k to Logarithmic Mean Temperature Difference [7].

transfer coefficient for evaporative nitrogen heat exchangers was determined in [7] (see Figure 7.8. The values presented in this paper are much higher than those obtained in this investigated. However, this is in line with predictions; the regolith and vacuum create very poor conditions for heat exchange. P. E. Clark et al. [17] states:

> "[...] the extremely low thermal conductivity and heat capacity of the regolith severely limits the rate at which heat can be removed."

7.3.4. Evaluation of Test Rig and Experiment Procedures

Unforeseen flow behaviour could not be rectified without significant modifications to the test rig. Two-phase flow was exhibited through the heat exchanger. A method for the analysis of the experimental data was evolved, accounting for the predicted two-phase flow regimes. This analysis showed high consistency. The heat transfer coefficient was seen to have a strong temperature dependency, and a relationship was investigated for this dependency, thus allowing the heat transfer coefficient to be determined for various temperatures, or, applicable to the SPG design; at various depths in the lunar soil.

Analysis of data was hampered due to the low number of experiments completed. The relationship of the heat transfer coefficient to regolith temperature could not be consolidated. However, the values obtained were highly consistent, therefore further experiments can be performed using the same equipment and procedures to provide a sufficiently rigorous investigation.

To improve the performance of the test rig, some adaptions are proposed. One problem was the pressure oscillations in the nitrogen tank. In the current test rig setup, this problem was alleviated with the use of an additional valve and manometer. To better control the pressure in the nitrogen pipe and therefore the nitrogen flow velocity, an extra nitrogen cylinder with a moderator can be added. This would dampen the pressure oscillations from the liquid nitrogen tank by increasing the tank ullage pressure. Another result of this thesis was the estimation of the heat capacity of the lunar regolith simulant. Because of the value found, the cooling of the regolith is not easy to achieve with the current setup. To improve this situation, an additional cooling system could be installed to cool the regolith down before starting the measurements. Future investigations could involve long run-times, to obtain constant, cooler regolith temperatures and to better represent the operating period and cycles of the SPG.

8. Summary and Outlook

A permanent lunar outpost needs permanent energy supply. Due to the long lasting lunar night, it is not possible to provide this energy just with solar cells. To survive the lunar night another, constant energy source is needed. To fulfil this need, the SPG concept was proposed. Comparable to a geothermal power generator, the SPG would use thermal energy from the Moon to power a dynamic conversion cycle to generate electric energy. To support the design of a power generation system, the heat transfer from the lunar regolith to the power generation system itself is needed. The aim of this thesis is to determine these values experimentally. For this reason, a test rig is designed, constructed and verified to gain the heat transfer coefficient from regolith simulant to liquid nitrogen in the heat exchanger. In the task description the requirements for the test rig were defined. The requirements included

- a suitable regolith simulant,
- a vacuum,
- a setup reflecting the relevant parts of the SPG setup.

After designing the test rig and ordering the needed parts, the test rig was constructed. To verify its functionality, heat conductivity measurements were performed. In Chapter 7 the results from those measurements were evaluated, and a heat transfer coefficient of 73 - 124 W/(m^2·K) for temperatures between 291 and 325 K was determined. These values were validated by experimental data from geothermal experiments.

Although the objective for the development of the test rig and procedures was successfully achieved, it became also obvious that this simple design of heat exchanger is not suitable for the deployment on the Moon. The nitrogen did not undertake a complete phase change but ended up in a two-phase flow. While this was not optimal for the evaluation and determination of the heat transfer coefficient, it is also not optimal for the energy extraction on the Moon. A different heat exchanger design could help improve this situation and allow a complete phase change in the heat exchanger.

The experimental values for the heat transfer coefficient do, however, have great applicability in the continued development of the SPG concept. The obtained values are still representative of the system; going through a comparable temperature and enthalpy increase.

The technical challenges overcome in this thesis have set the ground work for continued SPG experimental investigations at the DLR Bremen. The test rig construction, calibration, optimisation, and trouble shooting provided the author with valuable experience and know-how. This knowledge has been passed on to the DLR SARA colleagues and DLR cryo-lab technicians, for the successful future use of the test rig. Furthermore,

the results have provided a model for the determination of heat transfer coefficient for thermodynamic cycle analysis. Two-phase flow evaluation techniques were created and utilised. The developed equipment, procedures and evaluation techniques can be utilised in future investigations to consolidate the heat transfer coefficient for a wider range of conditions, and to optimise the heat exchanger design. Finally, recommendations based on the experimental results to the SPG concept design were generated.

Bibliography

[1] P. Atkins and J. de Paula. *Atkins' Physical Chemistry*. 9th ed. OUP Oxford, 2010, 919 ff. ISBN: 9780199543373.

[2] H.D. Baehr and K. Stephan. *Heat and Mass Transfer*. 2nd ed. Physics and Astronomy. Springer, 2006. ISBN: 9783540295266.

[3] T. Ballatré et al. 'Analysis of energy supply options for lunar ISRU'. 2012.

[4] R. F. Barron. *Cryogenic Heat Transfer*. Series in Chemical and Mechanical Engineering. Taylor & Francis Group, 1999, 52ff, 143f. ISBN: 9781560325512.

[5] P. von Böckh and T. Wetzel. *Wärmeübertragung: Grundlagen und Praxis*. 4th ed. Springer-Lehrbuch. Berlin, Heidelberg: Springer, 2011, 4, 17, 218f. ISBN: 9783642159589.

[6] K. W. Bonfig. *Technische Durchflussmessung: Unter besonderer Berücksichtigung neuartiger Durchflussmessverfahren*. Vulkan-Verlag, 2002. ISBN: 9783802721908.

[7] E. S. Borovik et al. 'Heat Transfer during Boiling of Liquid Nitrogen at Coiled Heat Exchangers'. In: *Inzhenerno-Fizicheskii Zhurnal* 24.4 (04/1973), pp. 643–649.

[8] C. G. Brooks, J. M. Grimwood and L. S. Swenson. *Chariots for Apollo: a history of manned lunar spacecraft*. NASA History Series. Scientific, Technical Information Branch, National Aeronautics and Space Administration, 1979.

[9] C. Büttner. *Die Entstehung des Erdballs, Mondes und anderer grossen Weltkörper: Aus den Lagerungsverhältnissen der Erde abgeleitet*. Erlangen: Enke, 1847, 65f.

[10] A. G. W. Cameron and W. R. Ward. 'The Origin of the Moon'. In: *Lunar and Planetary Institute* (1976).

[11] R. M. Canup and E. Asphaug. 'Origin of the Moon in a giant impact near the end of the Earth's formation'. In: *Nature* 412 (08/2001), pp. 708–712.

[12] P. Carpenter. 'Characterization Strategies and Requirements for Lunar Regolith Simulant Materials'. In: *LRSM Workshop*. Huntsville, 2005.

[13] W. D. Carrier, J. K. Mitchell and A. Mahmood. 'The relative density of lunar soll'. In: *Proceedings of the Fourth Lunar Science Conference*. Vol. 3. 1973, pp. 2403–2411.

[14] H. S. Carslaw and J. C. Jaeger. *Conduction of Heat in Solids*. 2nd ed. London: Oxford University Press, 1959, p. 1.

[15] VDI-Gesellschaft Verfahrenstechnik und Chemieingenieurwesen. *VDI-Wärmeatlas: Berechnungsunterlagen für Druckverlust, Wärme- und Stoffübergang*. VDI-Buch Series Bd. 1. Springer Verlag, 2006, Dbc2. ISBN: 9783540255031.

[16] W. Chesworth. *Encyclopedia of Soil Science*. Encyclopedia of Earth Sciences Series. Springer, 2008, p. 306. ISBN: 9781402039942.

[17] P. E. Clark et al. 'Geothermal Systems Design for Lunar Surface Environment Science Activities'. In: *Annual Meeting of LEAG*. 2009.

[18] H. Czichos, T. Saito and L. Smith. *Springer Handbook of Materials Measurement Methods*. Springer handbooks. Springer, 2006, p. 401. ISBN: 9783540207856.

[19] Institut für Arbeitsschutz der Deutschen Gesetzlichen Unfallversicherung (IFA). *GESTIS-Stoffdatenbank*. 2013. URL: `http://gestis.itrust.de/nxt/gateway.dll?f=id$t=default.htm$vid=gestisdeu:sdbdeu$id=001530` (visited on 15/08/2013).

[20] R. C. Fernandes, R. Semiat and A. E. Dukler. 'Hydrodynamic model for gas-liquid slug flow in vertical tubes'. In: *AIChE Journal* 29.6 (1983), pp. 981–989. ISSN: 1547-5905. DOI: 10.1002/aic.690290617.

[21] N. N. Filina and J. G. Weisend. *Cryogenic Two-Phase Flow: Applications to Large Scale Systems*. Cambridge University Press, 1996, p. 18. ISBN: 9780521481922.

[22] M. Frandsen. *The heat capacity, heat of sublimation, and heat of solution of phosphorus pentoxide*. Vol. 10. 1. National Bureau of Standards, 1933, p. 35.

[23] H. K. Gupta, ed. *Encyclopedia of Solid Earth Geophysics*. Springer, 2011, p. 1431. ISBN: 9789048187010.

[24] *H250 Handbook*. KROHNE Messtechnik GmbH. 2011.

[25] A. Hadas. 'Heat Transfer in Dry Aggregated Soil: I. Heat Conduction'. In: *Soil Science Society of America Journal* 41.6 (1977), pp. 1055–1059.

[26] G. Heiken, D. Vaniman and B.M. French. *Lunar Sourcebook: A User's Guide to the Moon*. Cambridge University Press, 1991, p. 28. ISBN: 9780521334440.

[27] E. Hering and G. Schönfelder. *Sensoren in Wissenschaft und Technik: Funktionsweise und Einsatzgebiete*. Vieweg Verlag, Friedr, & Sohn Verlagsgesellschaft mbH, 2011, p. 382. ISBN: 9783834886354.

[28] R. T. Jacobsen, R. B. Stewart and M. Jahangiri. 'Thermodynamic Properties of Nitrogen from the Freezing Line to 2000 K at Pressures to 1000 MPa'. In: *Journal of Physical and Chemical Reference Data* 15.2 (1986), pp. 735–909. DOI: 10.1063/1.555754.

[29] S. B. Jacobsen. 'The Hf-W Isotopic System and the Origin of the Earth and Moon'. In: *Annual Review of Earth and Planetary Sciences* 33 (2005), pp. 531–570.

[30] R. Jaumann et al. 'Geology, geochemistry, and geophysics of the Moon: Status of current understanding'. In: *Planetary and Space Science* (2012), 9ff. ISSN: 0032-0633. DOI: 10.1016/j.pss.2012.08.019.

[31] K. Jousten. *Handbook of Vacuum Technology*. John Wiley & Sons, 2008, 277ff. ISBN: 9783527407231.

[32] C. Q. LaMarche, J. S. Curtis and P. T. Metzger. 'Permeability of JSC-1A: A lunar soil simulant'. In: *Icarus* 212.1 (2011), pp. 383 –389. ISSN: 0019-1035. DOI: 10.1016/j.icarus.2010.12.015.

[33] M. G. Langseth and S. J. Keihm. *In-Situ Measurements of Lunar Heat Flow*. The Lunar Science Institute, 1975.

[34] M. G. Langseth, S. J. Keihm and K. Peters. 'Revised lunar heat-flow values'. In: *Lunar Science Conference, 7th, Houston*. Vol. 3. New York: Pergamon Press, 1976, pp. 3143–3171.

[35] J. Leitner et al. 'Estimation of heat capacities of solid mixed oxides'. In: *Thermochimica Acta* 395.12 (2002), pp. 27 –46. ISSN: 0040-6031. DOI: 10.1016/S0040-6031(02)00177-6.

[36] E. W. Lemmon and R. T. Jacobsen. 'Viscosity and Thermal Conductivity Equations for Nitrogen, Oxygen, Argon, and Air'. In: *International Journal of Thermophysics* 25.1 (01/2004), pp. 21–69.

[37] D. Li. *Encyclopedia of Microfluidics and Nanofluidics*. Encyclopedia of Microfluidics and Nanofluidics. Springer, 2008. ISBN: 9780387324685.

[38] K. Lucas. *Thermodynamik*. Springer-Lehrbuch. Springer London, Limited, 2008, p. 353. ISBN: 9783540686484.

[39] V. Maiwald. *Discord between Gaia and Selene: Why selenothermal energy is insufficient for electrical power generation*. Tech. rep. Bremen: German Aerospace Center (DLR), 2013.

[40] T. D. McGee. *Principles and Methods of Temperature Measurement*. Wiley-Interscience publication. Wiley, 1988, 141ff, 237, 264f. ISBN: 9780471627678.

[41] D. S. McKay and J. D. Blacic. *Workshop on Production and Uses of Simulated Lunar Materials*. LPI Technical Report 91-01. Houston: Lunar and Planetary Institute, 1991.

[42] N. Naili et al. 'Experimental Analysis of Horizontal Ground Heat Exchanger for Northern Tunisia'. In: *Journal of Electronics Cooling and Thermal Control* 2 (2012), pp. 44–51. DOI: 10.4236/jectc.2012.23005.

[43] *Nichtrostender austenitischer Stahl 1.4404 - X2CrNiMo17-12-2*. Deutsche Edelstahlwerke. 03/2008.

[44] H. Oertel, M. Böhle and T. Reviol. *Strömungsmechanik: Grundlagen - Grundgleichungen - Lösungsmethoden - Softwarebeispiele*. Studium Technik. Vieweg+Teubner Verlag, 2011, p. 153. ISBN: 9783834813978.

[45] G. R. Olhoeft and D. W. Strangway. 'Dielectric properties of the first 100 meters of the Moon'. In: *Earth and Planetary Science Letters* 24.3 (1975), pp. 394 –404. ISSN: 0012-821X. DOI: 10.1016/0012-821X(75)90146-6.

[46] C. Owens. *Characterization summary of JSC-1AF bulk lunar mare regolith simulant*. Tech. rep. 1.6.2. NASA, 12/2006.

[47] J. J. Papike, S. B. Simon and J. C. Laul. 'The Lunar Regolith: Chemistry, Mineralogy, and Petrology'. In: *Reviews of Geophysics and Space Physics* 20.4 (11/1982), pp. 761–826.

[48] S. Parzinger et al. 'Experimental Determination of the Thermal Conductivity of JSC-1A under Vacuum Conditions with a Cavity Receiver Breadboard Design for Regolith Heating'. In: *International Conference on Environmental Systems (ICES)*. American Institute of Aeronautics and Astronautics, 07/2012, p. 7.

[49] D. Rickman, C. McLemore and J. Fikes. 'Characterization summary of JSC-1A bulk lunar mare regolith simulant'. 06/2007.

[50] D. Rist. *Dynamik realer Gase: Grundlagen, Berechnungen und Daten für Thermogasdynamik, Strömungsmechanik und Gastechnik*. Springer, 1996, p. 480. ISBN: 9783540586388.

[51] C. M. Schrader and D. L. Rickman. *Figure of Merit Characteristics Compared to Engineering Parameters*. Tech. rep. National Aeronautics and Space Administration, 09/2010.

[52] W. Schröder. *Fluidmechanik*. Vol. 7. Aachener Beiträge zur Strömungsmechanik. Aachen: Wissenschaftsverlag Mainz in Aachen, 2004, p. 150. ISBN: 386130371x.

[53] L. Sibille et al. *Lunar Regolith Simulant Materials: Recommendations for Standardization, Production and Usage*. Tech. rep. National Aeronautics and Space Administration, 12/2005.

[54] Christopher Steins and Sadiq J. Zarrouk. 'Assessment of the geothermal space heating system at Rotorua Hospital, New Zealand'. In: *Energy Conversion and Management* 55.0 (2012), pp. 60 –70. ISSN: 0196-8904. DOI: `http://dx.doi.org/10.1016/j.enconman.2011.10.013`.

[55] P. Stephan et al. *Thermodynamik*. Springer-Lehrbuch Bd. 1. Springer London, Limited, 2007, p. 321. ISBN: 9783540708148.

[56] *Stickstoff Produktinformation*. Air Liquide. 08/2001.

[57] D. B. Stoeser, S. Wilson and D. L. Rickman. *Preliminary Geological Findings on the BP-1 Simulant*. Tech. rep. National Aeronautics and Space Administration, 09/2010.

[58] K. W. Street Jr. et al. 'Thermal Properties of Lunar Regolith Simulants'. In: *Earth and Space 2010 Conference*. NASA. Honolulu, 2010.

[59] H.A. Stuart and G. Klages. *Kurzes Lehrbuch der Physik*. Springer-Lehrbuch. Springer, 2006, p. 113. ISBN: 9783540231462.

[60] Y. Taitel, D. Bornea and A. E. Dukler. 'Modelling flow pattern transitions for steady upward gas-liquid flow in vertical tubes'. In: *AIChE Journal* 26.3 (1980), pp. 345–354. ISSN: 1547-5905. DOI: `10.1002/aic.690260304`.

[61] J. R. Thome. *Engineering Data Book III*. Wolverine Tube, Inc., 2010, 13–1f.

[62] L. Tong and Y.S. Tang. *Boiling Heat Transfer and Two-phase Flow*. 2nd ed. Series in chemical and mechanical engineering. Taylor & Francis, 1997, p. 122. ISBN: 9781560324850.

[63] M. Wächter. *Tabellenbuch der Chemie: Daten zur Analytik, Laborpraxis und Theorie*. 1st ed. Wiley-VCH, 2012, 92 ff. ISBN: 9783527329601.

[64] J. Walker. *Boiling and the Leidenfrost effect*. URL: http://www.wiley.com/college/phy/halliday320005/pdf/leidenfrost_essay.pdf.

[65] D. R. Williams. *Lunar Exploration Timeline*. 2011. URL: http://nssdc.gsfc.nasa.gov/planetary/lunar/lunartimeline.html (visited on 15/10/2012).

[66] W. D. Woods. *How Apollo Flew to the Moon*. Springer Praxis Books in Space Exploration. Berlin, Heidelberg, New York: Springer Verlag, 2008, 25ff, 44ff. ISBN: 9780387716756.

[67] Y. Xu et al. 'Evaluation of frictional pressure drop correlations for two-phase flow in pipes'. In: *Nuclear Engineering and Design* 253.0 (2012). <ce:title>SI : CFD4NRS-3</ce:title>, pp. 86 –97. ISSN: 0029-5493. DOI: http://dx.doi.org/10.1016/j.nucengdes.2012.08.007.

[68] X. Zeng et al. 'Geotechnical Properties of JSC-1A Lunar Soil Simulant'. In: *Journal of Aerospace Engineering* 23.2 (2010), pp. 111–116. DOI: 10.1061/(ASCE)AS.1943-5525.0000014.

A. Appendix

A.1. Procedures and Checklists for the Usage of the Test Rig

In the following sections important procedures and checklists are listed. These procedures were used to guarantee a safe and correct execution of the experiments.

A.1.1. Vacuum Chamber Evacuation and Ventilation Procedure

Following the integration of the Pt100 temperature sensors, heating wire connection, nitrogen connection, and inner regolith container, the vacuum chamber is closed. The vacuum chamber is then evacuated. This involves the following procedure:

1. Check if all valves are closed.
2. Turn on the vacuum pump.
3. Open the "Inert Gas Outlet" valve slightly until the pressure sensors starts indicating a variation in pressure.
4. After the pressure has fallen to 15 kPa the "Inert Gas Outlet" valve can be opened completely.

From this point on it takes several hours to days to create a good-quality vacuum of at least low-tenths of a mbar.

The procedure in the event that the vacuum chamber has to be opened again:

1. Close all valves.
2. Turn off the vacuum pump.
3. Open the vent valve.
4. Slowly open the "Inert Gas Outlet" valve until ambient pressure is reached in the vacuum chamber.

Only following the execution of all of these steps, may the vacuum chamber be re-opened.

A.1.2. Heating Wire Power-On Procedure

In case that experiments are to be performed with heating of the regolith, the following steps have to be undertaken:

1. Check at several points with a multimeter for short circuits at the test rig to prevent bodily harm.

2. Turn on the power supply.
3. Press the preview button, “Prev”, and set everything to the desired output voltage and current (maximum allowed current due to safety reasons is 40 A).
4. The press button “Out” turns on the heating wire electrical circuit.
5. Now the voltage and current can be adjusted manually.
6. To stop the current flow, press “Out” again.
7. Turn off the power supply.

A.1.3. Experiment Execution Checklist

The execution of the experiments should follow this checklist to ensure all required steps are completed.

Before the experiment:

1. Check if all connections (especially the Nitrogen connections) are closed.
2. Put the Nitrogen outlet into the provided catch tank.
3. Check at several points for electrical short circuits at the test rig to prevent bodily harm.
4. Turn on all measuring instruments:
   - Measuring computer,
   - Temperature monitor,
   - Power source for the flow meter,
   - Pressure monitor,
   - Scales,
   - Power supply for the heating wire.
5. Delete or relocate all files in the location where the data is saved.
6. Determine the temperature of the water in the after-heater.
7. Read out the pressure in the LN tank and in the vacuum chamber.
8. Set the output voltage and current and press “Out”.
9. Start the measurement in LabVIEW®.
10. Start the nitrogen flow.

After the experiment:

1. Close the LN valve and stop the LN flow.

2. Stop the current flow.
3. Read out the pressure in the LN tank and in the vacuum chamber.
4. Determine the temperature of the water in the after-heater.
5. Read out the mass on the scales.
6. Stop the measurement in LabVIEW®.
7. Rename all created files to the desired name.
8. Save all created files externally.

A.2. Test Protocols

In this section all performed tests at the test rig are protocolled.

A.2.1. Test 1

Title: First testing **Date:** 15.07.2013

Experimenters:	Thomas Ballatré, Michael Elsen
Goal/Motivation:	Functionality testing of the test rig and first starting of the nitrogen flow.
Execution:	After starting the nitrogen flow, the correct functionality is checked.
Parameters:	$p_{chamber}$ = 850 Pa $p_{LN\ tank}$ = 250 kPa T_{water} = - U = 0 V I = 0 A
Results:	$p_{chamber}$ = 540 Pa $p_{LN\ tank}$ = 250 kPa T_{water} = - U = 0 V I = 0 A t_{N_2} = 314 s m_{N_2} = 0.76 kg
Observations:	-

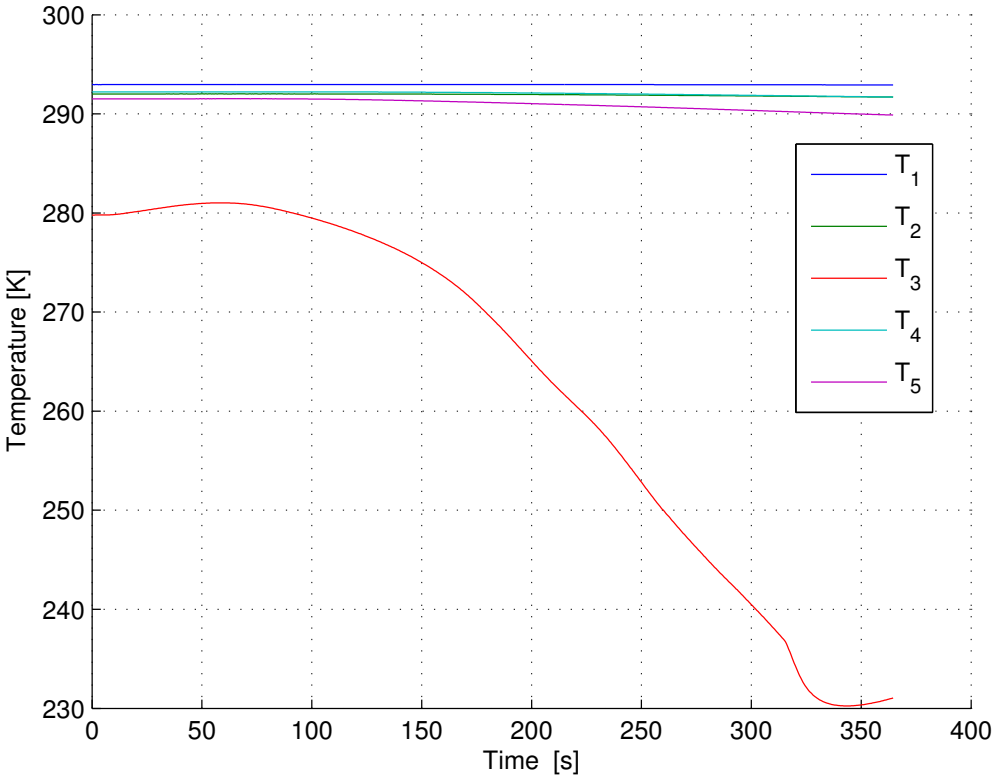

Figure A.1.: Pt100 Temperatures, Test 1.

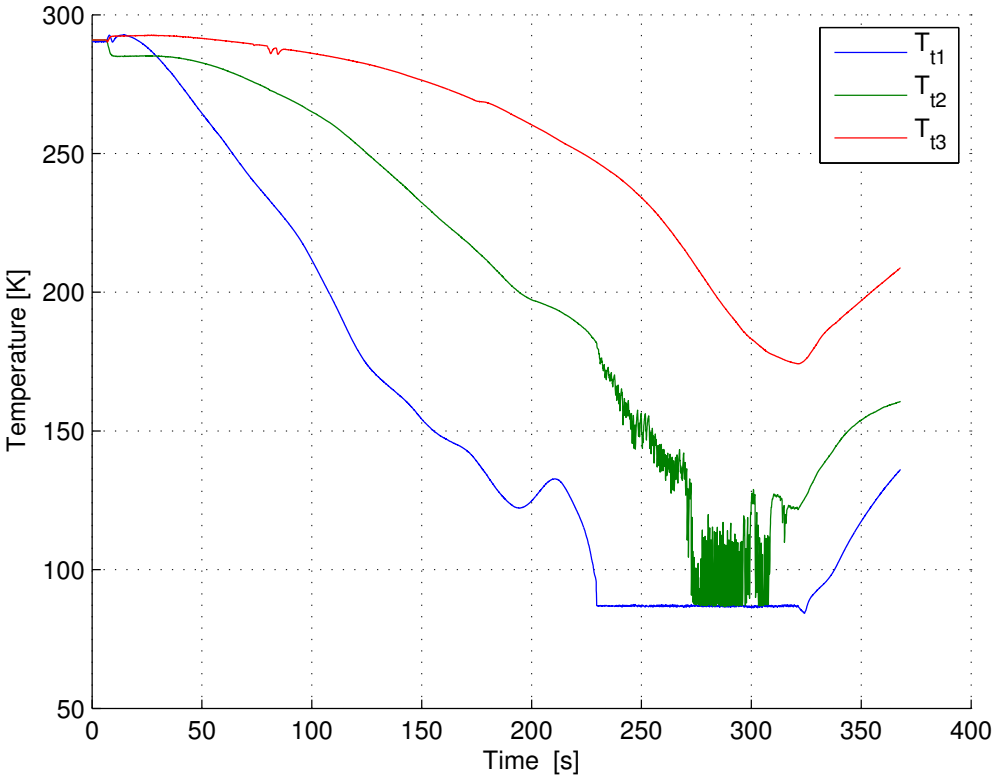

Figure A.2.: Thermocouple Temperatures, Test 1.

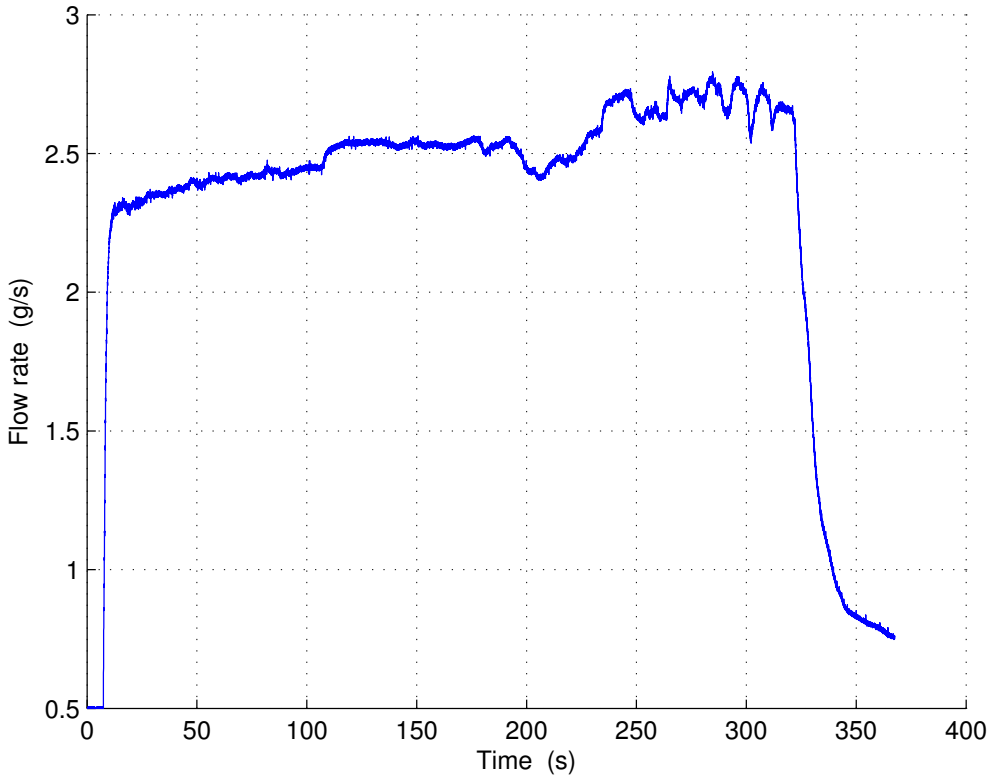

Figure A.3.: Mass Flow Rate, Test 1.

A.2.2. Test 2

Title: First testing **Date:** 16.07.2013

Experimenters:	Thomas Ballatré, Michael Elsen
Goal/Motivation:	Functionality testing of the test rig, especially of the new after-heater.
Execution:	After starting the nitrogen flow the correct functionality is checked.
Parameters:	$p_{chamber}$ = 1000 Pa $p_{LN\ tank}$ = 250 kPa T_{water} = N/A U = 0 V I = 0 A
Results:	$p_{chamber}$ = 490 Pa $p_{LN\ tank}$ = 250 kPa T_{water} = 303.35 K U = 0 V I = 0 A t_{N_2} = 462 s m_{N_2} = 0.75 kg
Observations:	Due to a memory error the Pt100 sensors were not recorded. The temperature within the regolith had minimal change.

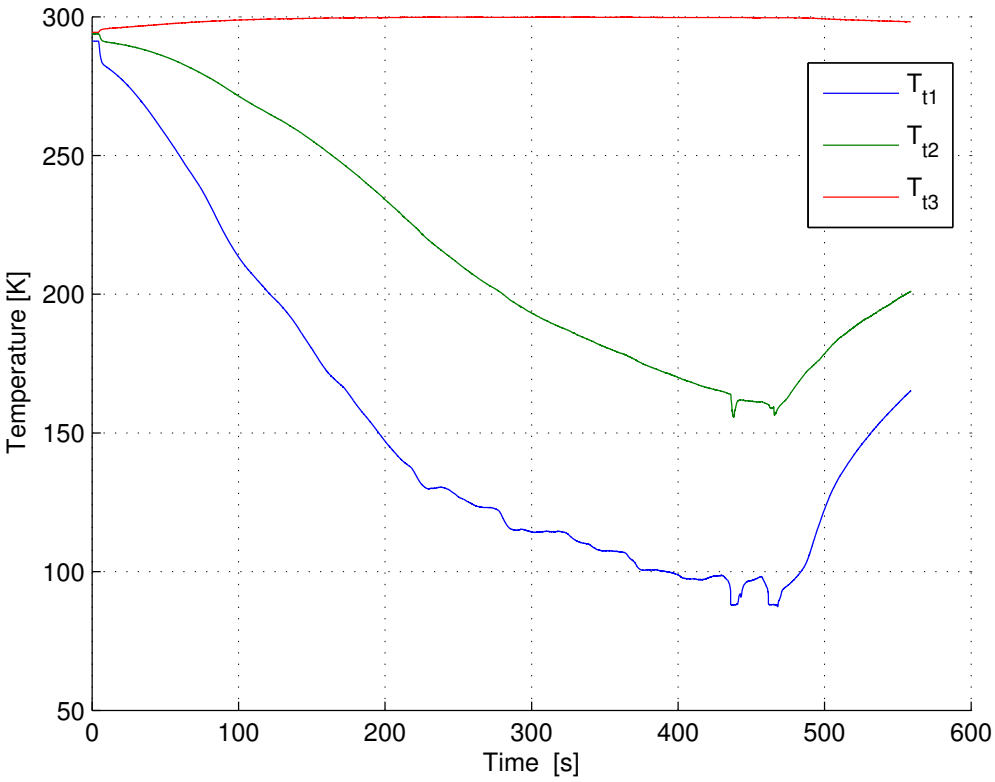

Figure A.4.: Thermocouple Temperatures, Test 2.

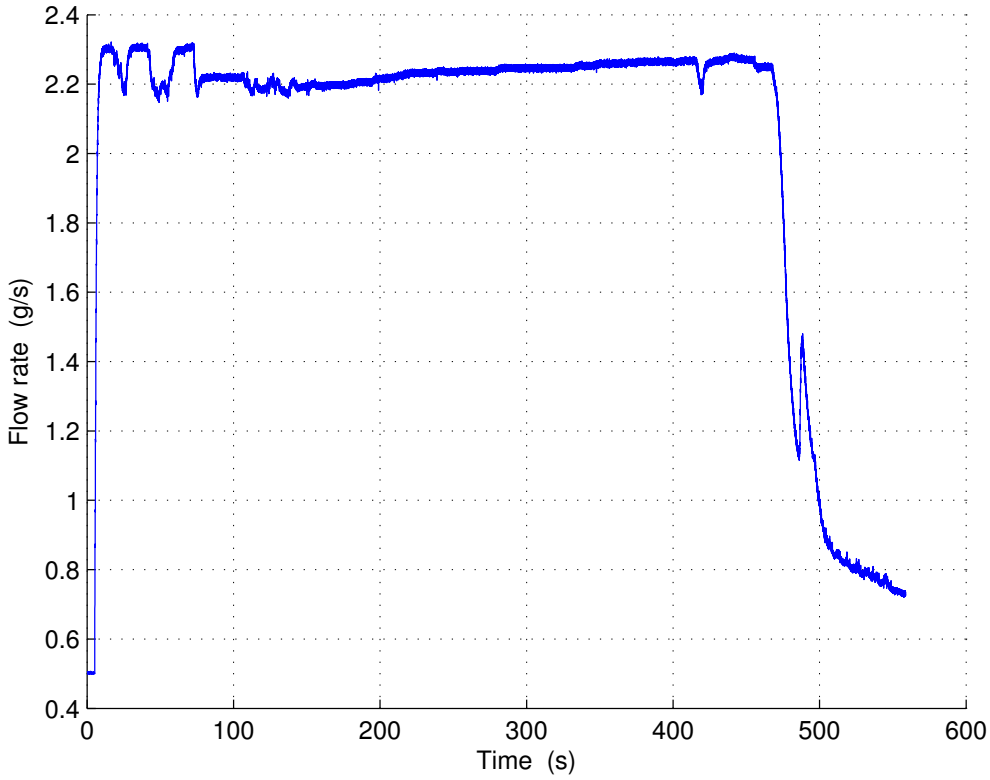

Figure A.5.: Mass Flow Rate, Test 2.

A.2.3. Test 3

Title: Leakage test **Date:** 22.07.2013

Experimenters: Thomas Ballatré, Michael Elsen

Goal/Motivation: Vacuum chamber tightness testing.

Execution: Creating a vacuum in the empty vacuum chamber.

Parameters:
$p_{chamber}$ = 101.3 kPa
$p_{LN\ tank}$ = -
T_{water} = -
U = -
I = -

Results:
$p_{chamber}$ = 24 Pa
$p_{LN\ tank}$ = -
T_{water} = -
U = -
I = -
t = 2.5 h
m_{N_2} = -

Observations: The vacuum quality was still improving at the termination of the experiment.

A.2.4. Test 4

Title: Leakage test **Date:** 22.07.2013

Experimenters: Thomas Ballatré, Michael Elsen

Goal/Motivation: Vacuum chamber tightness testing.

Execution: Creating a vacuum in the empty vacuum chamber.

Parameters:
$p_{chamber}$ = 101.3 kPa
$p_{LN\ tank}$ = -
T_{water} = -
U = -
I = -

Results:
$p_{chamber}$ = 9.5 Pa
$p_{LN\ tank}$ = -
T_{water} = -
U = -
I = -
t = 45 min
m_{N_2} = -

Observations: The vacuum quality was still improving at the termination of the experiment.

A.2.5. Test 5

Title: Heating wire test **Date:** 23.07.2013

Experimenters: Thomas Ballatré, Michael Elsen

Goal/Motivation: Basic testing of the heating wire to prove its functionality.

Execution: Observing the changes in temperature after turning on the power supply for the heating wire.

Parameters:
$p_{chamber}$ = 140 Pa
$p_{LN\ tank}$ = -
T_{water} = -
U = 9.09 V
I = 23.9 A

Results:
$p_{chamber}$ = 160 Pa
$p_{LN\ tank}$ = -
T_{water} = -
U = 8.95 V
I = 23.9 A
t = 13 min
m_{N_2} = -

Observations: -

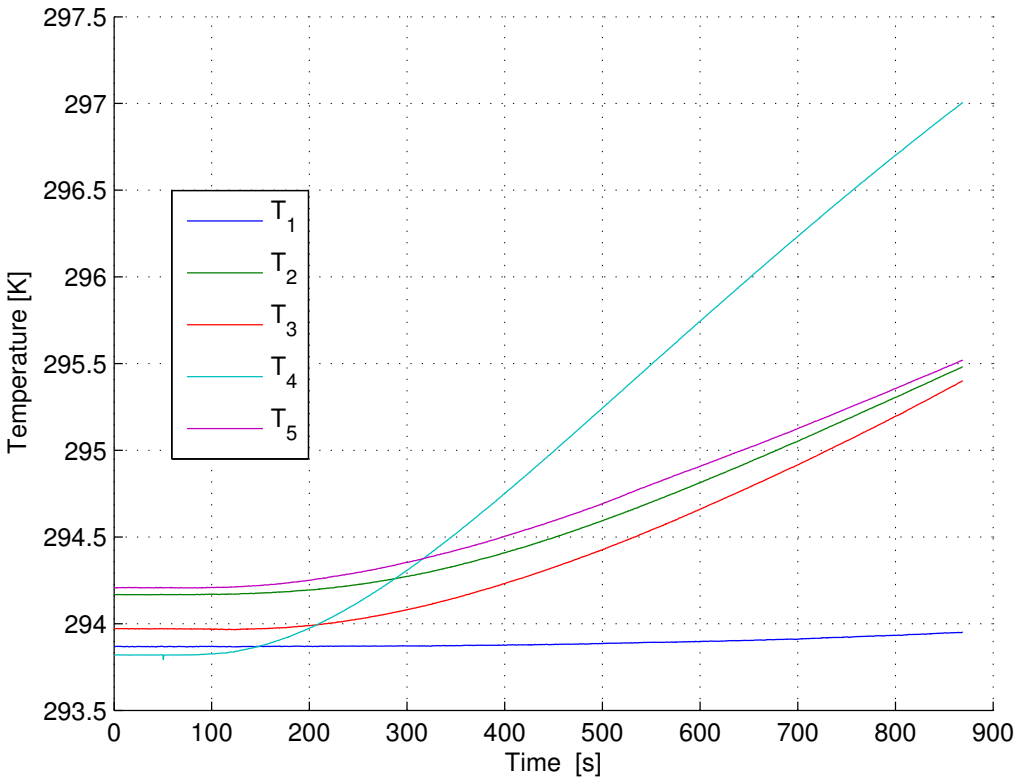

Figure A.6.: Pt100 Temperatures, Test 5.

A.2.6. Test 6

Title: Heating wire test **Date:** 23.07.2013

Experimenters:	Thomas Ballatré, Michael Elsen
Goal/Motivation:	Basic testing of the heating wire to prove its functionality.
Execution:	Observing the changes in temperature after turning on the power supply for the heating wire.
Parameters:	$p_{chamber}$ = 140 Pa $p_{LN\ tank}$ = - T_{water} = - U = 14.99 V I = 40 A
Results:	$p_{chamber}$ = 470 Pa $p_{LN\ tank}$ = - T_{water} = - U = 9.49 V I = 40 A t = ~30 min m_{N_2} = -
Observations:	-

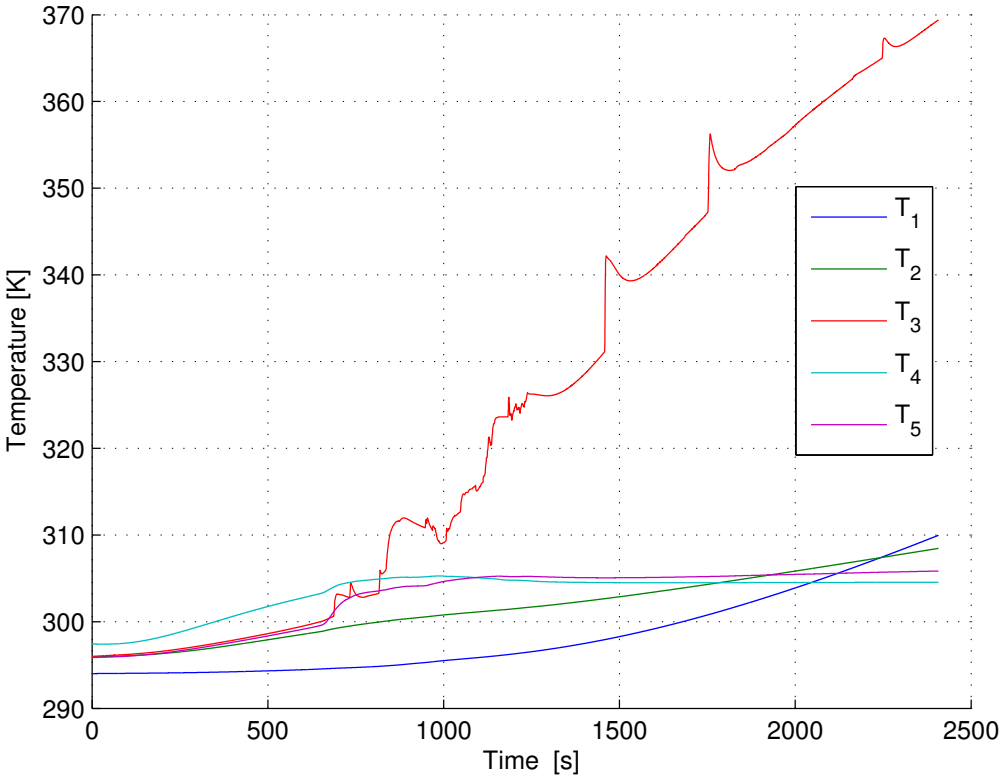

Figure A.7.: Pt100 Temperatures, Test 6.

A.2.7. Test 7

Title: Calibration of Pt100 **Date:** 23.07.2013

Experimenters: Thomas Ballatré, Michael Elsen

Goal/Motivation: Calibrating the Pt100 sensors

Execution: -

Parameters:
$p_{chamber}$ = -
$p_{LN\ tank}$ = -
T_{water} = 273.15 K
U = -
I = -

Results:
$p_{chamber}$ = -
$p_{LN\ tank}$ = -
T_{water} = 273.15 K
U = -
I = -
t = -
m_{N_2} = -

Observations: -

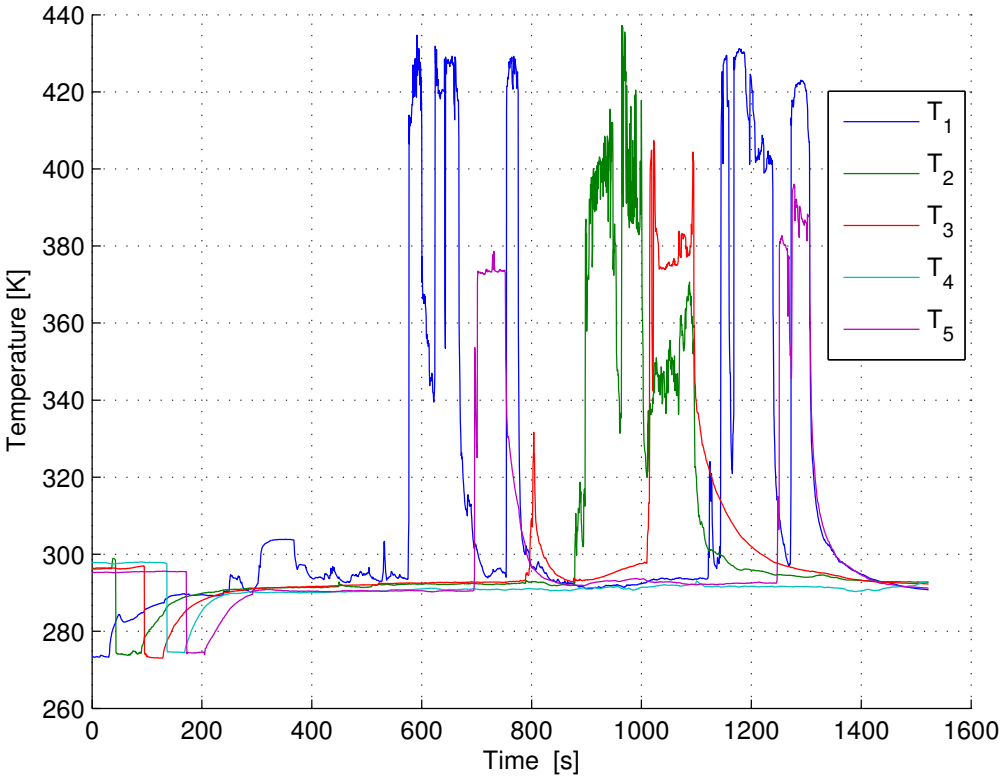

Figure A.8.: Pt100 Temperatures, Test 7.

A.2.8. Test 8

Title: Calibration of Pt100 **Date:** 23.07.2013

Experimenters: Thomas Ballatré, Michael Elsen

Goal/Motivation: Calibrating the Pt100 sensors

Execution: -

Parameters:
$p_{chamber}$ = -
$p_{LN\ tank}$ = -
T_{water} = 273.15 K
U = -
I = -

Results:
$p_{chamber}$ = -
$p_{LN\ tank}$ = -
T_{water} = 273.15 K
U = -
I = -
t = -
m_{N_2} = -

Observations: -

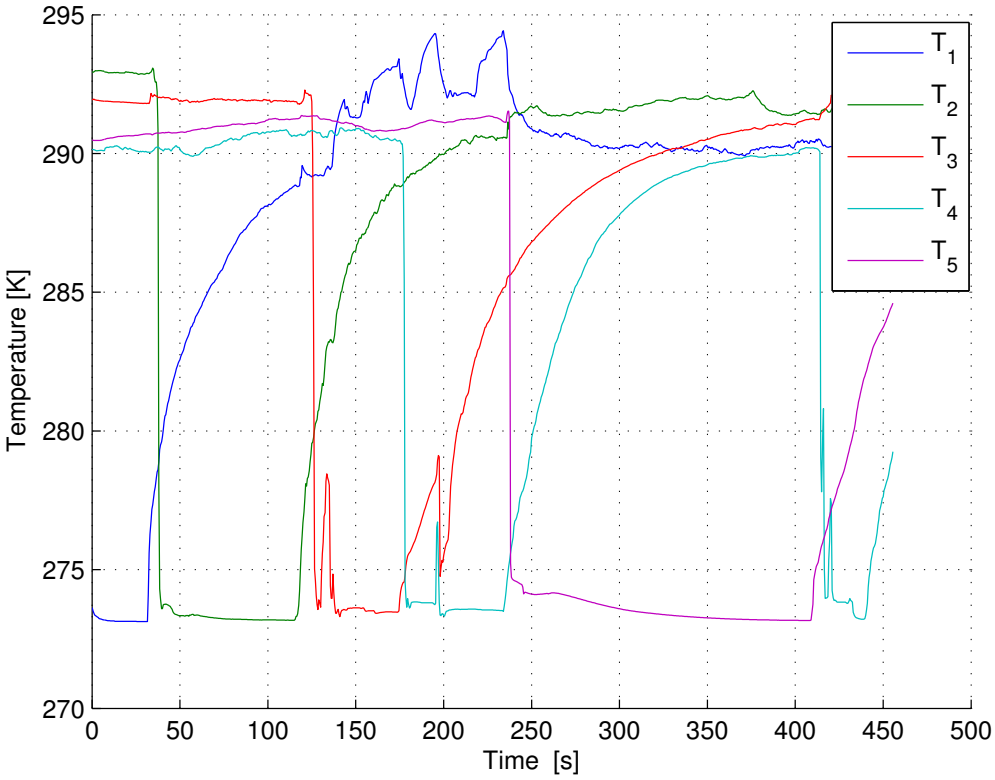

Figure A.9.: Pt100 Temperatures, Test 8.

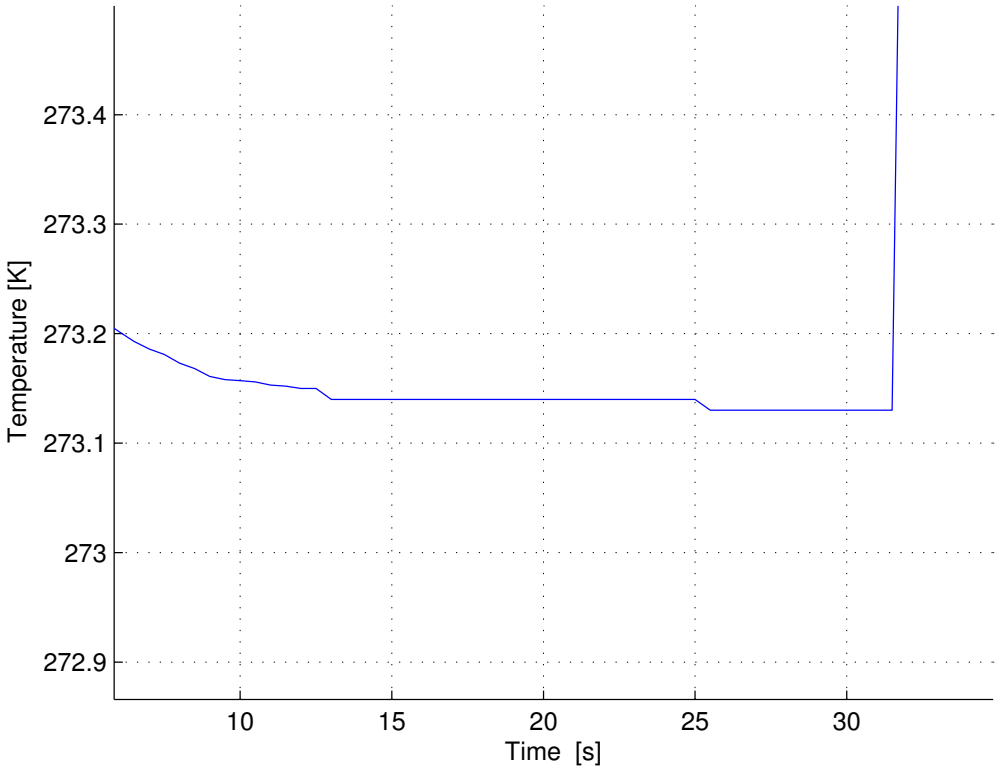

Figure A.10.: T1 Calibration, Test 8.

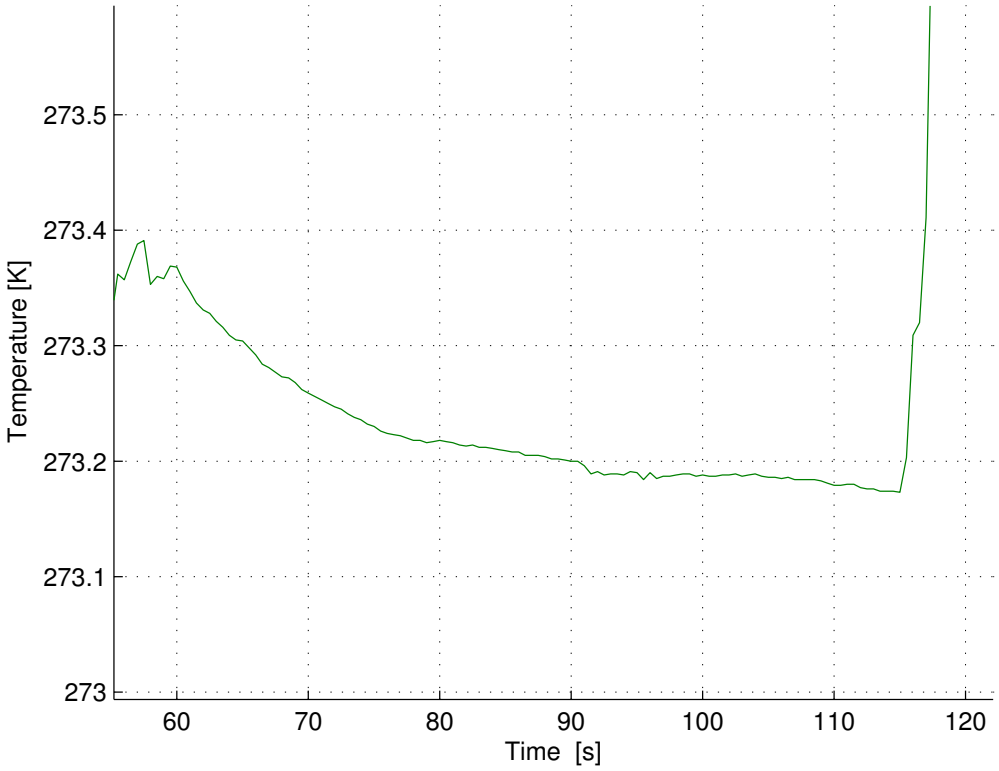

Figure A.11.: T2 Calibration, Test 8.

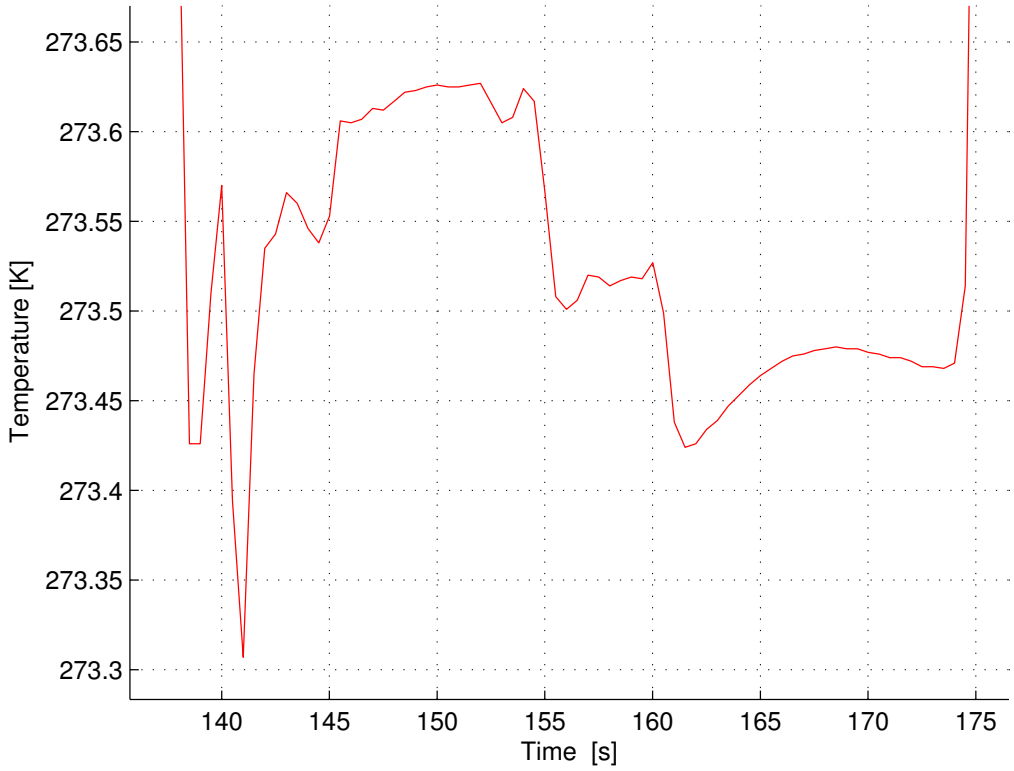

Figure A.12.: T3 Calibration, Test 8.

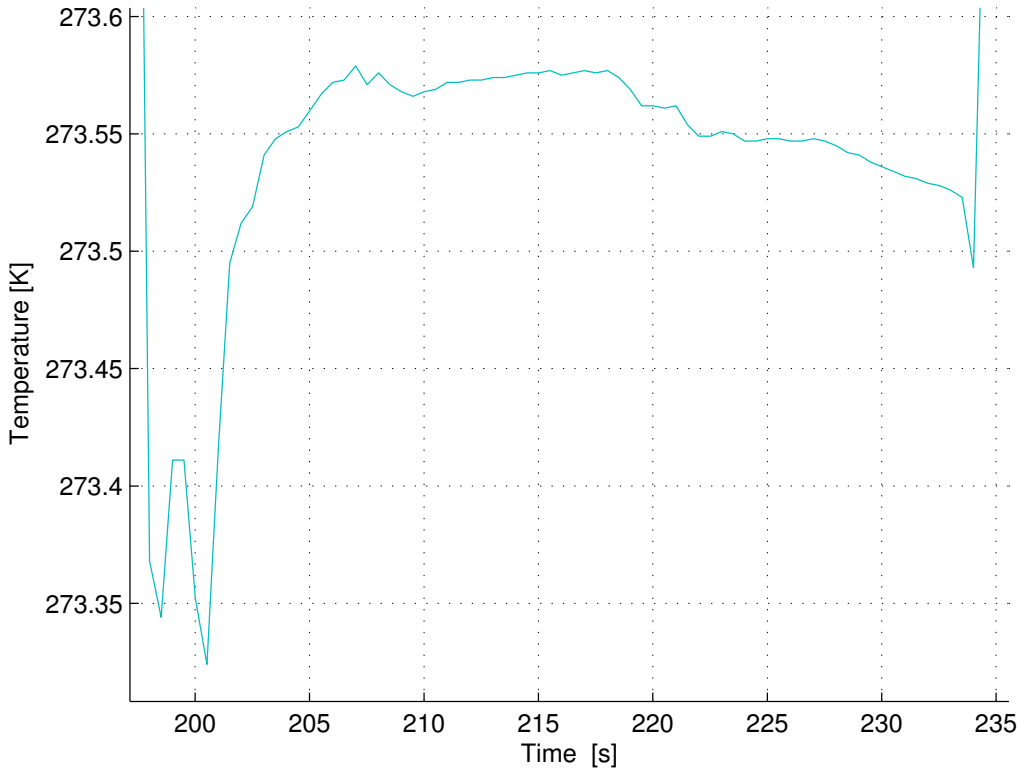

Figure A.13.: T4 Calibration, Test 8.

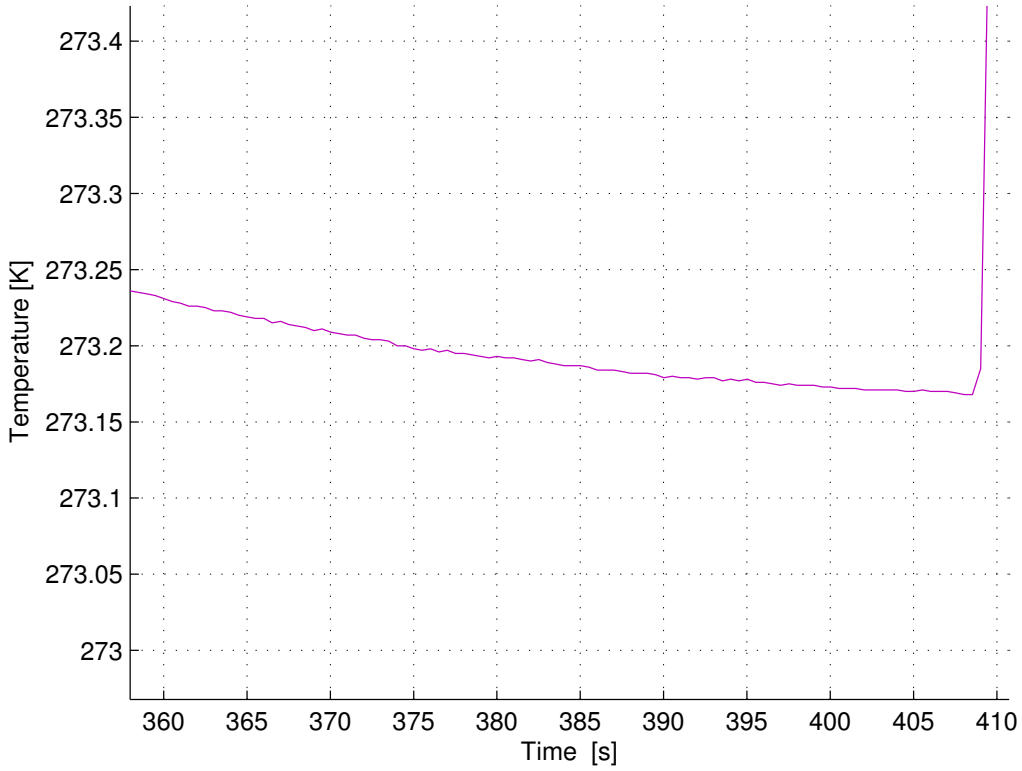

Figure A.14.: T5 Calibration, Test 8.

A.2.9. Test 9

Title: Heat transfer measurements at an increased temperature **Date:** 24.07.2013

Experimenters: Thomas Ballatré, Michael Elsen

Goal/Motivation: To test concurrent operation of every integrated component.

Execution: -

Parameters:
$p_{chamber}$ = 150 Pa
$p_{LN\ tank}$ = 250 kPa
T_{water} = 292.35 K
U = 3.68 V
I = 15 A

Results:
$p_{chamber}$ = 250 Pa
$p_{LN\ tank}$ = 250 kPa
T_{water} = 284.15 K
U = 3.68 V
I = 15 A
t = 30 min
m_{N_2} = 2.98 kg

Observations: $p_{chamber}$ is observed to first rise to 160 Pa, before falling to 55 Pa, and then rise again to the final pressure.
A loose contact at the mass flow meter at the beginning of the experiment caused an incomplete mass flow rate measurement.

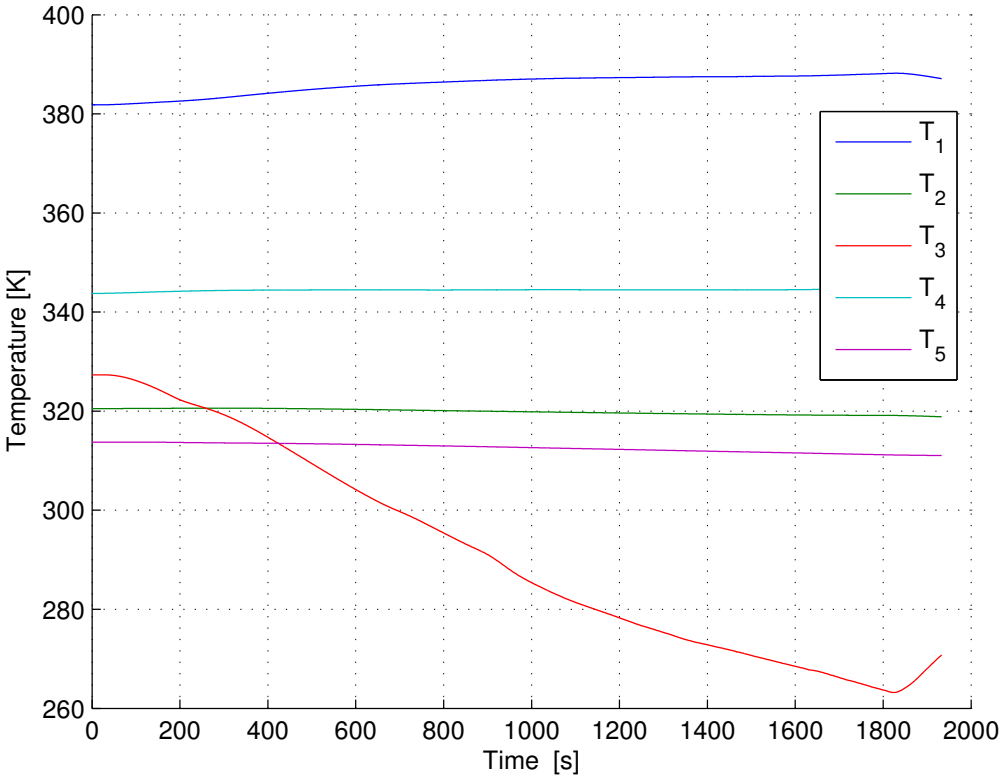

Figure A.15.: Pt100 Temperatures, Test 9.

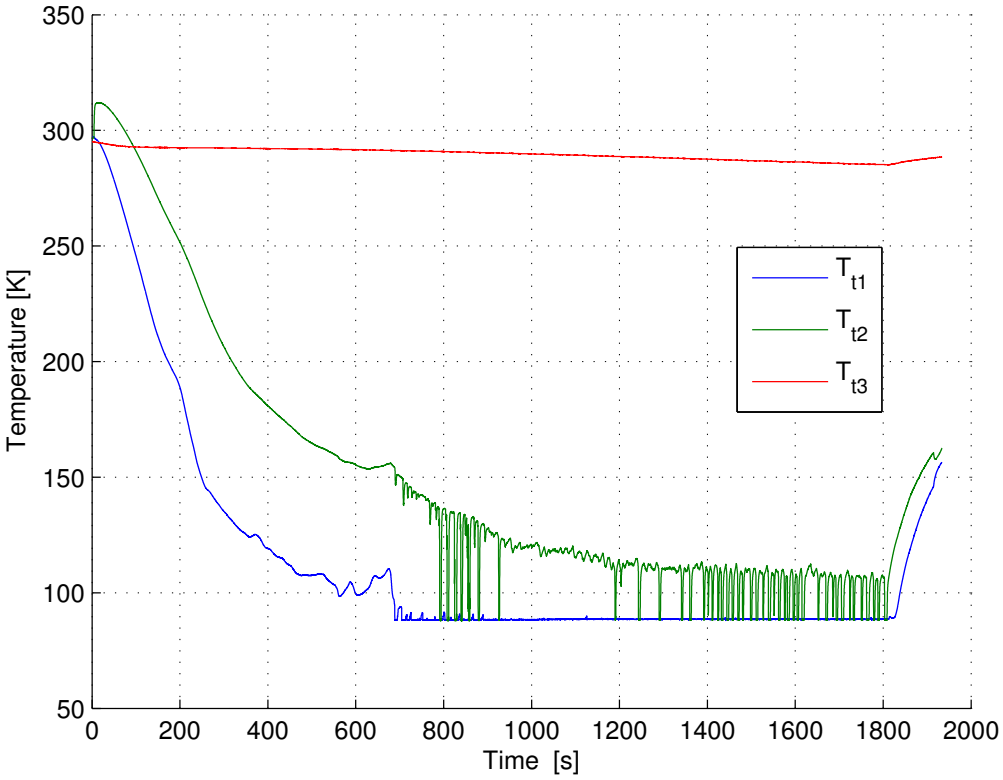

Figure A.16.: Thermocouple Temperatures, Test 9.

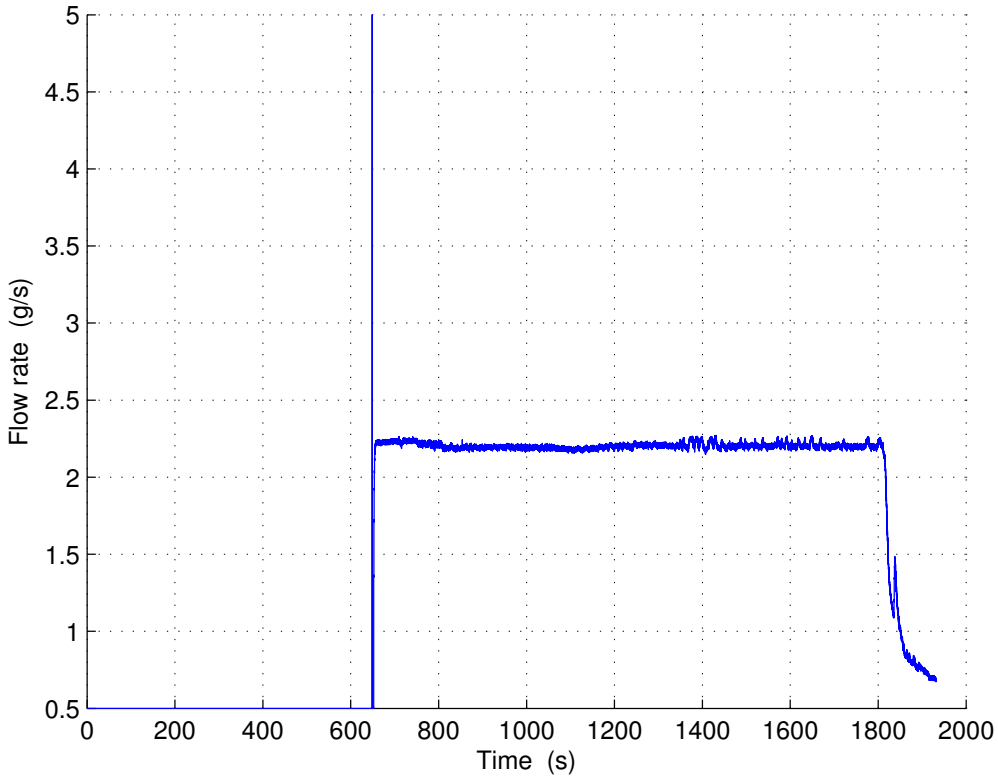

Figure A.17.: Mass Flow Rate, Test 9.

A.2.10. Test 10

Title: Heat transfer measurements at an increased temperature **Date:** 24.07.2013

Experimenters: Thomas Ballatré, Michael Elsen

Goal/Motivation: To find the minimal flow velocity to have single phase-flow at the nitrogen inlet.

Execution: -

Parameters:
$p_{chamber}$ = 89 Pa
$p_{LN\ tank}$ = 250 kPa
T_{water} = 302.55 K
U = 0 V
I = 0 A

Results:
$p_{chamber}$ = 98 Pa
$p_{LN\ tank}$ = 250 kPa
T_{water} = 300.85 K
U = 0 V
I = 0 A
t = ? min
m_{N_2} = 1.17 kg

Observations: $p_{chamber}$ is observed to first rise to 100 Pa, before falling to 56 Pa, and then oscillating between 98 Pa and 110 Pa.

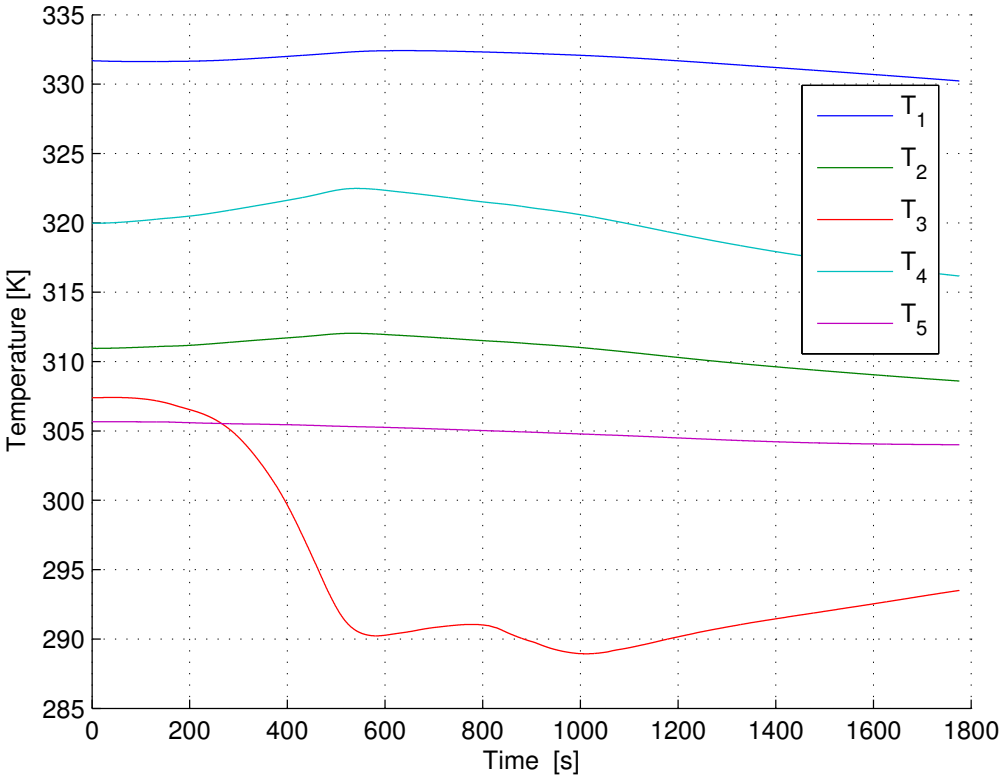

Figure A.18.: Pt100 Temperatures, Test 10.

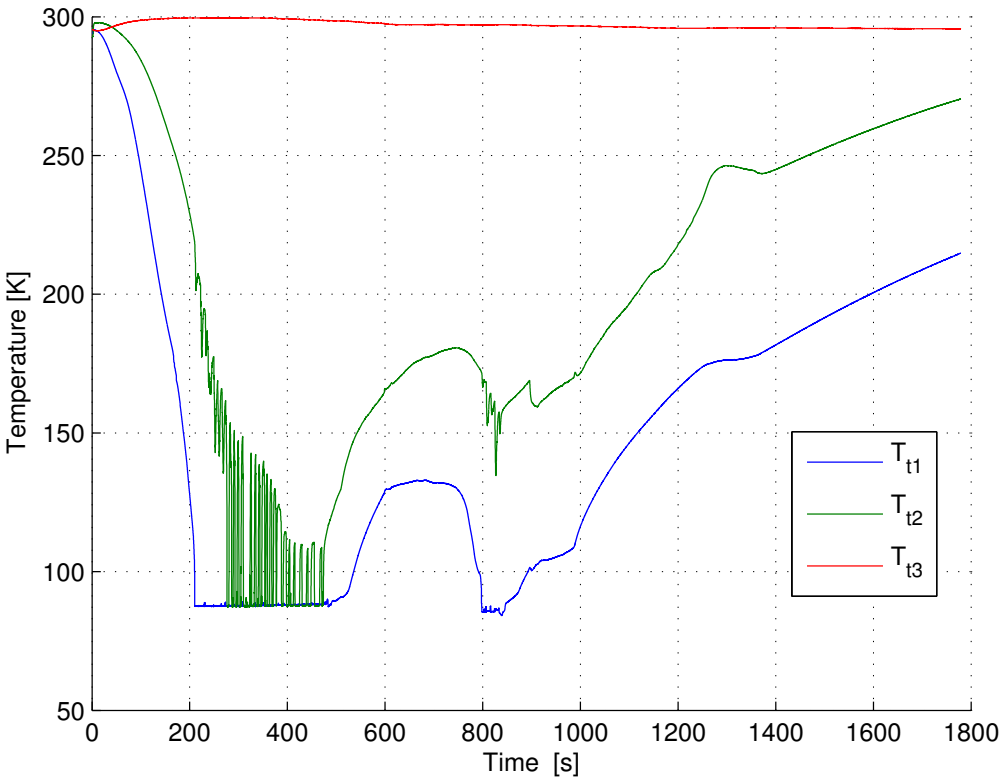

Figure A.19.: Thermocouple Temperatures, Test 10.

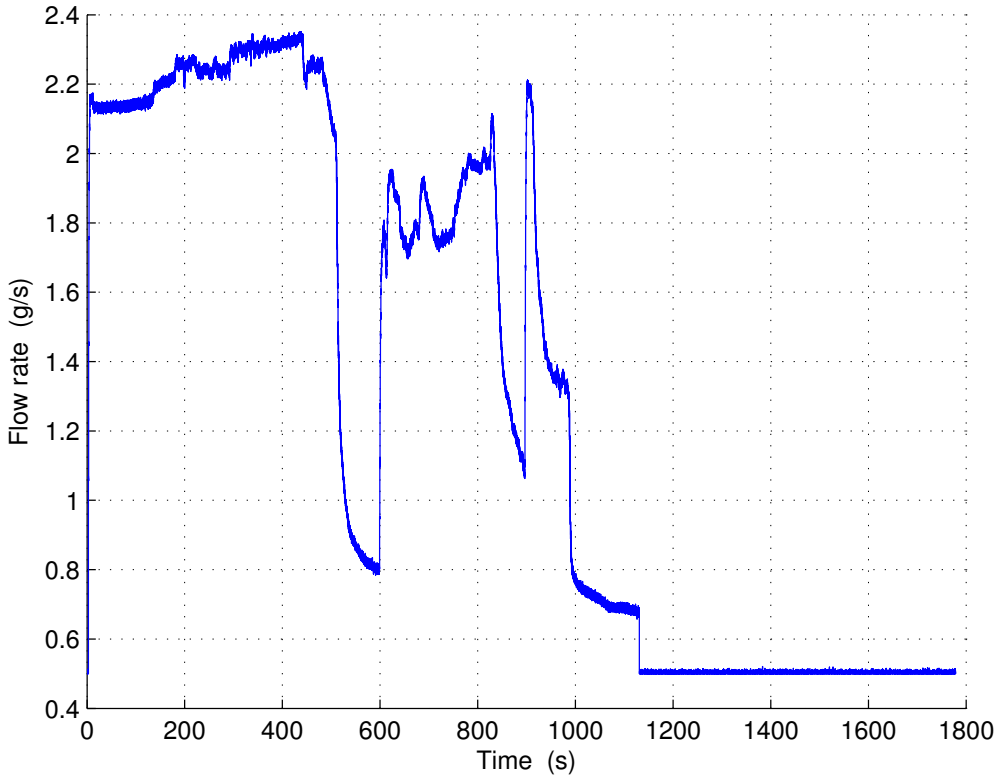

Figure A.20.: Mass Flow Rate, Test 10.

A.2.11. Test 11

Title: Determination of the electrical connection's resistance **Date:** 25.07.2013

Experimenters: Thomas Ballatré, Michael Elsen

Goal/Motivation: To determine the electrical resistance of the whole circuit (heating wire, current feedthrough and cable).

Execution: -

Parameters:
$p_{chamber}$ = -
$p_{LN\ tank}$ = -
$T_{hot\ plate}$ = 365 K
U = -
I = -

Results:
$p_{chamber}$ = -
$p_{LN\ tank}$ = -
$T_{hot\ plate}$ = 365 K
U = -
I = -
R = 0.44 Ω
t = -
m_{N_2} = -

Observations: -

A.2.12. Test 12

Title: Test of the new valve **Date:** 25.07.2013

Experimenters: Thomas Ballatré, Michael Elsen

Goal/Motivation: Controlled variation of the flow velocity.

Execution: -

Parameters:
$p_{chamber}$ = 83 Pa
$p_{LN\ tank}$ = 250 kPa
T_{water} = 293.25 K
U = 0 V
I = 0 A

Results:
$p_{chamber}$ = 87 Pa
$p_{LN\ tank}$ = 250 kPa
T_{water} = 285.05 K
U = 0 V
I = 0 A
t_{N_2} = 39 min 51 s
m_{N_2} = 2.64 kg

Observations: Pressure rises to 94 Pa, declines to 53 Pa and rises against to 250 Pa. After that it declines again. As soon as T_4 stops rising and starts declining, the pressure declines, too.

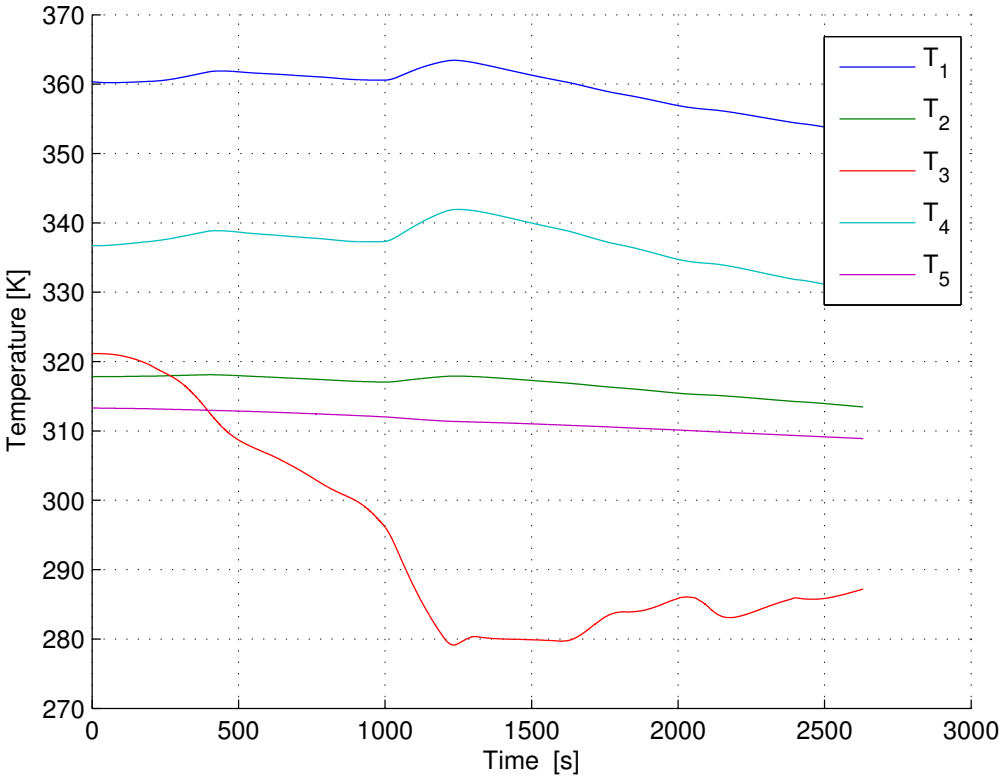

Figure A.21.: Pt100 Temperatures, Test 12.

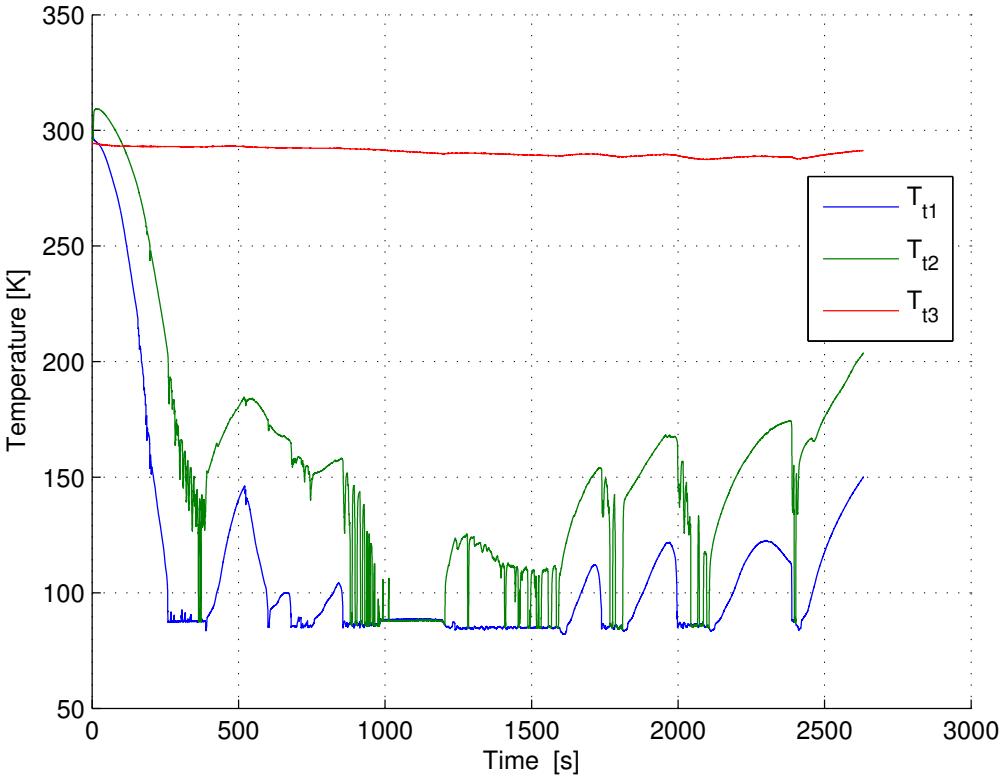

Figure A.22.: Thermocouple Temperatures, Test 12.

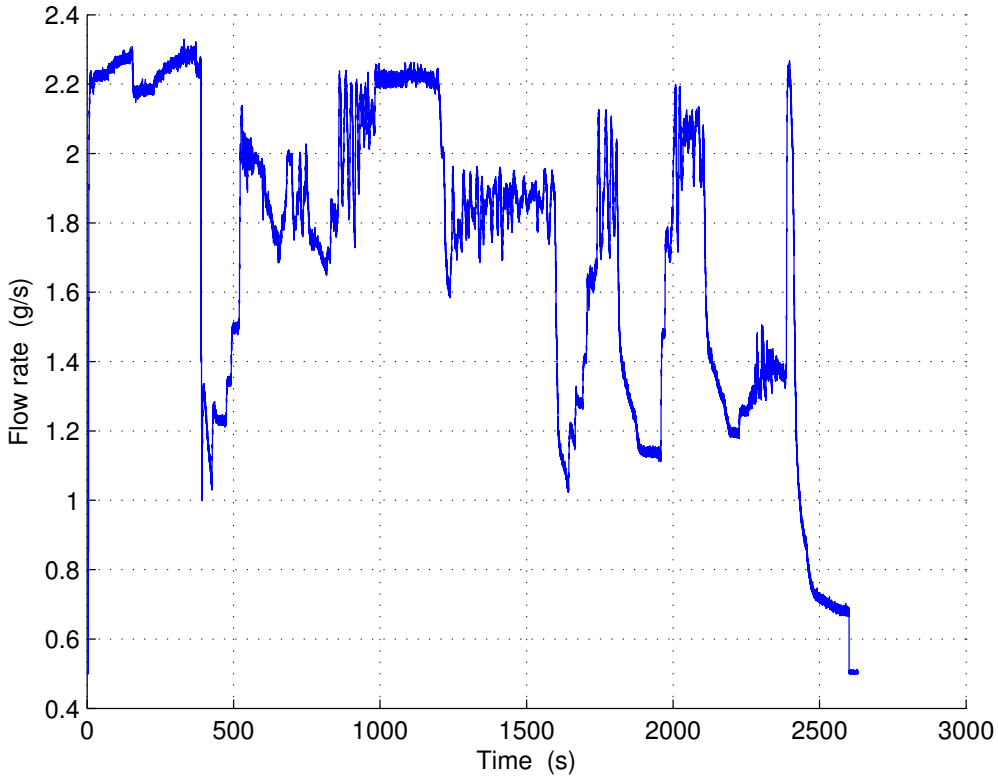

Figure A.23.: Mass Flow Rate, Test 12.

A.2.13. Test 13

Title: Calibration of the valve's new scale **Date:** 25.07.2013

Experimenters: Thomas Ballatré, Michael Elsen

Goal/Motivation: More exact setting of the flow velocity.

Execution: Stepwise reduction of the valve opening after previous cooling down of the nitrogen pipes in 2°and 60 s steps. After that the same procedure but enlarging the valve's opening.

Parameters:
$p_{chamber}$ = 63 Pa
$p_{LN\ tank}$ = 250 kPa
T_{water} = 285.25 K
U = 0 V
I = 0 A

Results:
$p_{chamber}$ = -
$p_{LN\ tank}$ = -
T_{water} = -
U = -
I = -
t_{N_2} = -
m_{N_2} = -

Observations: Abortion of the test.

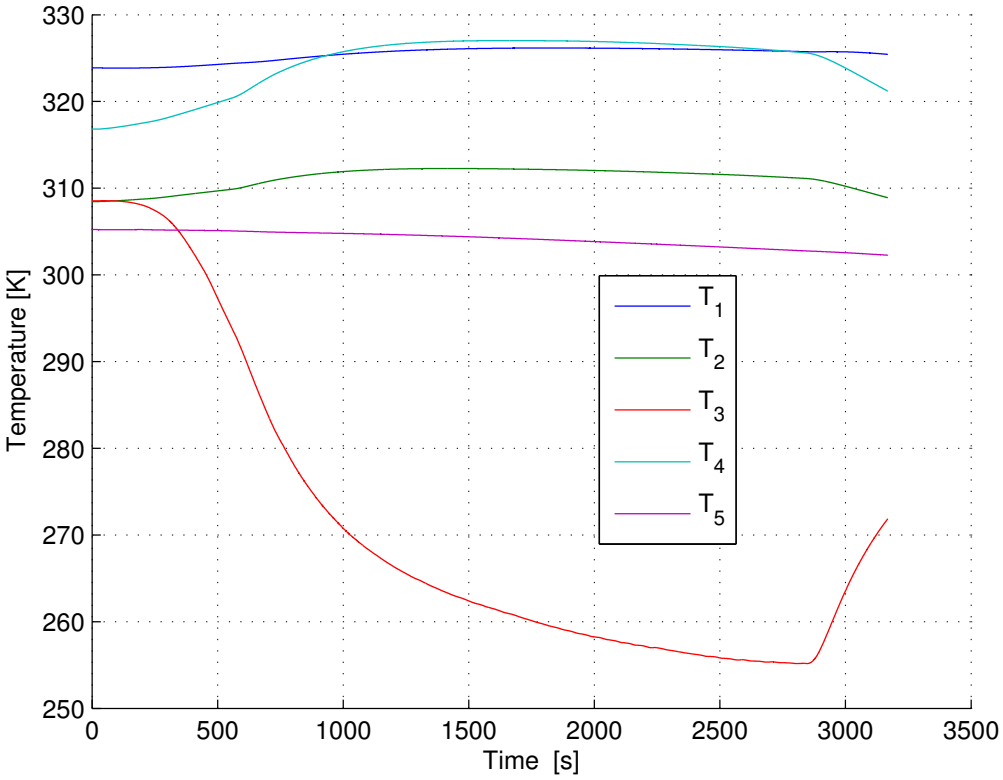

Figure A.24.: Pt100 Temperatures, Test 13.

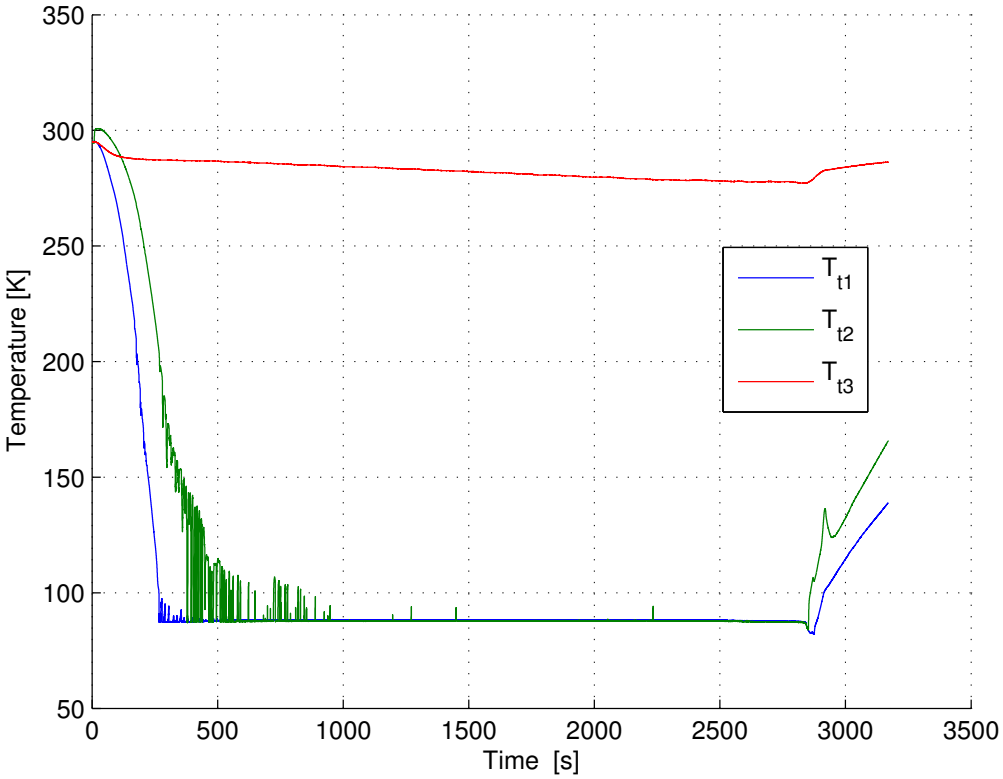

Figure A.25.: Thermocouple Temperatures, Test 13.

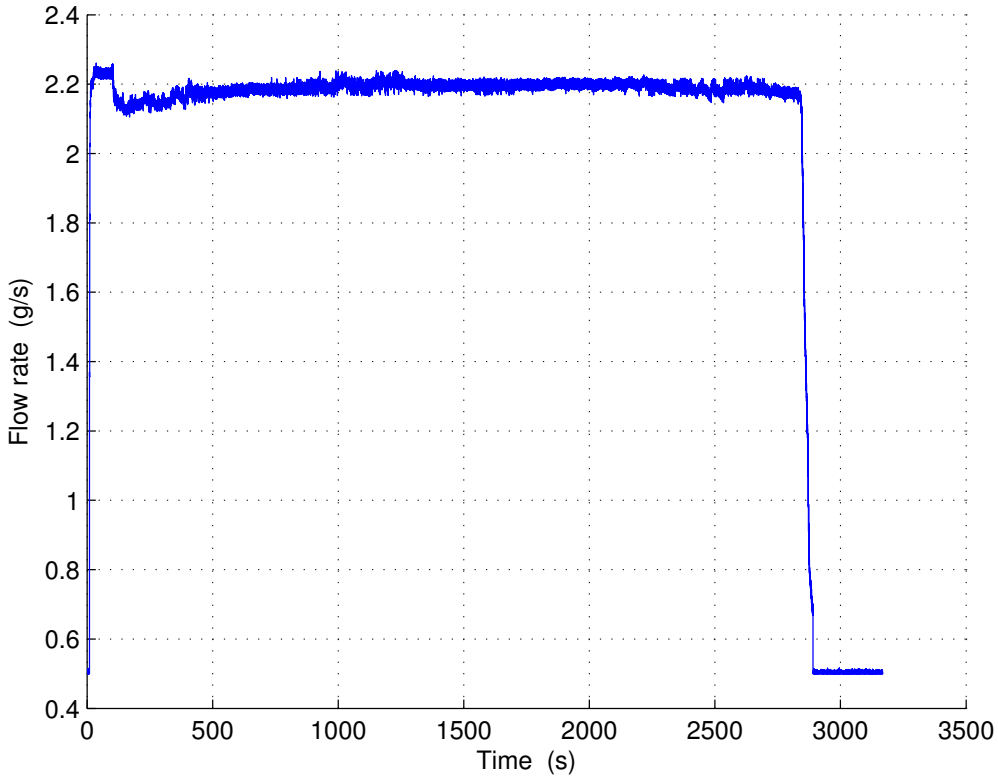

Figure A.26.: Mass Flow Rate, Test 13.

A.2.14. Test 14

Title: Test of the new manometer **Date:** 26.07.2013

Experimenters: Thomas Ballatré, Michael Elsen

Goal/Motivation: More exact and reproducible setting of the flow velocity.

Execution: -

Parameters:
$p_{chamber}$ = 43 Pa
$p_{LN\ tank}$ = 250 kPa
T_{water} = 304.75 K
U = 0 V
I = 0 A

Results:
$p_{chamber}$ = 210 Pa
$p_{LN\ tank}$ = 250 kPa
T_{water} = 298.55 K
U = 0 V
I = 0 A
t_{N_2} = ?
m_{N_2} = 1.81 kg

Observations: At 106°on the valve's scale, there is a more or less constant pressure in the nitrogen pipe of ~0.2 MPa.

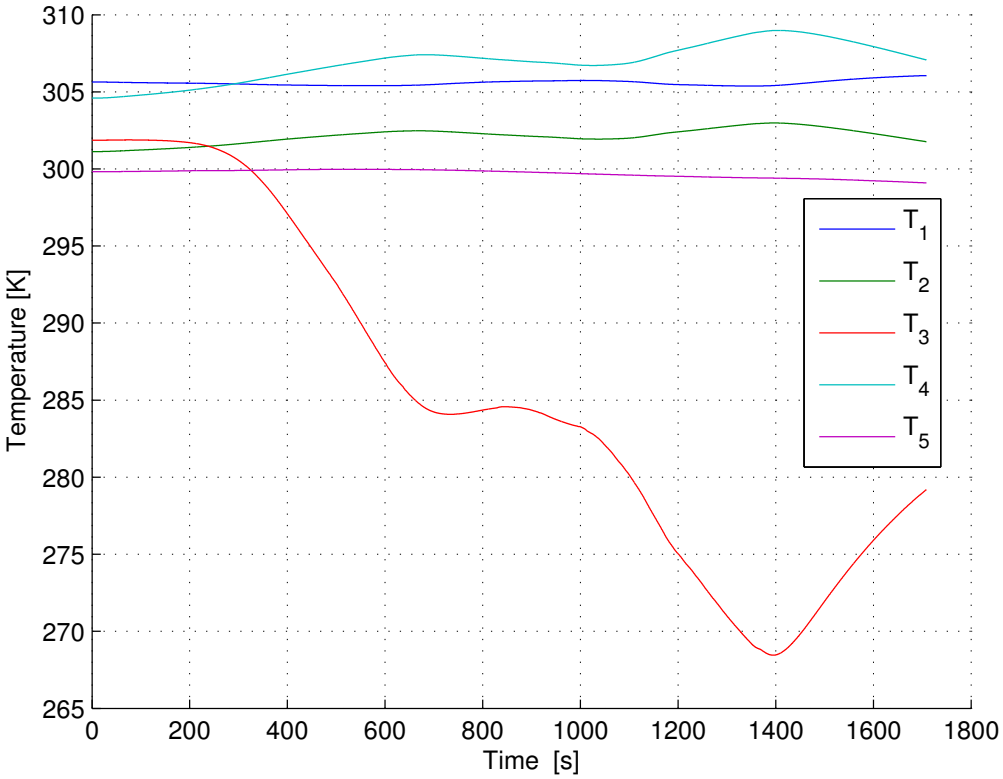

Figure A.27.: Pt100 Temperatures, Test 14.

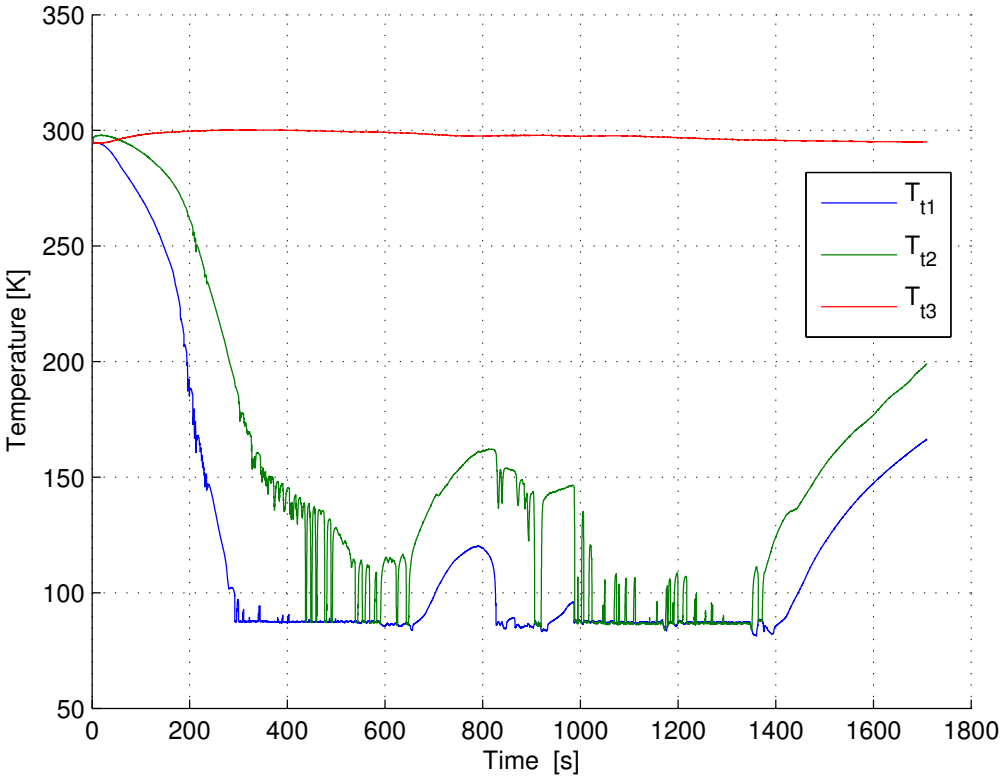

Figure A.28.: Thermocouple Temperatures, Test 14.

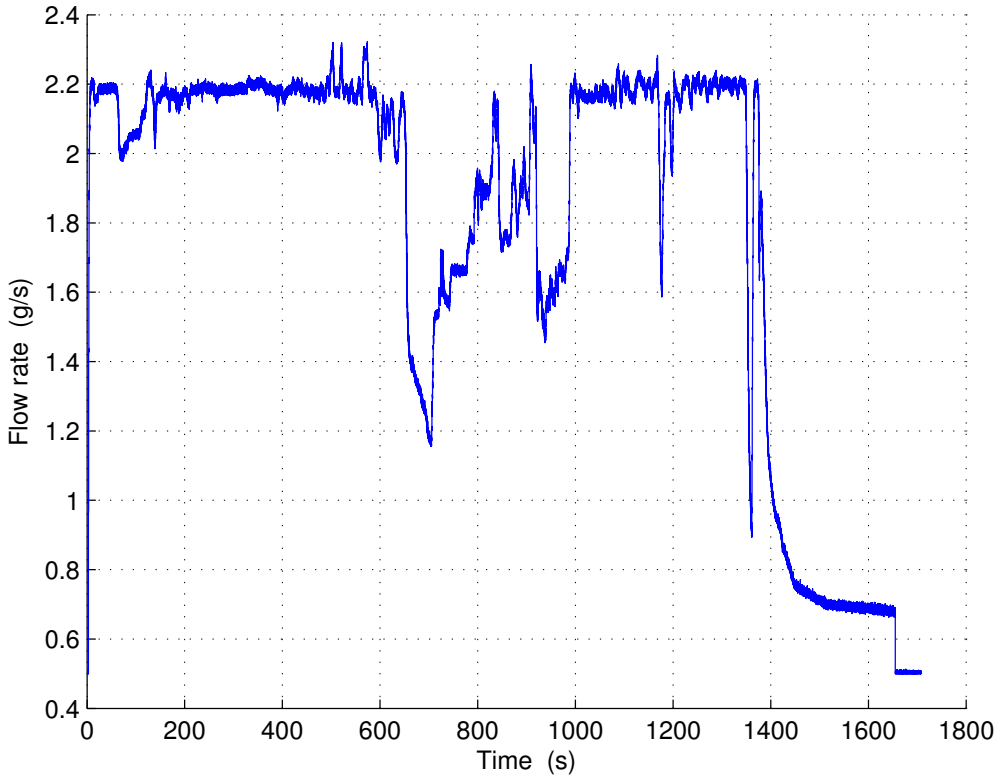

Figure A.29.: Mass Flow Rate, Test 14.

A.2.15. Test 15

Title: Heat conductivity measurement **Date:** 26.07.2013

Experimenters: Thomas Ballatré

Goal/Motivation: Determination of the heat transfer from regolith simulant to flowing, cryogenic nitrogen in a pipe system.

Execution: After cooling down of the nitrogen pipes (constant temperature at the nitrogen inlet of the vacuum chamber), the heat transfer is recorded for 5 minutes.

Parameters:
$p_{chamber}$ = 42 Pa
$p_{LN\ tank}$ = 250 kPa
T_{water} = 293.85 K
U = 0 V
I = 0 A

Results:
$p_{chamber}$ = 120 Pa
$p_{LN\ tank}$ = 230 kPa
T_{water} = 293.85 K
U = 0 V
I = 0 A
t = 300 s
m_{N_2} = 1.06 kg

Observations: Pressure rises to 72 Pa, declines to 60 Pa and rises against to 320 Pa. After that it declines again. As soon as T_4 stops rising and starts declining, the pressure declines, too.

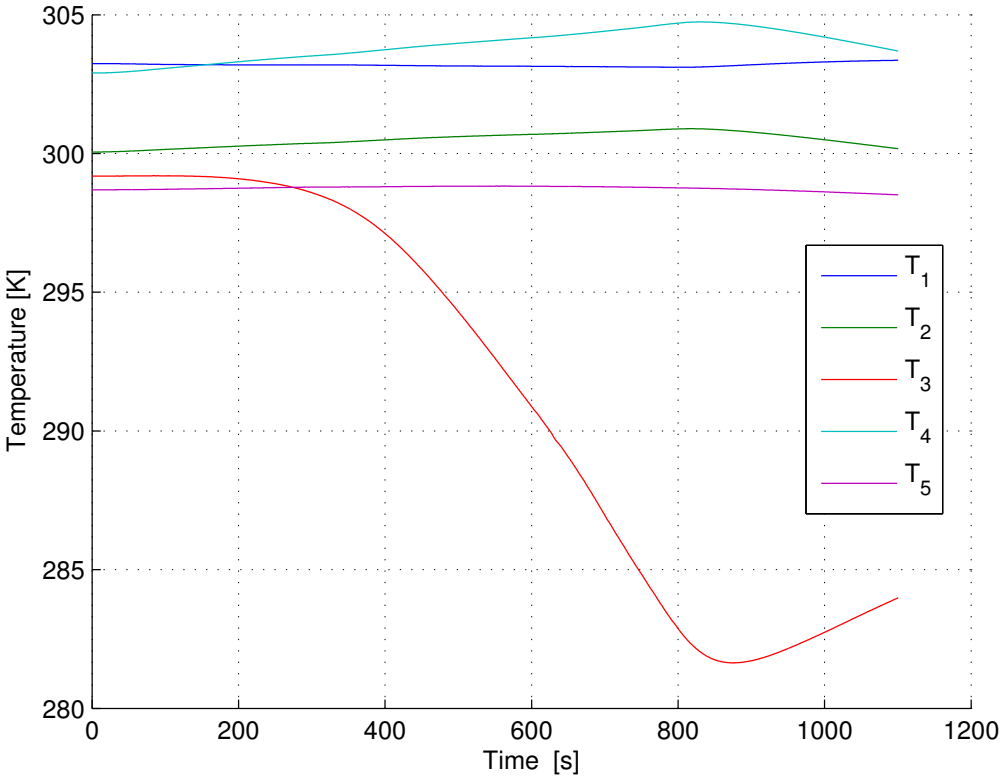

Figure A.30.: Pt100 Temperatures, Test 15.

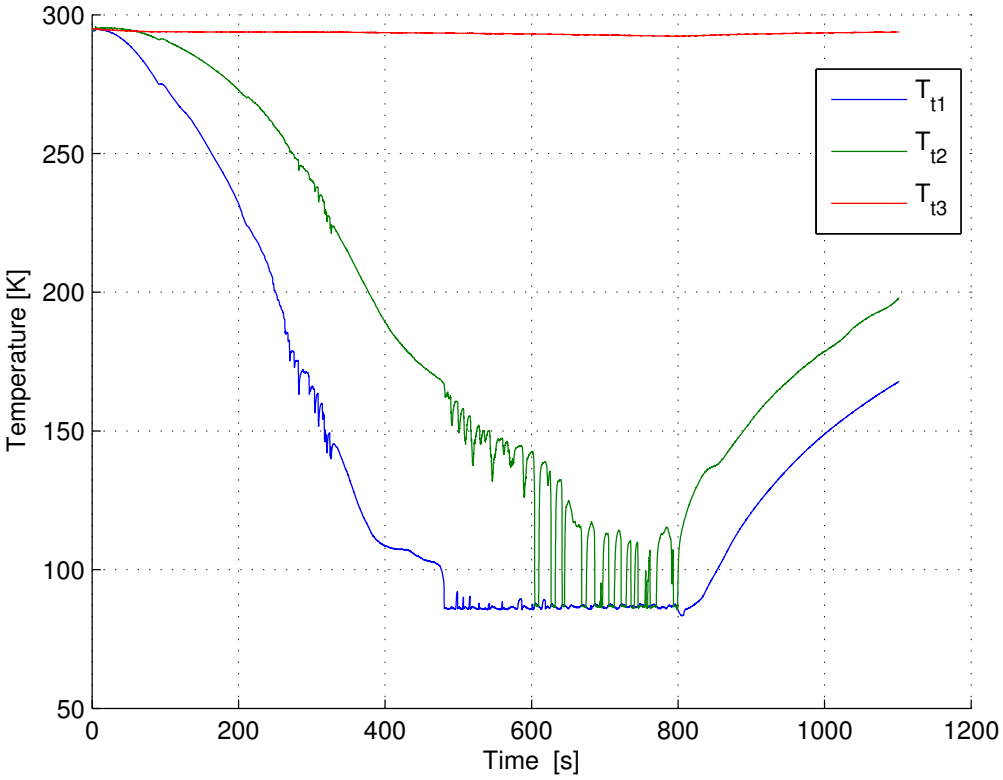

Figure A.31.: Thermocouple Temperatures, Test 15.

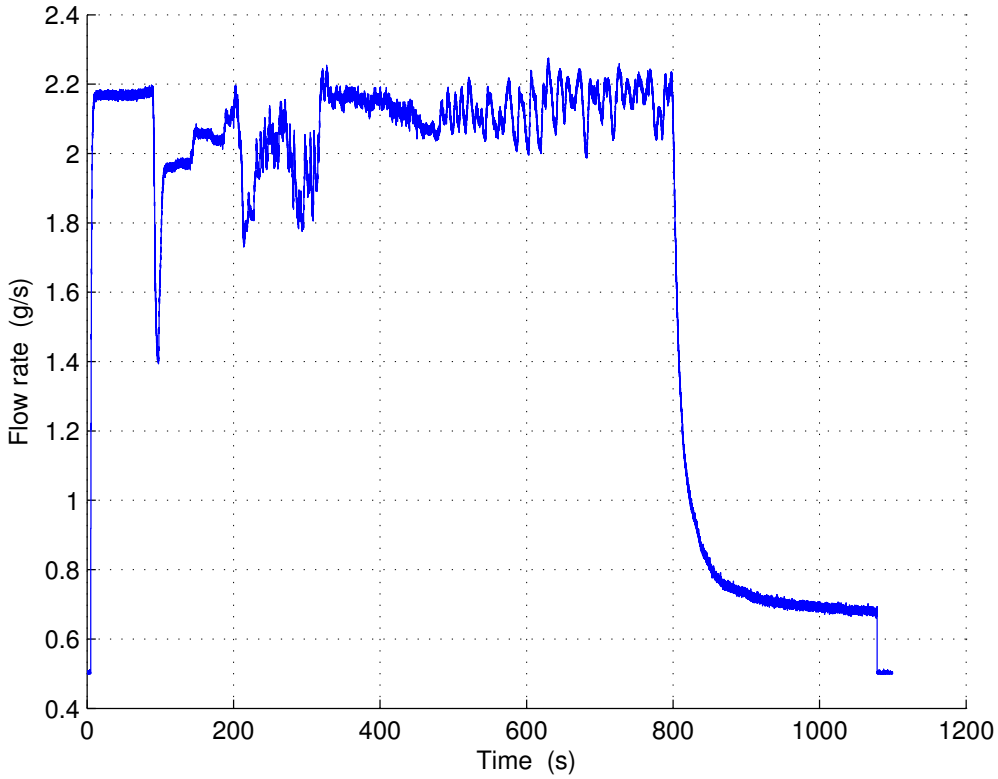

Figure A.32.: Mass Flow Rate, Test 15.

A.2.16. Test 16

Title: Heat conductivity measurement **Date:** 30.07.2013

Experimenters: Thomas Ballatré, Michael Elsen

Goal/Motivation: Determination of the heat transfer from regolith simulant to flowing, cryogenic nitrogen in a pipe system.

Execution: After cooling down of the nitrogen pipes (constant temperature at the nitrogen inlet of the vacuum chamber), the heat transfer is recorded for 5 minutes.

Parameters:
$p_{chamber}$ = 36 Pa
$p_{LN\ tank}$ = 238 kPa
T_{water} = 291.95 K
U = 0 V
I = 0 A

Results:
$p_{chamber}$ = 160 Pa
$p_{LN\ tank}$ = 220 kPa
T_{water} = 292.3 K
U = 0 V
I = 0 A
t = 300 s
m_{N_2} = 0.68 kg

Observations: -

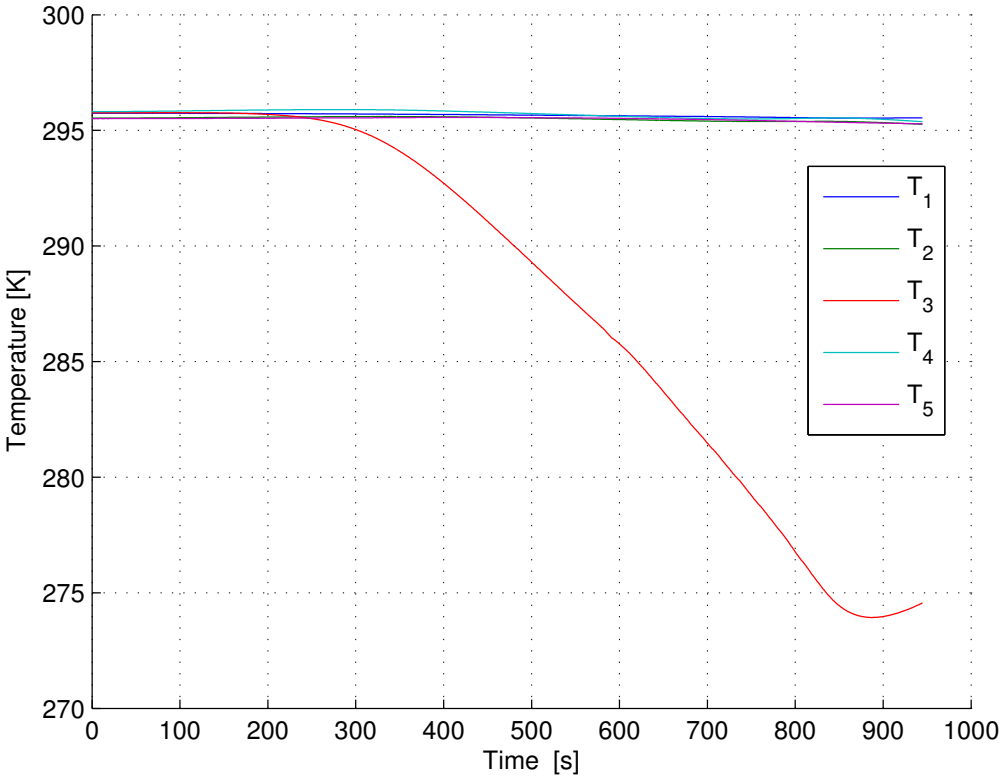

Figure A.33.: Pt100 Temperatures, Test 16.

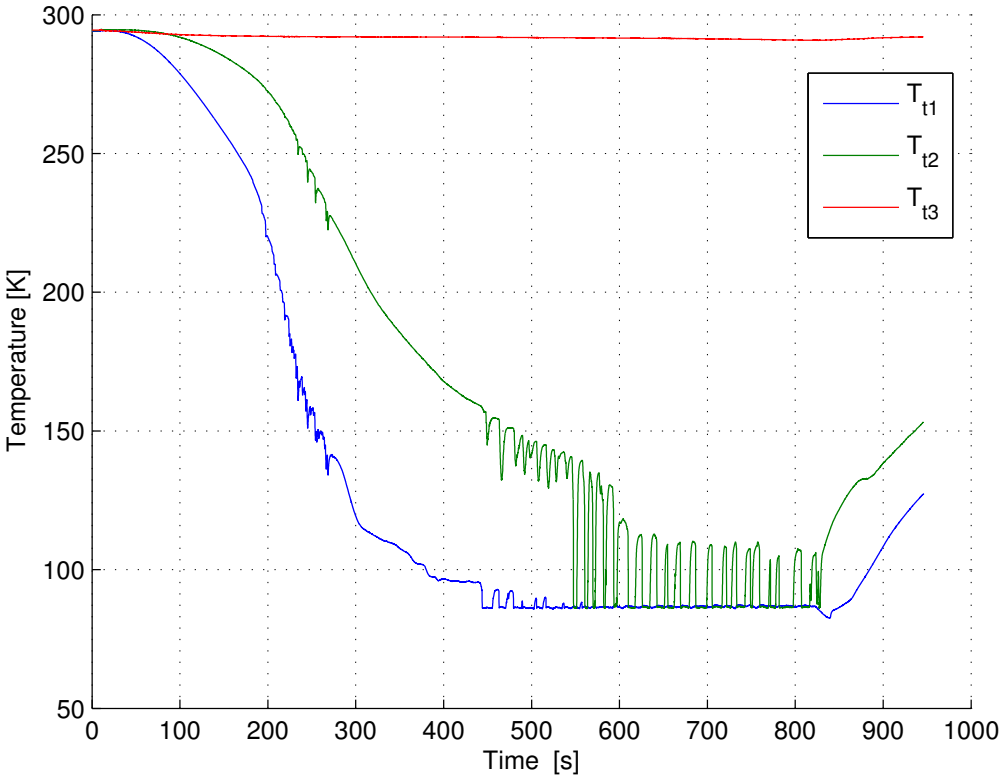

Figure A.34.: Thermocouple Temperatures, Test 16.

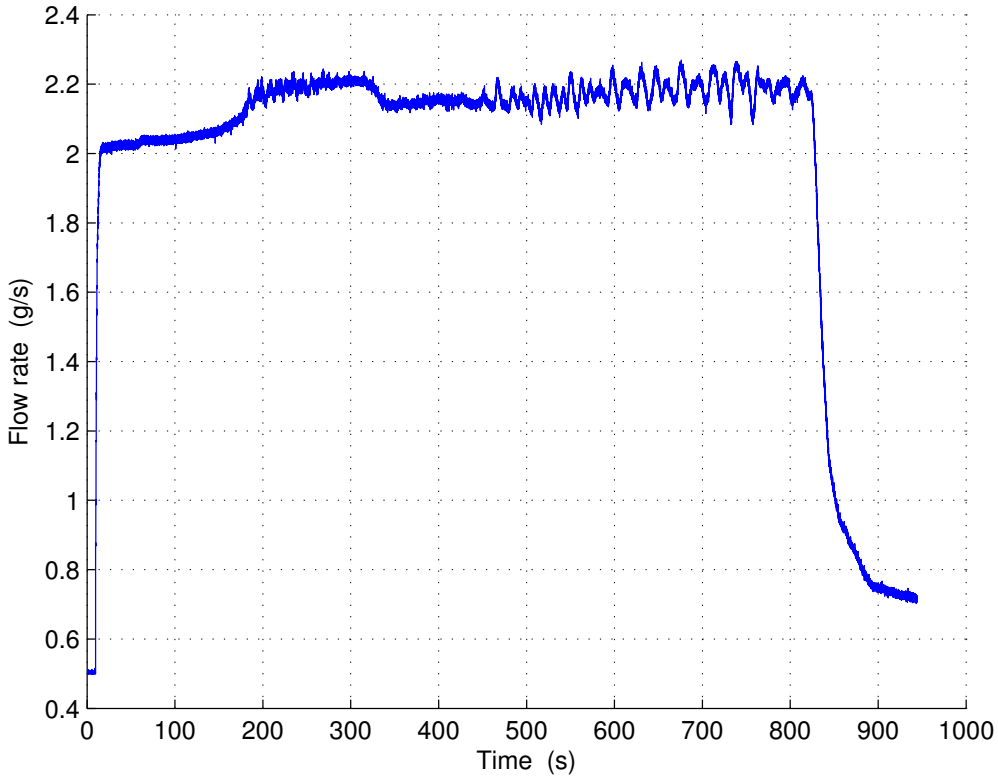

Figure A.35.: Mass Flow Rate, Test 16.

A.2.17. Test 17

Title: Heat conductivity measurement **Date:** 30.07.2013

Experimenters: Thomas Ballatré, Michael Elsen

Goal/Motivation: Determination of the heat transfer from regolith simulant to flowing, cryogenic nitrogen in a pipe system.

Execution: After cooling down of the nitrogen pipes (constant temperature at the nitrogen inlet of the vacuum chamber), the heat transfer is recorded for 5 minutes.

Parameters:
$p_{chamber}$ = 37 Pa
$p_{LN\ tank}$ = 229 kPa
T_{water} = 290.55 K
U = 0 V
I = 0 A

Results:
$p_{chamber}$ = 140 Pa
$p_{LN\ tank}$ = 215 kPa
T_{water} = 289.65 K
U = 0 V
I = 0 A
t = 337 s
m_{N_2} = 0.81 kg

Observations: -

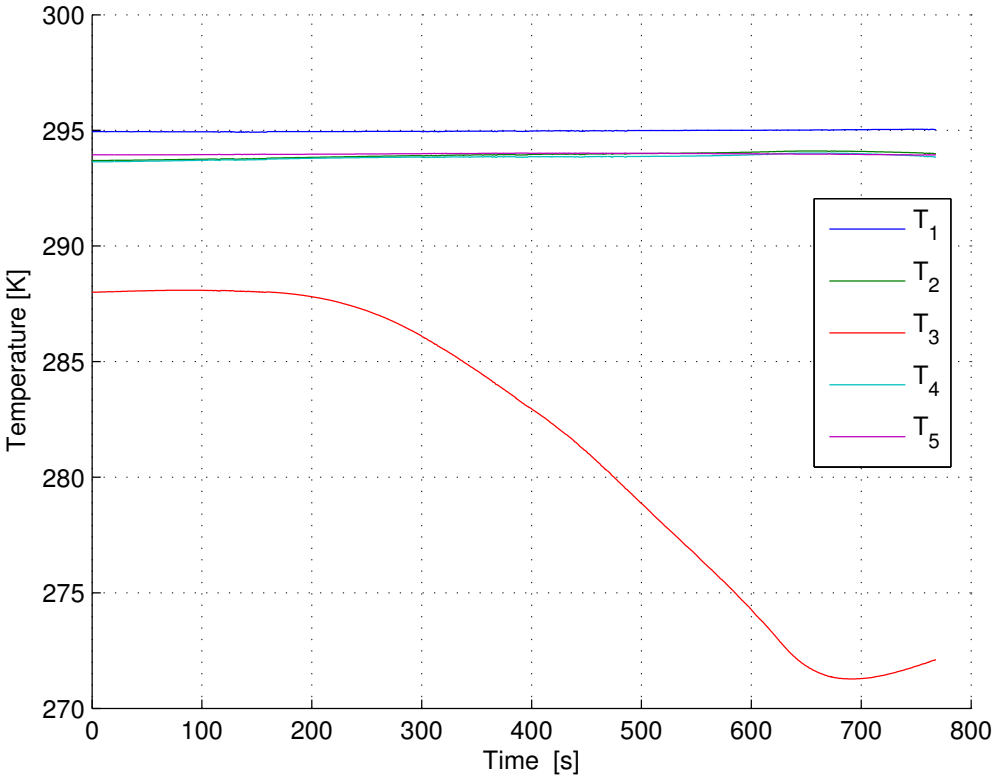

Figure A.36.: Pt100 Temperatures, Test 17.

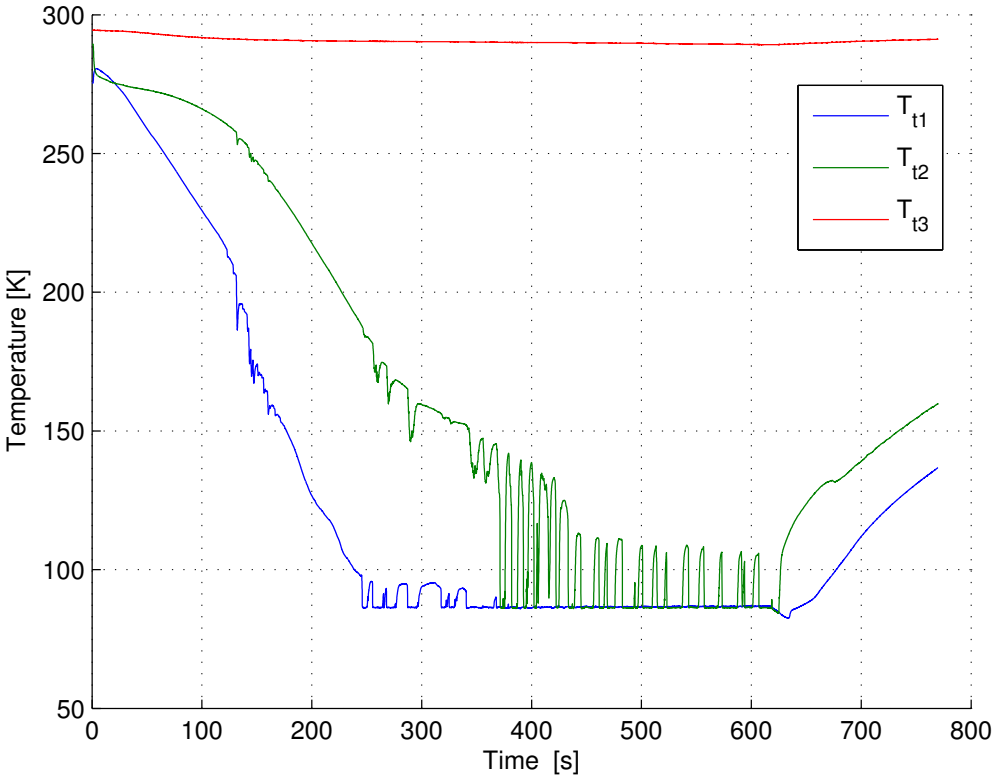

Figure A.37.: Thermocouple Temperatures, Test 17.

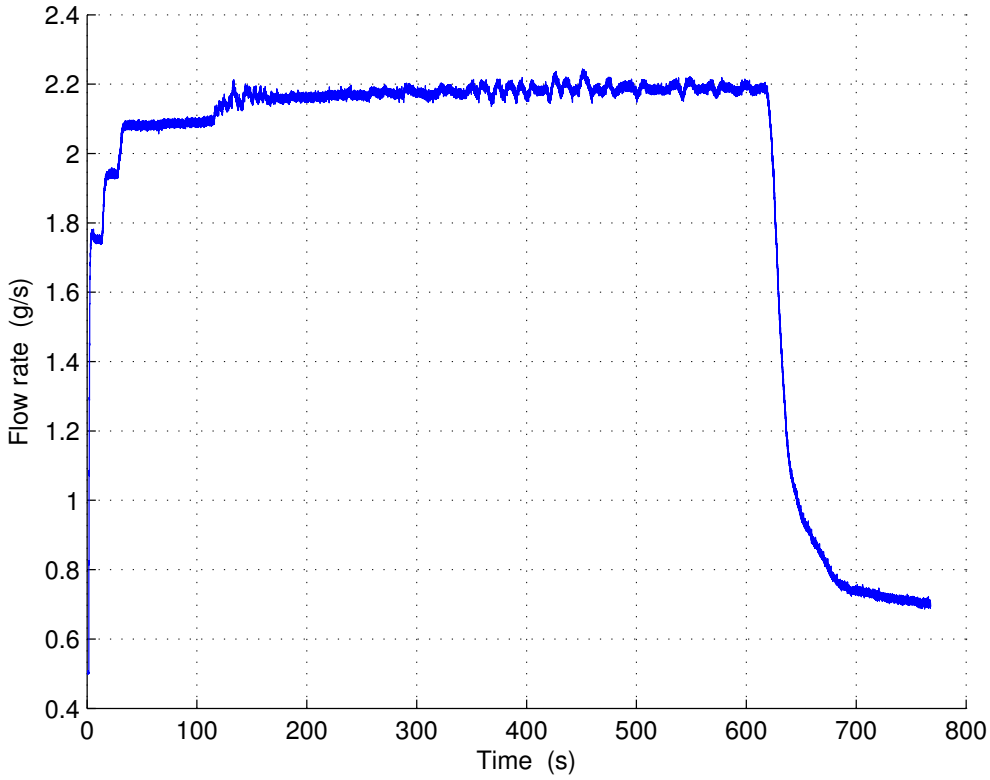

Figure A.38.: Mass Flow Rate, Test 17.

A.2.18. Test 18

Title: Heat conductivity measurement **Date:** 30.07.2013

Experimenters: Thomas Ballatré, Michael Elsen

Goal/Motivation: Determination of the heat transfer from regolith simulant to flowing, cryogenic nitrogen in a pipe system.

Execution: After cooling down of the nitrogen pipes (constant temperature at the nitrogen inlet of the vacuum chamber), the heat transfer is recorded for 5 minutes.

Parameters:
$p_{chamber}$ = 38 Pa
$p_{LN\ tank}$ = 221 kPa
T_{water} = 288.15 K
U = 0 V
I = 0 A

Results:
$p_{chamber}$ = 130 Pa
$p_{LN\ tank}$ = 209 kPa
T_{water} = 286.85 K
U = 0 V
I = 0 A
t = 300 s
m_{N_2} = 0.83 kg

Observations: -

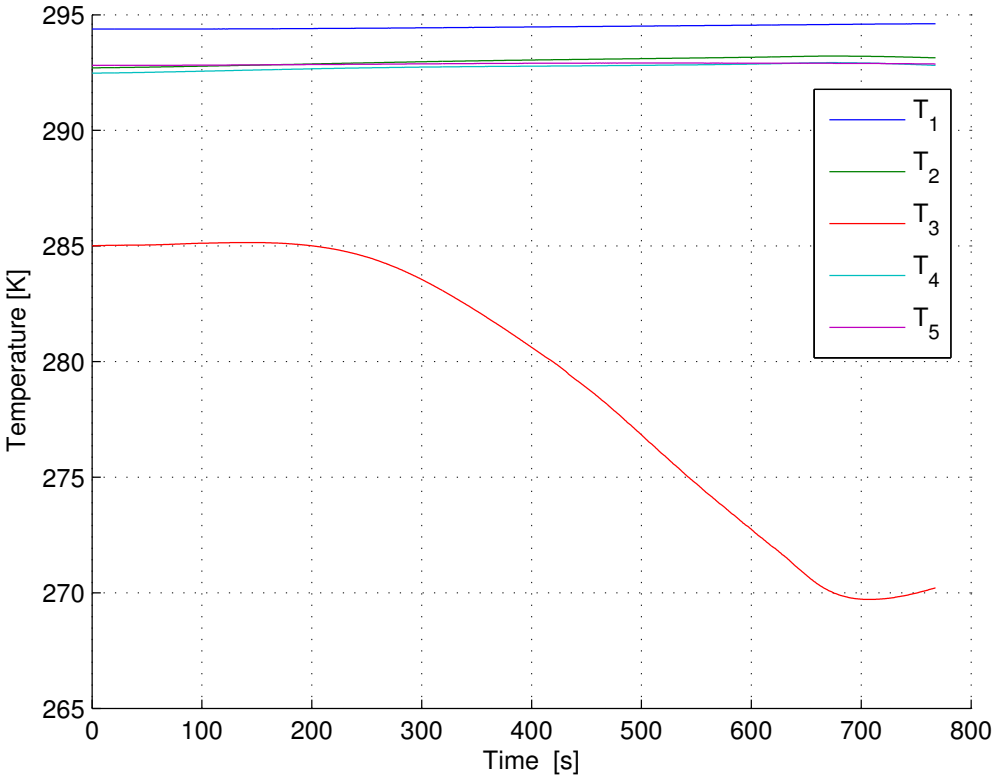

Figure A.39.: Pt100 Temperatures, Test 18.

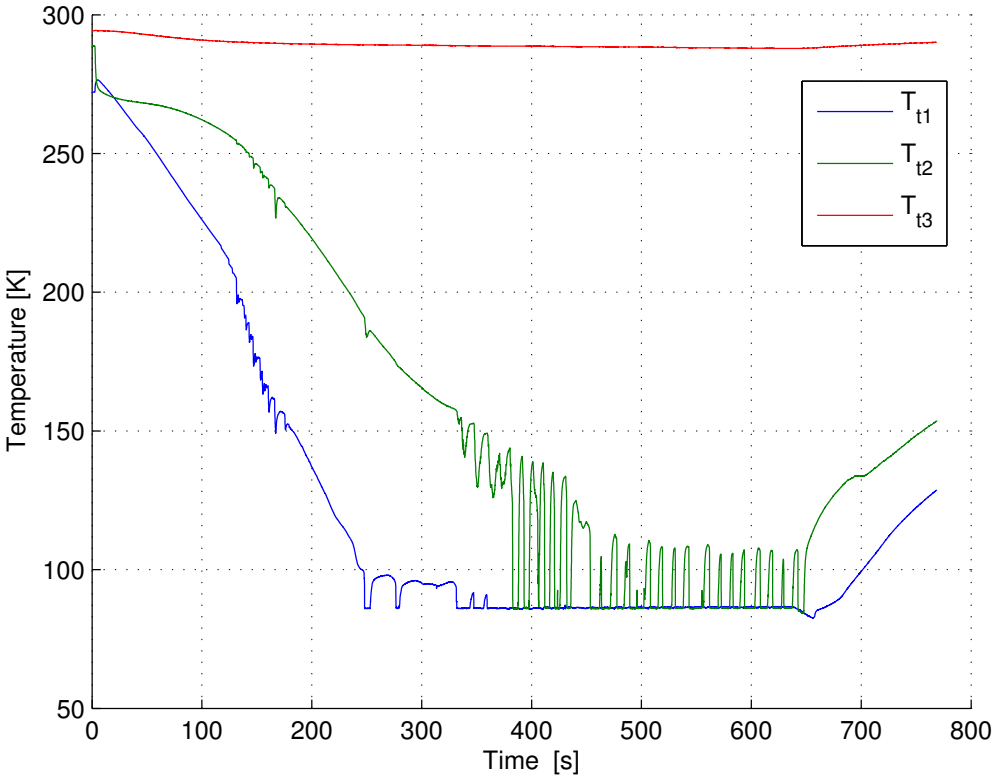

Figure A.40.: Thermocouple Temperatures, Test 18.

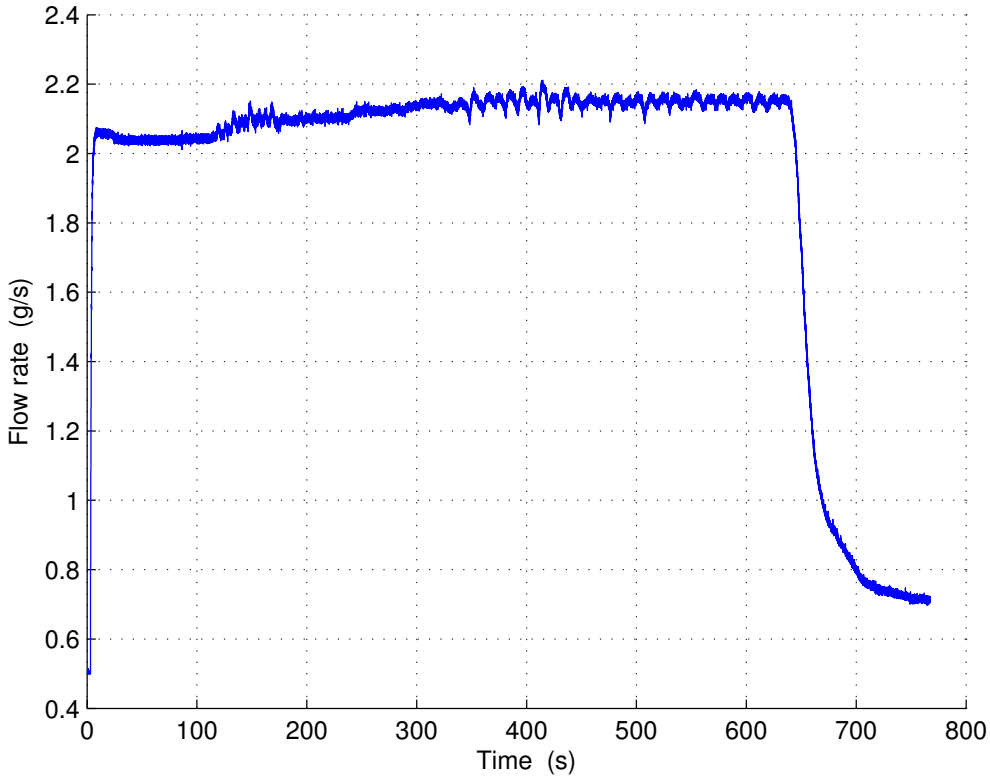

Figure A.41.: Mass Flow Rate, Test 18.

A.2.19. Test 19

Title: Heat conductivity measurement **Date:** 30.07.2013

Experimenters: Thomas Ballatré, Michael Elsen

Goal/Motivation: Determination of the heat transfer from regolith simulant to flowing, cryogenic nitrogen in a pipe system.

Execution: After cooling down of the nitrogen pipes (constant temperature at the nitrogen inlet of the vacuum chamber), the heat transfer is recorded for 10 minutes.

Parameters:
$p_{chamber}$ = 36 Pa
$p_{LN\ tank}$ = 231 kPa
T_{water} = 310.95 K
U = 0 V
I = 0 A

Results:
$p_{chamber}$ = 160 Pa
$p_{LN\ tank}$ = 213 kPa
T_{water} = 304.75 K
U = 0 V
I = 0 A
t = 600 s
m_{N_2} = 1.2 kg

Observations: -

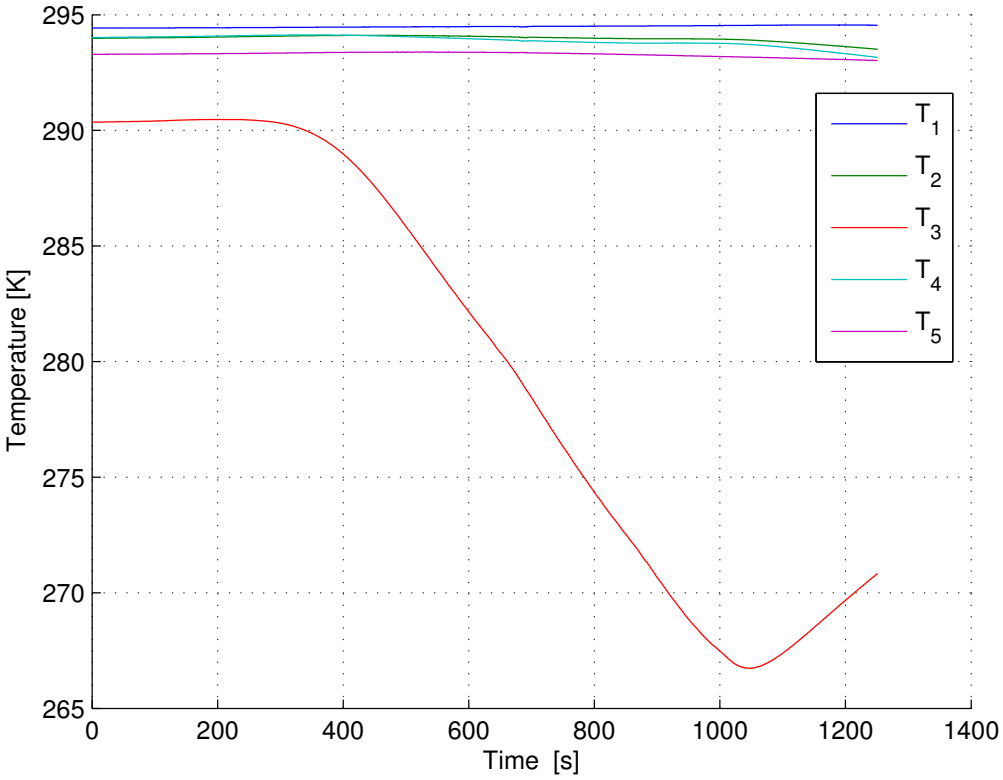

Figure A.42.: Pt100 Temperatures, Test 19.

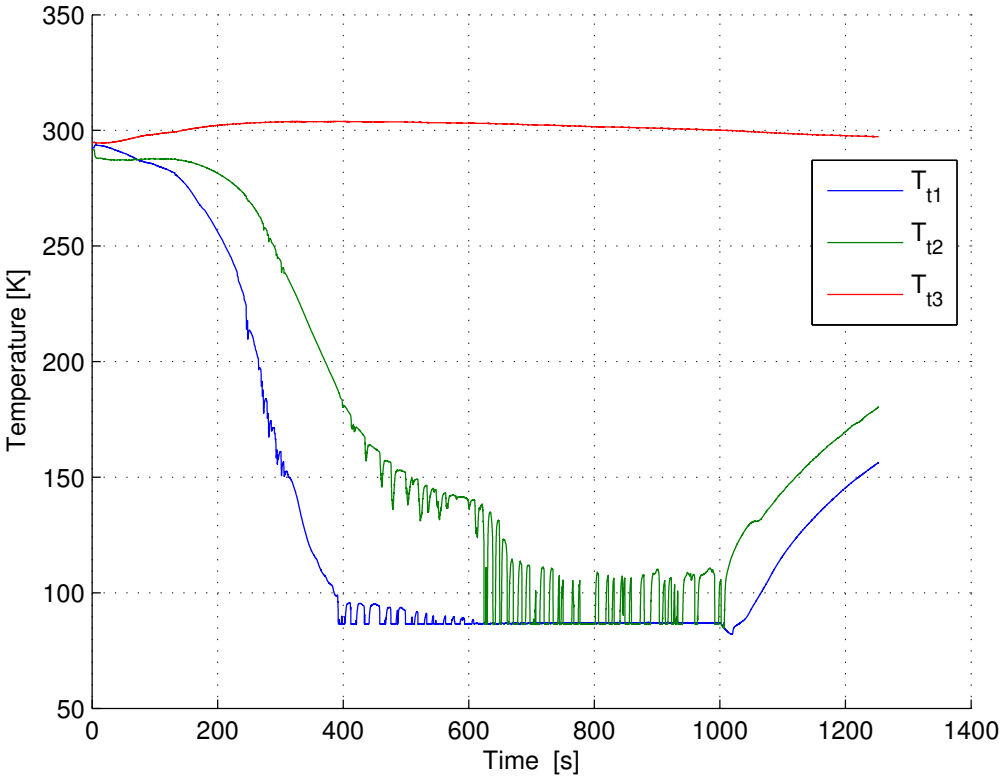

Figure A.43.: Thermocouple Temperatures, Test 19.

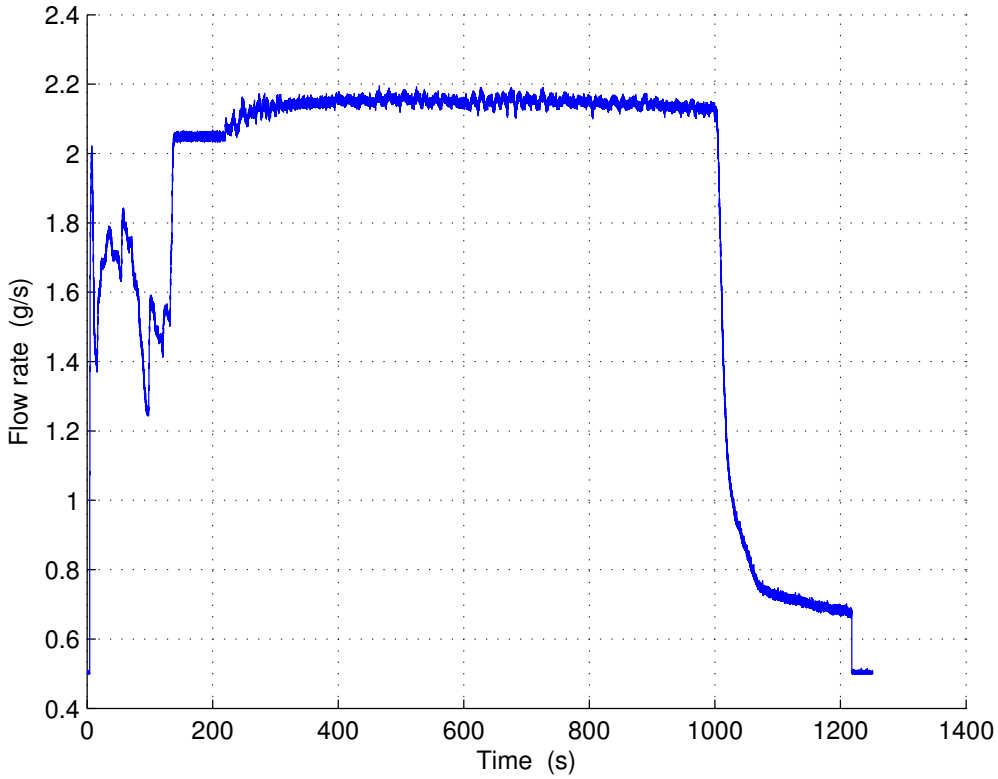

Figure A.44.: Mass Flow Rate, Test 19.

A.2.20. Test 20

Title: Heat conductivity measurement **Date:** 30.07.2013

Experimenters: Thomas Ballatré, Michael Elsen

Goal/Motivation: Determination of the heat transfer from regolith simulant to flowing, cryogenic nitrogen in a pipe system.

Execution: After cooling down of the nitrogen pipes (constant temperature at the nitrogen inlet of the vacuum chamber), the heat transfer is recorded for 10 minutes.

Parameters:
$p_{chamber}$ = 37 Pa
$p_{LN\ tank}$ = 222 kPa
T_{water} = 301.95 K
U = 0 V
I = 0 A

Results:
$p_{chamber}$ = 150 Pa
$p_{LN\ tank}$ = 208 kPa
T_{water} = 296.15 K
U = 0 V
I = 0 A
t = 630 s
m_{N_2} = 1.27 kg

Observations: -

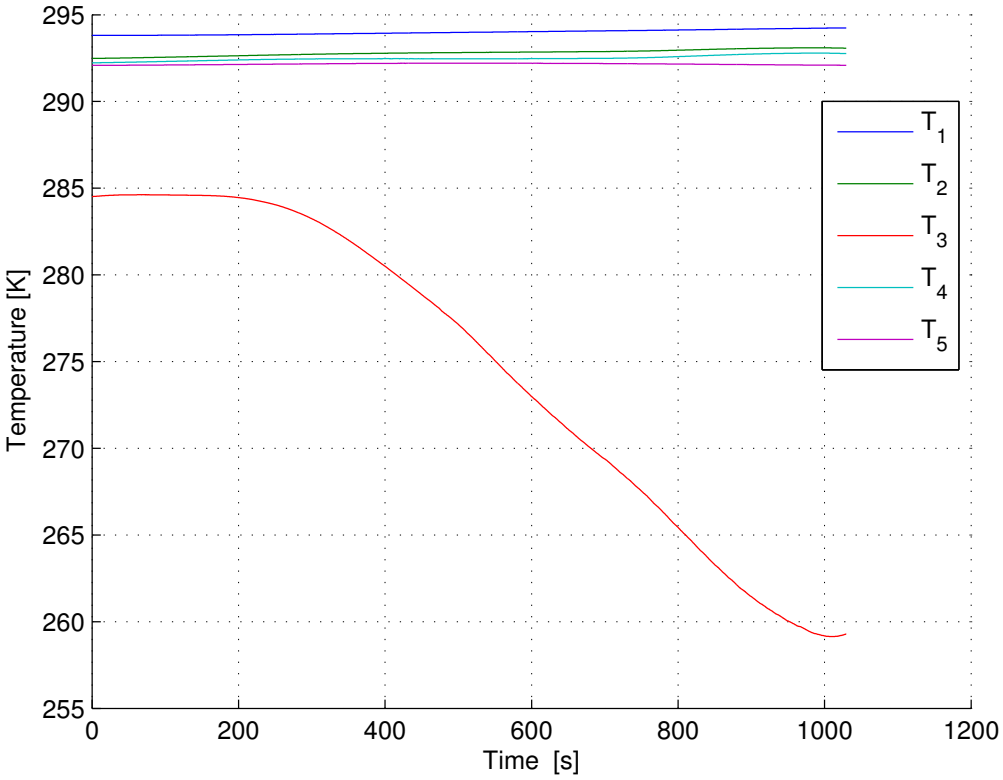

Figure A.45.: Pt100 Temperatures, Test 20.

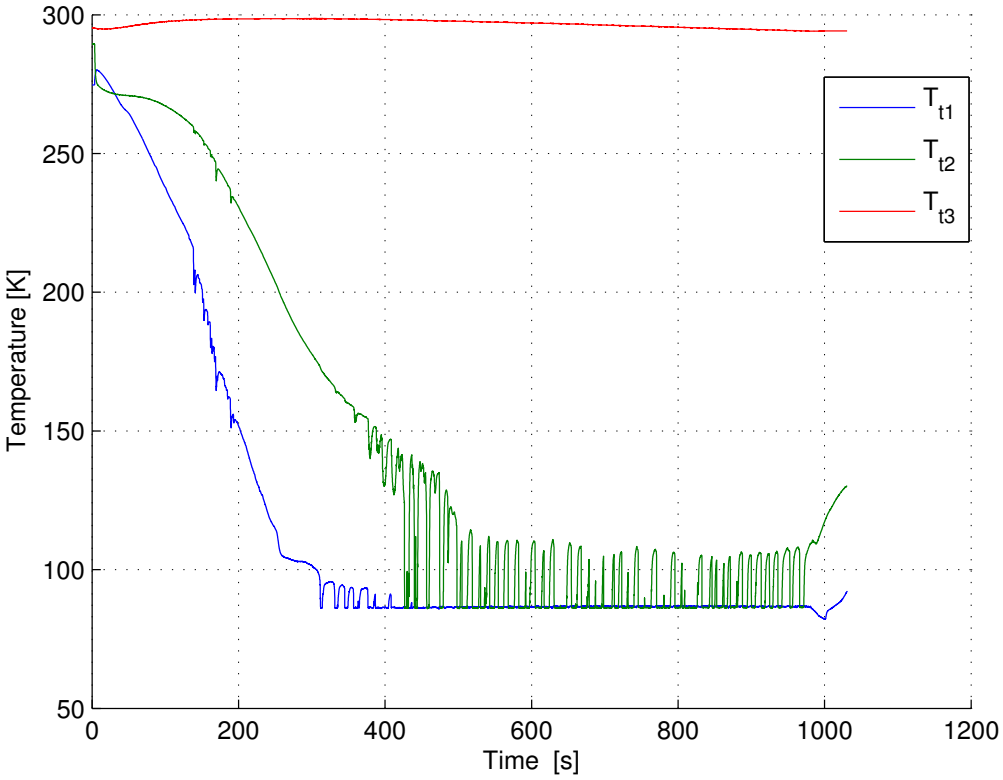

Figure A.46.: Thermocouple Temperatures, Test 20.

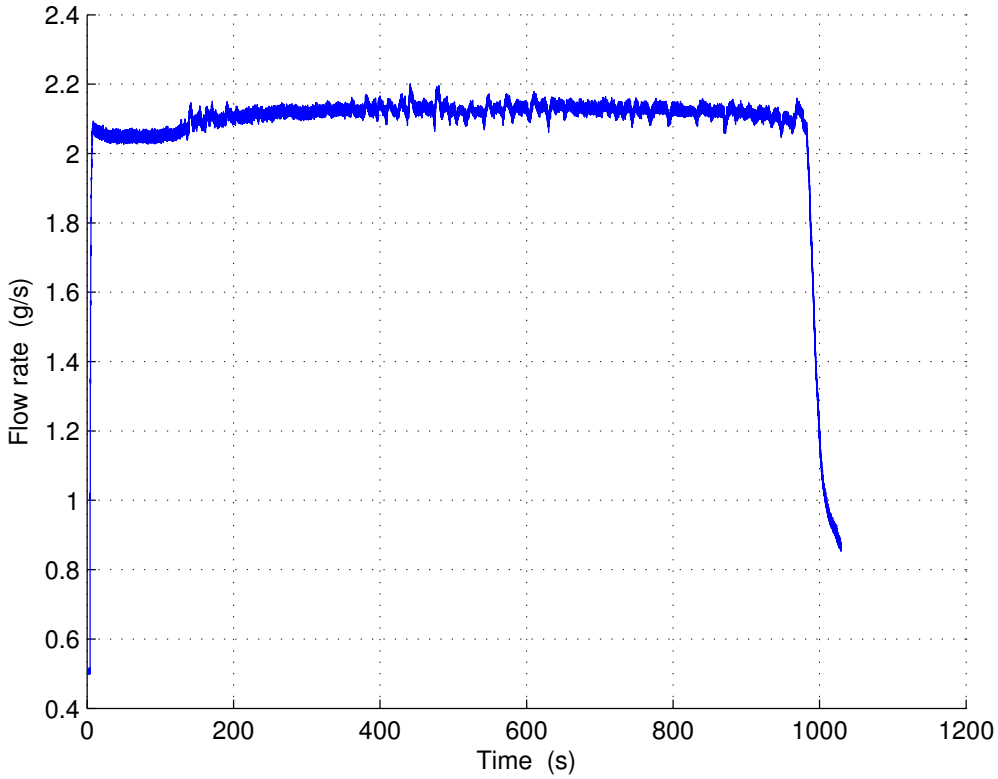

Figure A.47.: Mass Flow Rate, Test 20.

A.2.21. Test 21

Title: Heat conductivity measurement **Date:** 30.07.2013

Experimenters: Thomas Ballatré, Michael Elsen

Goal/Motivation: Determination of the heat transfer from regolith simulant to flowing, cryogenic nitrogen in a pipe system.

Execution: After cooling down of the nitrogen pipes (constant temperature at the nitrogen inlet of the vacuum chamber), the heat transfer is recorded for 10 minutes.

Parameters:
$p_{chamber}$ = 38 Pa
$p_{LN\ tank}$ = 215 kPa
T_{water} = 294.35 K
U = 0 V
I = 0 A

Results:
$p_{chamber}$ = 180 Pa
$p_{LN\ tank}$ = 204 kPa
T_{water} = 289.65 K
U = 0 V
I = 0 A
t = 620 s
m_{N_2} = 1.23 kg

Observations: -

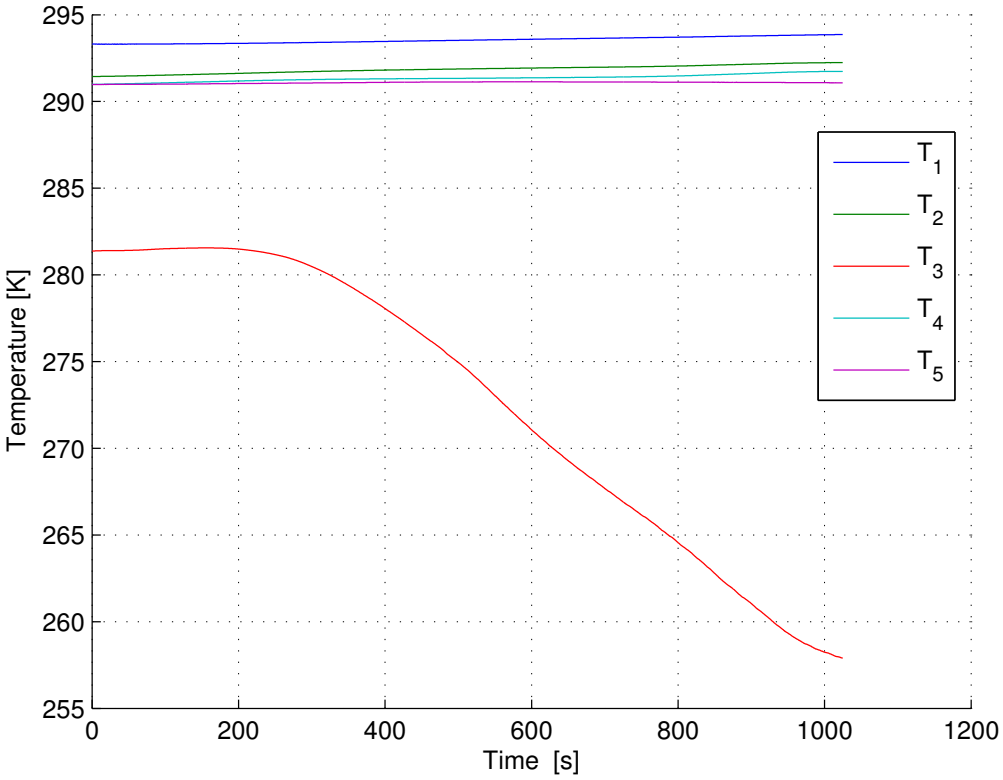

Figure A.48.: Pt100 Temperatures, Test 21.

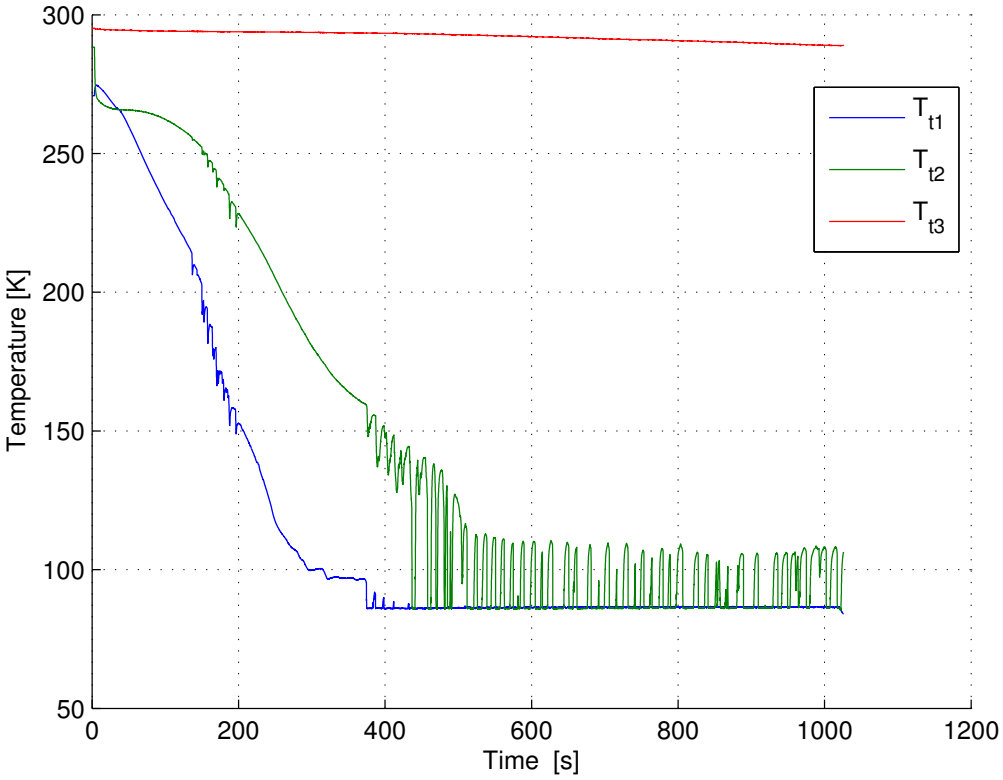

Figure A.49.: Thermocouple Temperatures, Test 21.

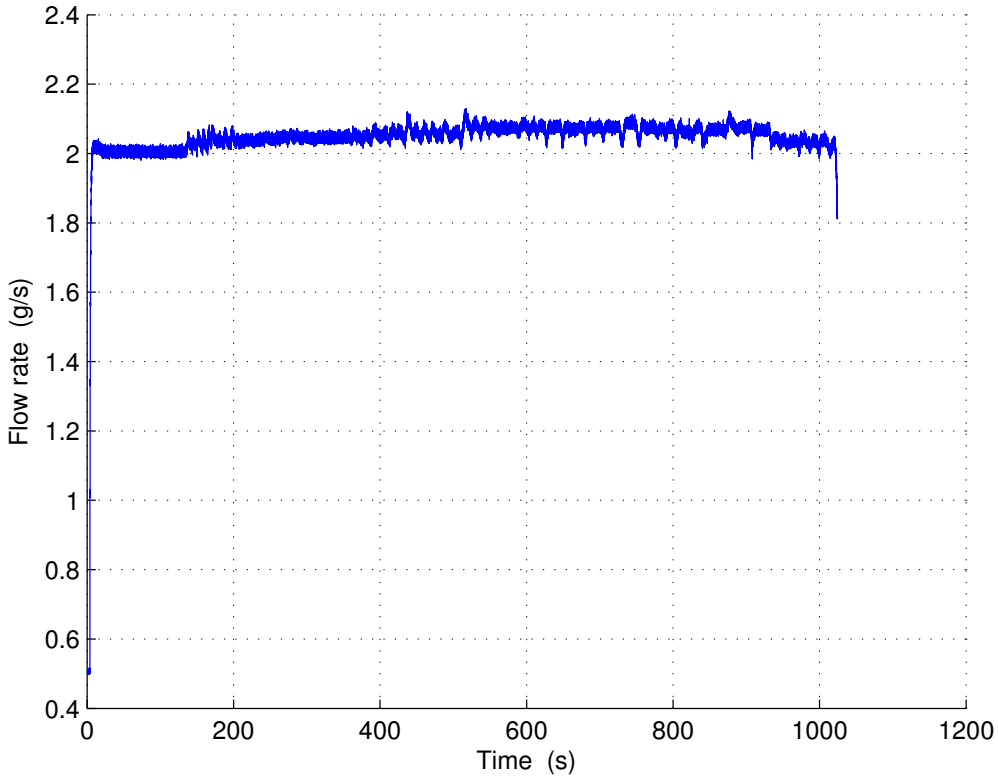

Figure A.50.: Mass Flow Rate, Test 21.

A.2.22. Test 22

Title: Determination of the electrical connection's resistance **Date:** 08.08.2013

Experimenters: Michael Elsen

Goal/Motivation: To determine the electrical resistance of the whole circuit (heating wire, current feedthrough and cable).

Execution: -

Parameters:
$p_{chamber}$ = -
$p_{LN\ tank}$ = -
$T_{hot\ plate}$ = 294.25 K
U = -
I = -

Results:
$p_{chamber}$ = -
$p_{LN\ tank}$ = -
$T_{hot\ plate}$ = 294.25 K
U = -
I = -
R = 0.42 Ω
t = -
m_{N_2} = -

Observations: -

A.3. Data Sheets

This section contains data sheets for:

- JSC-1A,
- Nitrogen,
- Heating Wire,
- Thermocouples.

MATERIAL SAFETY DATA SHEET

SECTION 1: Product and Company Identification

Orbital Technologies Corporation
1212 Fourier Drive
Madison, WI 53717

Phone Number: 608-827-5000
Availability: 8:00 am – 5:00 pm CDT
Website: www.lunarmarssimulant.com
Alternate Website: www.orbitec.com

Product Name: JSC-1AF, JSC-1A, JSC-1AC Lunar Mare Regolith Simulant
Issue Date: September 23, 2005

SECTION 2: Hazards Identification

Overview: The JSC-1A simulant family is a set of odorless powder/gray sand-like materials comprised of crushed basalt. JSC-1AF is primarily 50 micron particle size and lower, JSC-1A is 1 mm particle size and lower, and JSC-1AC is 5 mm particle size and lower. All JSC-1A types contain no asbestos or quartz. Since a fraction of all JSC-1A types contain particle sizes under 25 micron, JSC-1A is to be considered a nuisance dust and safe handling procedures per NIOSH 0500 nuisance dust classification should be followed to avoid symptoms of overexposure.

Caution: Excessive inhalation over long period may cause harmful irritation to eyes and respiratory tract. Use a NIOSH approved mask for nuisance dust for prolonged exposure.

HAZARD	RATING (0-4)
Health	1 (Slight hazard)
Reactivity	0 (No hazard)
Flammability	0 (No hazard)
Exposure	1 (Slight hazard)
Storage	0 (No hazard)

Potential Health Effects:
Inhalation: May cause irritation to the respiratory tract.
Skin Contact: No adverse effects expected.
Eye Contact: May cause irritation.
Chronic Exposure: No studies have been conducted on long-term effects.
Pre-existing conditions: Persons with impaired respiratory function may be aggravated by a nuisance dust.

See SECTION 11: **Toxicological Information.**

Potential Environmental Effects: None identified.

SECTION 3: Composition Information

The normal convention for data presentation uses oxide formulae from an assumed oxidation state for each element (with the exception of Fe) and oxygen is calculated by stoichiometry. For example, silicon is analyzed as an element but presented at SiO_2. It is important to understand that these are representations of the chemistry and do not represent actual phases or minerals in the simulant.

Major Element Composition	**CAS #**	**% by Wt.**
Silicon Dioxide (SiO_2)	14808-60-7	46-49
Titanium Dioxide ($TiO_{2)}$	13463-67-7	1-2
Aluminum Oxide (Al_2O_3)	1344-28-1	14.5 – 15.5
Ferric Oxide (Fe_2O_3)	1309-37-1	3-4
Iron Oxide (FeO)	1332-37-2	7 – 7.5
Magnesium Oxide (MgO)	1309-48-4	8.5 – 9.5
Calcium Oxide (CaO)	1305-78-8	10 – 11
Sodium Oxide (Na_2O)	1313-59-3	2.5 – 3
Potassium Oxide (K_2O)	12136-45-7	0.75 – 0.85
Manganese Oxide (MnO)	1344-43-0	0.15 – 0.20
Chromium III Oxide (Cr_2O_3)	1308-38-9	0.02 – 0.06
Diphosphorus Pentoxide (P_2O_5)	1314-56-3	0.6 – 0.7

SECTION 4: First Aid Measures

Inhalation: Move to fresh air. Get medical attention if symptoms occur.
Skin Contact: Wash exposed area with soap and water.
Eye Contact: Immediately flush eyes with water for 15 minutes. Get medical attention if irritation persists.

SECTION 5: Fire Fighting Measures

Fire: Not a fire hazard.
Explosion: No information found.
Fire extinguishing: Use any means suitable for extinguishing surrounding fire.

SECTION 6: Accidental Release Measures

Personal Precautions: Use personal protection recommended in Section 8.
Methods for Containment: No special instructions necessary.
Methods for Clean-Up: For spills, pick up and place in a suitable container for reclamation or disposal, using a method that avoids creating airborne dust.

SECTION 7: Handling and Storage

Handling: Use precaution when handling to minimize dust release of the material to the environment. Observe all warnings and precautions listed for this product.

Storage: Keep container closed when not in use and store in a cool, dry, ventilated area. Containers of the material may require caution when empty since they retain product residues (dust).

SECTION 8: Exposure Controls/Personal Protection

Airborne Exposure Limits: No ACGIH TLV exposure limits have been determined for JSC-1A, therefore maintain exposure limits for nuisance dust as defined by OSHA (15 mg/m^3) or ACGIH (10 mg/m^3).

Ventilation: When working with large quantities of JSC-1AF, a system of local and/or general exhaust is recommended to minimize employee exposure. A NIOSH/MSHA approved dust respirator is recommended for long exposure.

Skin Protection: Wear protective gloves as a precaution.

Eye Protection: Use safety goggles as a precaution.

SECTION 9: Physical and Chemical Properties

Appearance: JSC-1A and JSC-1AC: Gray material similar to sand or dirt
JSC-1AF: Gray material similar to powder

Odor: None detected

Specific Gravity: 2.9 g/cm^3

pH: No information

Melting Point: 1100º - 1125º C

Angle of Internal Friction: 45º

Cohesion: 1.0 kPa

SECTION 10: Stability and Reactivity

Stability: Stable under ordinary conditions of use and storage.

Conditions to Avoid: None

Incompatible Materials: No information found

Hazardous Decomposition Products: No information found

SECTION 11: Toxicological Information

General Comments: Inhalation of dust may irritate nose, throat and lungs. Eye contact with solids may produce irritation. Use NIOSH nuisance dust masks or respirators and eye protection to avoid long term exposure to dust component if applicable during use.

The information contained in this document applies to this specific material as supplied. The information contained herein is believed to be accurate but is provided without warranty of any kind, express or implied. It may not be valid for this material if it is used in combination with any other materials. It is the user's responsibility to satisfy oneself as to the suitability and completeness of this information for his/her own particular use.

Betriebsanweisung

gem. § 14 GEFAHRSTOFFVERORDNUNG

Betrieb:	DLR, Standort Bremen	**Erstellt / Überprüft**	U. Rosendahl / N. Fehlauer
Arbeitsplatz:	Kryolabor, Haus 2, Raum 0.25 - 0.31	**Tätigkeit:**	Um- und Abfüllen von flüssigem Stickstoff

Gefahrstoffbezeichnung

	Stickstoff, tiefkalt, flüssig				
Andere Bezeichnung:	Flüssigstickstoff				
Enthält außerdem:	Bei längerem Stehen an der Luft kondensiert Sauerstoff ein			**AGW:** nicht festgelegt	
Form:	flüssig	**Farbe:**	farblos	**Geruch:**	geruchlos

Gefahren für Mensch und Umwelt

Achtung

- **Kälte, Erfrierungen und Kaltverbrennungen (H281)**
  Flüssiger Stickstoff ist tiefkalt (-196 °C), bei Kontakt kommt es zu Kaltverbrennungen bzw. Erfrierungen, Gefahr schwerer Augenschäden.
- **Sauerstoffmangel, Erstickungsgefahr**
  Verdampfen führt zur Anreicherung in der Luft und somit unmerklich zur Erstickungsgefahr (Schläfrigkeit, Unwohlsein, Blutdruckanstieg, Atemnot)
- **Berstgefahr durch Druckanstieg**
  Der Einschluss von flüssigem Stickstoff in nicht dafür vorgesehene Gefäße ohne Druckausgleich kann zum Bersten der Behältnisse führen. Bei Kunststoffgefäßen tritt Kaltversprödung auf.
- **Erhöhte Brand- und Explosionsgefahr**
  In offene Gefäße kann Luftsauerstoff einkondesieren; flüssiger Sauerstoff bildet mit organischen Stoffen explosionsfähige Gemische. Es besteht die Gefahr einer spontanen Entzündung.

Schutzmaßnahmen und Verhaltensregeln

- Flüssigstickstoff nicht über längere Zeit in offenen Gefäßen lagern. Gefäße immer sofort abdecken. Lagerbehälter nur kurz öffnen, regelmäßig den Flüssigstickstoff vollständig austauschen!
- Beim Ab- und Umfüllen Verspritzen und Nachlauf vermeiden. Flüssigstickstoff nur langsam und portionsweise in wärmere Gefäße/Lösungen geben.
- Behälter und Apparaturen sind vorsichtig zu behandeln, vor der Füllung gut zu trocknen und gegen Umfallen zu sichern.
- Flüssigstickstoff aus Dewaren und Testbehältern nicht zurück in Vorratsgefäße geben.
- Kryobehälter (Deware) sind so zu transportieren, dass sie nicht umfallen oder umkippen können.
- Auf Trockenheit achten, nur trockene Hilfsmittel verwenden.
- Auf Materialeignung achten. Gerätschaften und Hilfsmittel, die für den direkten Umgang mit flüssigem Stisckstoff bestimmt sind, müssen aus kältebeständigem Material sein.
- Drucklose Behälter, die Flüssigstickstoff enthalten, dürfen nur mit einem lose aufliegendem Deckel oder Stopfen verschlossen werden, so dass ein Druckausgleich möglich ist. Diese Behälter dürfen nur drucklos befüllt und transportiert werden. Deware, die für inneren Überdruck geeignet sind, sind entsprechend gekennzeichnet.
- Bei Transport von Flüssigstickstoff in Aufzügen dürfen keine Personen mitfahren (Siehe hierzu auch die Betriebsanweisung „Transport von Kryobehältern im Aufzug“)
- Behälter, Leitungen, verschraubte Flansche regelmäßig auf Materialschrumpfungen prüfen.
- Nicht Essen, Trinken, Rauchen oder Schnupfen. Einatmen von Dämpfen vermeiden! Berührung mit Augen, Haut und Kleidung vermeiden!
- **Augenschutz:** Korbbrille oder Gestellbrille mit Seitenschutz! Bei Gefährdung des Gesichts durch Spritzgefahr, Visier tragen.
- **Handschutz:** Kältebeständige, flüssigkeitsdichte, gut isolierende Handschuhe (Kryohandschuhe) verwenden. Bei Bedarf; gerbstoffhaltige Hautschutzmittel verwenden.
- **Körperschutz:** Saubere, trockene, nicht eng anliegende körperbedeckende Kleidung aus Naturfasern, ohne umgeschlagene Hosenbeine oder Ärmel. Geschlossene Schuhe, die schnell ausgezogen werden können. Beim Ab- und Umfüllen zusätzlich: Kälteschutzschürze.

Betriebsanweisung

gem. § 14 GEFAHRSTOFFVERORDNUNG

Fortsetzung

Schutzmaßnahmen und Verhaltensregeln (Fortsetzung)

- **Atemschutz:** Bei zu geringer Sauerstoffkonzentration (Überwachungsgerät!) oder bei unklaren Verhältnissen: Umgebungsluftunabhängiges Atemschutzgerät verwenden (ggf. Feuerwehr anfordern).

Verhalten im Gefahrenfall — Notruf: 0-112

Unbeabsichtigte Freisetzung

- Gefahrenbereich räumen und absperren. Vorgesetzten informieren.
- Bei Auslaufen größerer Mengen den Raum verlassen! Das gilt insbesondere in schlecht belüfteten Bereichen (z.B. Kellerräumen oder Fluren). Betreten des Bereichs nur mit umgebungsluft-unabhängigem Atemschutz (ggf. Feuerwehr anfordern). Benachbarte Bereiche warnen.Dämpfe nicht einatmen.

Brand

- Stickstoff ist nicht brennbar. Alle bekannten Löschmittel können benutzt werden. Brandbekämpfung auf Umgebung abstimmen.
- Berst- und Explosionsgefahr bei Erwärmung (z. B. von Transportbehältern und Kryostaten).
- Alarm-, Flucht- und Rettungspläne beachten. Feuerwehr alarmieren.

Erste Hilfe — Notruf: 0-112

- **Bei jeder Erste-Hilfe-Maßnahme:** Betroffenen unter Selbstschutz auf dem sichersten Weg aus der Gefahrenzone bergen, an die frische Luft bringen, hinlegen, ruhig und warm halten. Durchgaste Kleidung vorsichtig entfernen. Wunden keimfrei bedecken. Bei Gefahr der Bewusstlosigkeit Lagerung und Transport in stabiler Seitenlage. Bei Atemstillstand Atemspende/künstliche Beatmung. Bei Atem- und Kreislaufstillstand Herz-Lungen-Wiederbelebung. Notarzt zum Unfallort rufen.
- **Nach Augenkontakt:** Augen bei Erfrierung bei vorsichtig geöffnetem Lidspalt (Lidkrampf!) von innen nach außen mit handwarmen Wasser oder physiologischer Kochsalzlösung spülen. Lockerer keimfreier Verband. Sofortige augenärztliche Weiterbehandlung.
- **Nach Hautkontakt:** Benetzte Kleidungsstücke, Schuhe und Strümpfe sofort ausziehen. Bei Erfrierungen betroffene Stellen mit viel lauwarmem (keinesfalls heißem) Wasser übergießen. Keine Anwendung direkter Wärme. Die erfrorenen Stellen nicht reiben, da dies das Gewebe beschädigen kann. Wunde steril abdecken. Bei Gefahr von Bewusstlosigkeit Lagerung und Transport in stabiler Seitenlage. Arzt zum Unfallort rufen.
- **Nach Einatmen:** Verletzten aus dem Gefahrenbereich bringen. Frischluftzufuhr durch Einatmen von frischer Luft. Bei Atemstillstand oder verlangsamter Atmung künstlich beatmen. Möglicherweise ist Sauerstoffzufuhr erforderlich. Sofortige ärztliche Weiterbehandlung.
- **Nach Verschlucken:** Verschlucken wird nicht als möglicher Weg der Exposition angesehen.
- ERSTHELFER: Siehe gesonderten Aushang, bzw. Notfallplan
- UNFALLARZT: siehe gesonderten Aushang
- NORTUF: 0 -112 FEUERWEHR: 0-112

Sachgerechte Entsorgung

- Nicht in die Kanalisation, Keller, Arbeitsgruben und ähnliche Plätze, an denen die Ansammlung des Gases gefährlich werden könnte, ausströmen lassen.
- Reste flüssigen Stickstoffs im Freien abdampfen lassen.

Ansprechpartner / Betreiber: U. Rosendahl Unterschrift:

Daturm: 29.02.2012

Nächste Überprüfung: 29.02.2013

Resistance wire on mini bobbin
RD 100/4,0

Electrical data

Type	RD 100/4,0

Mechanical data

Type	RD 100/4,0
Operating data	
Resistance	0.039 Ω/m
highest wire temperature	to 600 °C
Mean linear coefficient of thermal expansion between 20 - 100 °C	13.5x10-6
Mean temperature coefficient of resistance at 20 °C	0.00004-0.00008
Melting point	1220-1270 °C
Specific electrical resistance	0.49 (Ω x mm²)/m
Current intensity for wire temperature (100°C)	23.900 A
Current intensity for wire temperature (200°C)	40.000 A
Current intensity for wire temperature (300°C)	54.000 A
Measures and weights	
Wire diameter	4.00 mm
Weight	0.10 kg

Subjects to change.

Electronic Sensor ...Temperaturen messen

Standard- Mantelthermoelmente- Ausgleichs- und Thermoleitung- Thermostecker- Lote- Verschraubungen- Pt 100-Widerstandsfühler

Betriebswirt: Dieter Betz
Edisonstr. 3 * 74076 Heilbronn
Tel. 07131 / 79796-0
Fax 07131 / 79796-29
email: info@electronic-sensor.de
Internet: www.electronic-sensor.de

Chargenzeugnis AB-Nr. 330419

Antragsteller : DLR - Lampoldshausen

Auftragsnummer: x/329/67175971 **vom:** 05.04.2013

Gegenstand : Mantelleitung, NiCr - Ni, Typ K

Chargen-Nr. : 109331/1 **Länge :** 176 m **Durchmesser :** 1,0 mm

---

Kalibriert nach DIN EN 60584 – 1

Die Messung der Thermospannung hat die folgenden Werte :

Temperatur Soll °C	Temperatur Ist °C	Thermospannung Ist mV	Abweichung mV	Abweichung °C
- 196,00	-195,25	- 5,817	0,012	0,75

Die ermittelten Abweichungen entsprechen der DIN EN 60584-2 , Klasse : 1 Temperatur der Vergleichstelle: 0 °C
Der Wert – 195,25 Grad C (76,90 K) entspricht gemäß DIN EN 60 584 , Tol. Klasse 3 .
(+- 1,5 % MW)

Datum/ Unterschrift : 30.04.2013 .....

ES Electronic Sensor GmbH
Postanschrift:
Postfach 1625 * 74006 Heilbronn
Lieferanschrift:
Edisonstr. 3 * 74076 Heilbronn
Telefon 0 71 31 / 79 79 60 - 0
Telefax 0 71 31 / 79 79 6 - 29